Check for updates

IKAROS and MENIN coordinate therapeutically actionable leukemogenic gene expression in *MLL*-r acute myeloid leukemia

Brandon J. Aubrey[1,2,14], Jevon A. Cutler[1,14], Wallace Bourgeois[1,3,14], Katherine A. Donovan[4,5], Shengqing Gu[6,7], Charlie Hatton [1], Sarah Perlee[1], Florian Perner[1,8], Homa Rahnamoun [1], Alexandra C. P. Theall[1], Jill A. Henrich[1], Qian Zhu [1,3], Radosław P. Nowak [4,5], Young Joon Kim[1], Salma Parvin [9], Anjali Cremer[1,10,11], Sarah Naomi Olsen [1], Nicholas A. Eleuteri[4], Yana Pikman [1,3], Gerard M. McGeehan[12], Kimberly Stegmaier [1,3,13], Anthony Letai [9], Eric S. Fischer [4,5], X. Shirley Liu [6,7] and Scott A. Armstrong [1,3] ✉

Acute myeloid leukemia (AML) remains difficult to treat and requires new therapeutic approaches. Potent inhibitors of the chromatin-associated protein MENIN have recently entered human clinical trials, opening new therapeutic opportunities for some genetic subtypes of this disease. Using genome-scale functional genetic screens, we identified IKAROS (encoded by *IKZF1*) as an essential transcription factor in *KMT2A* (*MLL1*)-rearranged (*MLL*-r) AML that maintains leukemogenic gene expression while also repressing pathways for tumor suppression, immune regulation and cellular differentiation. Furthermore, IKAROS displays an unexpected functional cooperativity and extensive chromatin co-occupancy with mixed lineage leukemia (MLL)1–MENIN and the regulator MEIS1 and an extensive hematopoietic transcriptional complex involving homeobox (HOX) A10, MEIS1 and IKAROS. This dependency could be therapeutically exploited by inducing IKAROS protein degradation with immunomodulatory imide drugs (IMiDs). Finally, we demonstrate that combined IKAROS degradation and MENIN inhibition effectively disrupts leukemogenic transcriptional networks, resulting in synergistic killing of leukemia cells and providing a paradigm for improved drug targeting of transcription and an opportunity for rapid clinical translation.

K MT2A (*MLL1*) gene chromosomal translocations (*MLL*-r) define a distinct subset of AML[1,2] characterized by well-defined pathologic features and a dismal prognosis. *MLL*-r AML serves as a paradigm for malignant disease that is driven by disordered gene expression[3]. Normal hematopoiesis is governed by a hierarchy of transcription factors (TFs) that mediate cell fate decisions while cooperating within densely interconnected co-regulatory circuits[4]. The MLL fusion drives leukemia through deregulation of these critical transcriptional networks, functioning within multi-component protein complexes containing key structural proteins and enzymes, including MENIN[5], LEDGF[6], DOT1L[7,8] and the super-elongation complex (SEC)[9]; each of which is important for MLL fusion function. Acting within these complexes, the MLL fusion drives the abnormal expression of numerous hematopoietic TFs such as those encoded by *MEF2C*[10,11], *CDK6* (ref. [12]), *HOXA9* (ref. [13]), *PBX3* (ref. [14]) and *MEIS1* (ref. [15]), which, in turn, mediate downstream transcriptional deregulation. These TFs interact with additional myeloid transcriptional regulatory proteins such as CEBPα[16], RUNX1 (ref. [17]), MLL3 (encoded by *KMT2C*)[18], PU.1 (encoded by *SPI1*)[19] and JMJD1C[20], thereby

impacting diverse cellular processes. Of these downstream oncogenic collaborators, *HOXA* cluster genes and *MEIS1*, the products of which act together, are considered among the most important due to their ability to recapitulate much of the oncogenic function of the MLL fusion protein[13,21]. Considered broadly, the MLL fusion protein acts within a complex network of transcriptional regulators that are essential for its leukemogenicity, and elucidating strategies to shut down these pathways has been a major focus of therapeutic development for this disease. Furthermore, mechanisms that govern MLL fusion protein-driven gene expression are also critical for leukemia development in other subtypes of AML; of particular importance, high-level *HOX* and *MEIS* gene expression is observed in *NPM1*-mutant (*NPM1c*) AML[22].

Deregulated transcription is an established hallmark of malignant disease[23] and a major target for the development of cancer therapeutics. *MLL*-r leukemia serves as a model disease for this approach. Highly specific and potent small-molecule inhibitors have been developed to target the MENIN–MLL1 protein–protein interaction (VTP-50469 (ref. [24]), MI-503/463 (ref. [25]) and MI-3454 (ref. [26])) and also the enzymatic function of the histone 3 lysine

79 (H3K79) methyltransferase DOT1L (EPZ-5676 (refs. [27,28])) as a means to target the MLL fusion protein-containing complex and downstream leukemia-promoting transcription. These drugs exhibit potent anti-leukemic effects in preclinical models of both *MLL*-r and *NPM1*c leukemia[22,24,26,29]. Clinical-grade compounds related to VTP-50469 and MI-3454 have now entered phase I–II clinical studies (Syndax (SNDX-5613) and Kura (KO-539), respectively). The DOT1L inhibitor EPZ-5676 (Epizyme, pinometostat) has completed a phase I–II clinical study[30], demonstrating on-target activity in humans but achieving only modest therapeutic effect, which highlights the need to understand resistance mechanisms and develop drug combinations to improve efficacy. Combination therapies are typically superior to monotherapy because they can abrogate resistance mechanisms, which is of particular importance for therapeutic targeting of transcriptional networks due to the presence of large multiprotein complexes containing cooperating TFs with functional redundancies that may be inefficiently targeted by a single drug alone[31]. With MENIN and DOT1L inhibitors entering clinical trials as single-agent therapies, we sought to investigate how mechanisms of resistance may limit their clinical application and inform the rational development of more effective drug combinations. Remarkably, we identified IKAROS (encoded by *IKZF1*) as an essential transcriptional regulator in *MLL*-r and *NPM1*c AML that can be immediately exploited using IMiDs; furthermore, we found that combined therapeutic targeting of IKAROS and MENIN leads to synergistic anti-proliferative effects and propose this as a new therapeutic strategy for AML.

Results
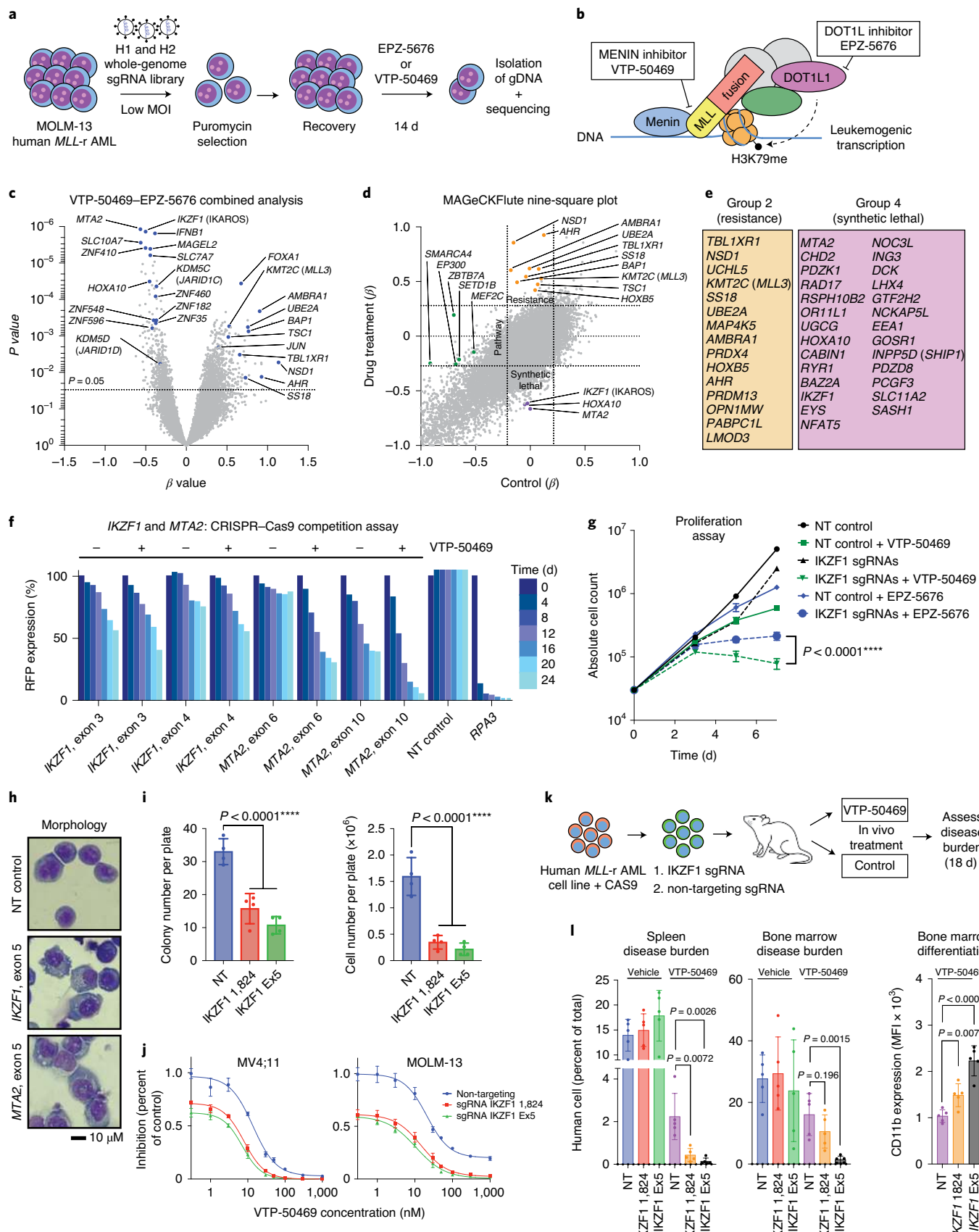
IKAROS (*IKZF1*) modulates dependency on MLL1–MENIN and DOT1L. Genome-scale, CRISPR–Cas9-based functional genetic screening was used to characterize resistance mechanisms and synthetic lethal interactions for small-molecule inhibitors of DOT1L or MENIN (EPZ-5676 and VTP-50469, respectively) using the human *MLL*-r AML cell line MOLM-13 (Fig. 1a). These drugs target the MLL fusion complex[3] (Fig. 1b). Cell proliferation was monitored during the screen (Extended Data Fig. 1a), showing strong inhibition. Comparison of the drug-treatment group to the vehicle control on day 14 (Supplementary Table 1) revealed selection for single-guide (sg)RNA species targeting transcriptional regulators (Extended Data Fig. 1b) and a strong overlap between the two drugs (Extended Data Fig. 1c). Leading edge analysis, focusing on resistance genes (group 2) and synthetic lethal genes (group 4), according to the MAGeCKFlute computational pipeline[32], highlighted genes exerting a large effect size in both screens (Fig. 1e)
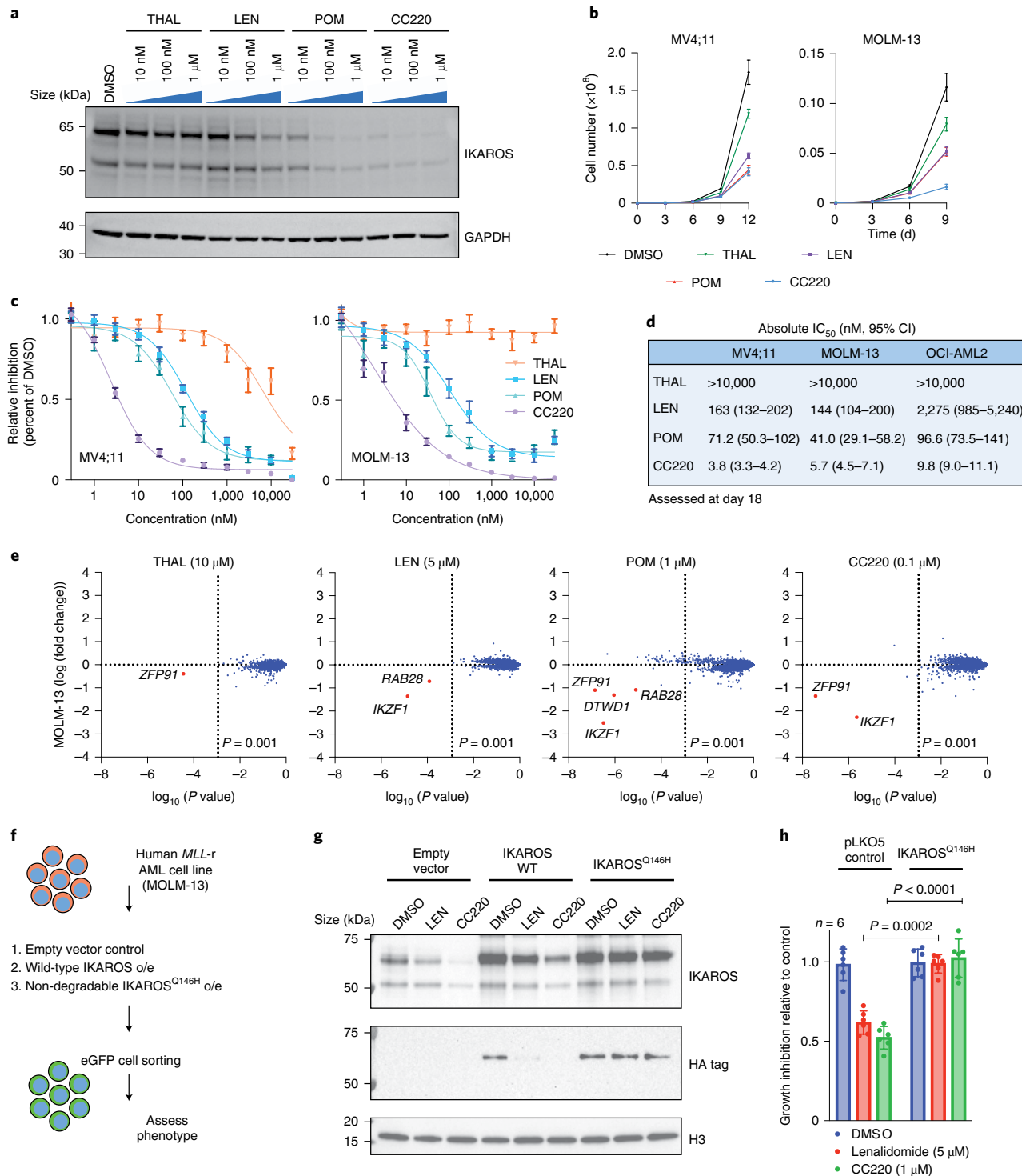
and common mechanisms of resistance. A combined analysis of the two screens highlighted these common pathways (Fig. 1c and Supplementary Table 1); *IKZF1* (IKAROS) and *MTA2* were the two highest-scoring negatively selected genes, which are notable as constituents of the nucleosome remodeling and histone deacetylase complex (NuRD)[33]. Other high-ranking genes that were depleted or enriched included those encoding members of the SWI–SNF complex (*SMARCA4*, *SS18*), the mTOR pathway (*TSC1*, *TSC2*, *PTEN*), protein-ubiquitination regulators (*UBE2A*, *BAP1*, *TBL1XR1*, *AMBRA1*, *UCHL5*, *RNF138*, *NOSIP*), regulators of histone methylation (*KDM5D* (JARID1D), *KDM5C* (JARID1C), *SETD1B*, *NSD1*, *KMT2C* (MLL3), *PRDM13*), TFs (*FOXA1*, *HOXA10*, *HOXB5*, *MEF2C*, *AHR*) and zinc finger proteins (*ZNF410*, *ZNF460*, *ZNF182*, *ZNF548*, *ZNF596*). MAGeCKFlute was used to correct cell cycle biases and classify hits into functional categories (Fig. 1d)[32]. This highlighted *IKZF1*, *MTA2* and *HOXA10* as synthetic lethal gene targets, because they were disproportionately depleted in drug-treated cells, and identified these genes as therapeutic targets that may increase sensitivity to inhibition of MENIN and DOT1L. IKAROS is an established therapeutic target in lymphoproliferative disorders, but a role in *MLL*-r AML has not been previously reported. Notably, *IKZF1* exhibits high-level gene expression in human AML[34,35] and is also detected as an AML dependency in the Broad DepMap dataset ($P = 3.8 \times 10^{-12}$); across all cancer cell lines in the DepMap dataset, there is a significant correlation of dependency between *MEN1* and *IKZF1* expression (Pearson, 0.15; *P* value, 5.3×10^{-7}) and between *DOT1L* and *IKZF1* expression (Pearson, 0.19; *P* value, 5.7×10^{-10})[35]. We next evaluated the impact of genetic targeting of both *IKZF1* and *MTA2* using CRISPR–Cas9-based competition assays, using lentiviral vectors coexpressing an sgRNA and red fluorescence protein (RFP) in four different Cas9-expressing human *MLL*-r AML cell lines (MOLM-13, MV4;11, OCI-AML2 and THP-1), revealing strong depletion of sgRNA species targeting *IKZF1* and *MTA2* (Fig. 1f and Extended Data Fig. 1d). Addition of VTP-50469 enhanced sgRNA depletion (Fig. 1f and Extended Data Fig. 2a) as predicted by the genetic screen. To generalize this finding to other leukemia subtypes, two *NPM1*c cell lines (IMS-M2 and OCI-AML3) and two non-*MLL*-rearranged leukemia lines (U937 and HL60) were examined (Extended Data Fig. 1e); importantly, U937 and HL60 did not display IKAROS dependency and, notably, are also insensitive to MENIN inhibition[24], highlighting a context-dependent role for IKAROS. By contrast, both *NPM1*c cell lines exhibited strong IKAROS dependency in accordance with their overlapping gene expression profile with *MLL*-r AML[36] and dependency on DOT1L and MENIN[22], suggesting that IKAROS and MENIN may be

---

Fig. 1 | *IKZF1* (IKAROS) and *MTA2* exhibit synthetic lethal interaction with pharmacologic inhibition of MENIN and DOT1L. a, Functional genetic screen schematic: cells were treated with EPZ-5676 (1 μM), VTP-50469 (500 nM) or vehicle. MOI, multiplicity of infection. **b,** Drug targeting of MENIN (VTP-50469) and DOT1L (EPZ-5676) disrupts MLL fusion complex function. H3K79me, methylated H3K79. **c,** Volcano plot depicting Wald *P* and *β* values calculated using the MAGeCK MLE function for the VTP-50469 and EPZ-5676 combined analysis comparing vehicle-treated (*n* = 2) and drug-treated (*n* = 4) states on day 14. **d,** MAGeCKFlute nine-square correlation plot using the *β* value calculated between day 0 and day 14 for vehicle treatment as compared to drug treatment (VTP-50469 and EPZ-5676 screens combined). Regions corresponding to pathway (group 1), resistance (group 2) and synthetic lethal (group 4) genetic hits are indicated. **e,** Leading edge analysis from GSEA showing overlapping genetic hits for each screen considered separately. **f,** CRISPR–Cas9-based competition assays targeting either *IKZF1* or *MTA2*, monitoring sgRNA-RFP expression over time in the Cas9-expressing MOLM-13 AML cell line with or without VTP-50469. NT, non-targeting. **g,** Proliferation assay on sorted, sgRNA-RFP-expressing cells with or without VTP-50469 or EPZ-5676. Data represent mean ± s.e.m. (*n* = 3) with the *P* value calculated using a paired, two-tailed *t*-test. **h,** Cell morphology was assessed using light microscopy (100×) 7 d following CRISPR–Cas9-mediated deletion of *IKZF1* or *MTA2* compared to that of the non-targeting sgRNA control. **i,** Colony-forming assay comparing MOLM-13 cells with an sgRNA targeting the luciferase gene (non-targeting control) to cells with two different sgRNA species targeting *IKZF1* (*n* = 4 per sgRNA). Data represent mean ± s.e.m. *P* values were determined by unpaired, two-tailed *t*-tests. Ex, exon. **j,** Proliferation assay comparing MOLM-13 cells with an sgRNA targeting the luciferase gene (non-targeting control) and cells with two sgRNA species targeting *IKZF1* (*n* = 3 per sgRNA) upon VTP-50469 treatment for 5 d. Data represent mean ± s.e.m. **k,** Schematic for the in vivo MOLM-13 xenograft experiment: 200,000 MOLM-13 cells with an sgRNA targeting the luciferase gene (non-targeting control) versus cells with two different sgRNA species targeting *IKZF1* (*n* = 5 per group) were injected via the tail vein on day 0, treatment began with VTP-50469 administered in chow on day 9, and mice were killed on day 18 when they became ill. **l,** MOLM-13 xenograft experiment, disease burden and differentiation markers in spleen and bone marrow after 9 d of VTP-50469 treatment. Data represent mean ± s.e.m. *P* values were determined by unpaired, two-tailed *t*-tests. MFI, mean fluorescence intensity.
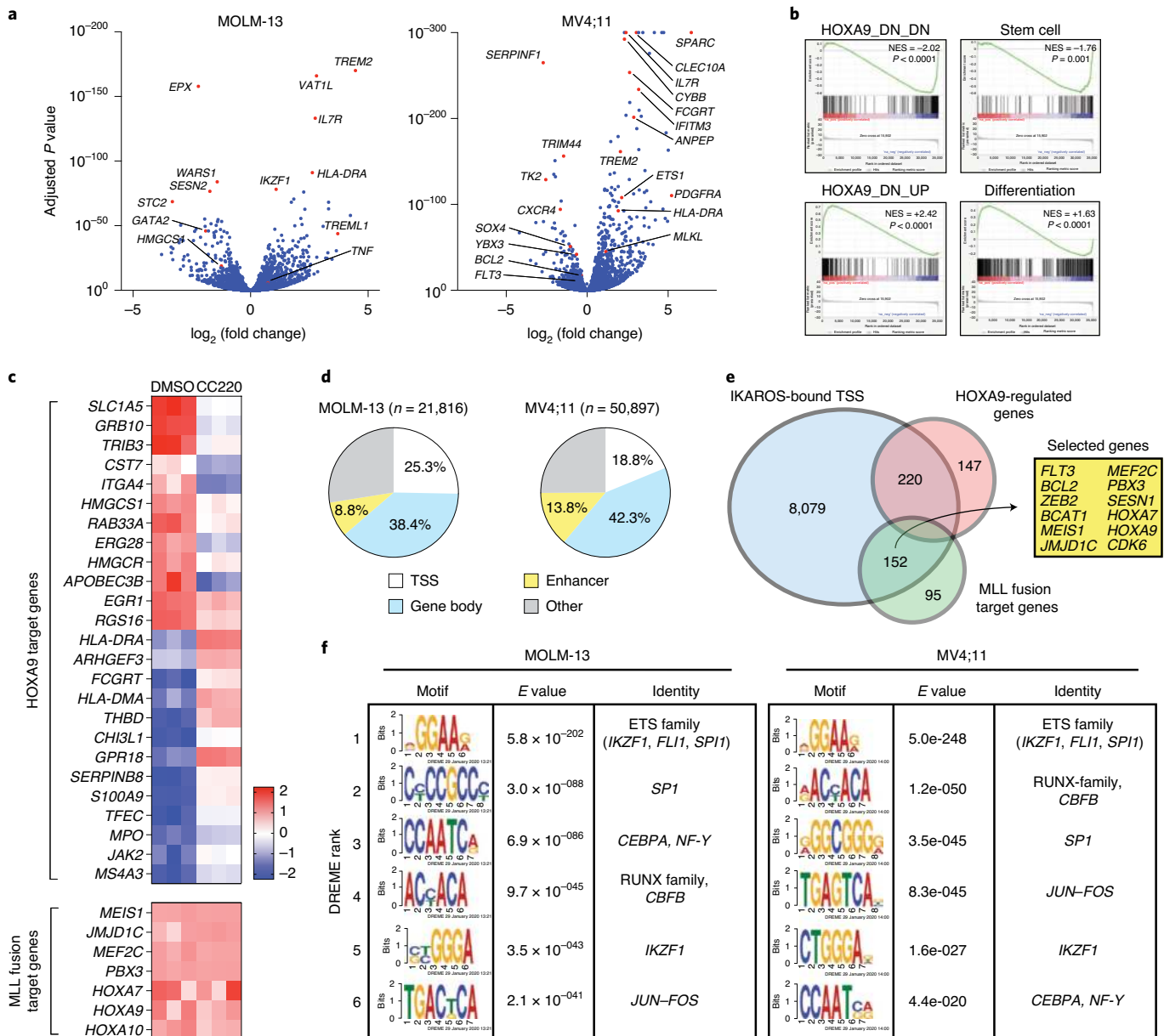
co-dependencies. CRISPR–Cas9-mediated depletion of IKAROS and metastasis-associated 1 family member 2 (MTA2) protein was confirmed by western blot (Extended Data Fig. 2b,c). Cell proliferation

was measured following *IKZF1* knockout with and without MENIN or DOT1L inhibition, revealing a modest reduction in cell proliferation that was enhanced when combined with either the MENIN or

a MOLM-13 human *MLL*-r AML; H1 and H2 whole-genome sgRNA library, Low MOI; Puromycin selection; Recovery; EPZ-5676 or VTP-50469, 14 d; Isolation of gDNA + sequencing

b MENIN inhibitor VTP-50469; DOT1L inhibitor EPZ-5676; Menin; MLL; fusion; DOT1L1; Leukemogenic transcription; DNA; H3K79me

c VTP-50469–EPZ-5676 combined analysis

d MAGeCKFlute nine-square plot

e Group 2 (resistance) / Group 4 (synthetic lethal)

f *IKZF1* and *MTA2*: CRISPR–Cas9 competition assay

g Proliferation assay; *P* < 0.0001****

h Morphology

i *P* < 0.0001****

j MV4;11 / MOLM-13

k Human *MLL*-r AML cell line + CAS9; 1. IKZF1 sgRNA 2. non-targeting sgRNA; VTP-50469 In vivo treatment / Control; Assess disease burden (18 d)

l Spleen disease burden / Bone marrow disease burden / Bone marrow differentiation

Fig. 2 | IMiDs effectively target the IKAROS protein for degradation and show therapeutic efficacy in *MLL*-r AML. a, Western blot analysis for IKAROS protein following treatment of the MOLM-13 cell line for 5 h with increasing doses of THAL, LEN, POM and CC220, using glyceraldehyde-3-phosphate dehydrogenase (GAPDH) as a loading control. **b**, Proliferation assay measuring cell number over time for the MV4;11 and MOLM-13 cell lines treated with vehicle control (dimethyl sulfoxide (DMSO)), THAL, LEN, POM and CC220. Data represent mean ± s.d. ($n = 3$). **c**, Dose–response curves for MV4;11 and MOLM-13 cell lines with THAL, LEN, POM and CC220 treatment. Data represent mean ± s.d. ($n = 6$) with non-linear regression curve fits shown. Percentage is indicated as a proportion. **d**, Calculated absolute IC_{50} and 95% confidence intervals (CI) for MOLM-13, OCI-AML2 and MV4;11 AML cell lines, assessed by the proliferation assay at day 18. **e**, Scatterplot for MS determination of IMiD substrates 5 h after the indicated drug treatment in the MOLM-13 cell line. Data represent the log fold change in abundance and $\log_{10}$ (P values). P values were determined by moderated t-test as implemented with the Bioconductor limma package. **f**, Schematic depicting generation of MOLM-13 cell lines with IKAROS-overexpression (o/e) constructs treated with DMSO, LEN (5 μM) and CC220 (1 μM) for 5 h. **g**, Western blot showing IKAROS-overexpression constructs. HA, hemagglutinin; WT, wild type. **h**, Proliferation assay showing rescue of anti-proliferative effects with overexpressed, non-degradable IKAROS (Q146H). Data represent mean ± s.e.m. P values were determined by paired, two-tailed t-tests.

Fig. 3 | IKAROS is a core transcriptional regulator in *MLL*-r AML. a, Volcano plots displaying RNA-seq data for MOLM-13 ($n = 3$) and MV4;11 ($n = 3$) cell lines treated with CC220 at $1\,\mu$M for 3 d. Selected genes are indicated. **b**, Barcode plots depicting GSEA results for HOXA9-regulated genes, stem cell genes and myeloid differentiation in the MOLM-13 cell line. Normalized enrichment scores (NES) and family-wise error rate P values were determined by the GSEA computational method. HOXA9_DN_DN and MYC_UP_UP indicate the names of gene sets from the Broad Molecular Signatures Database. **c**, Heatmap depicting gene expression z scores for canonical MLL1 fusion target genes and selected HOXA9-regulated genes following 3 d of treatment with CC220 compared to expression in the DMSO control in the MOLM-13 cell line. **d**, Percentage of ChIP–seq IKAROS peaks with fivefold enrichment over background at regulatory regions as indicated. **e**, Venn diagram depicting overlap between all TSS-proximal IKAROS peaks with genes within the MLL fusion and HOXA–MEIS1 network. **f**, CUT&RUN de novo DREME motif detection results for the MOLM-13 and MV4;11 cell lines. The top six motifs detected for IKAROS are shown in order of statistical significance. Motifs, statistical E values and predicted motif identities are indicated.

DOT1L inhibitor (Fig. 1g); *IKZF1* knockout in combination with MENIN inhibition resulted in the strongest overall anti-proliferative effect, shifting the half-maximum inhibitory concentration (IC_{50}) of MENIN inhibition (Fig. 1j and Extended Data Fig. 2f) and substantially increasing the amount of apoptosis induced with MENIN inhibition (Extended Data Fig. 2g). Remarkably, loss of either *IKZF1* or *MTA2* led to cellular differentiation, induction of apoptosis (Extended Data Fig. 2d) and morphologic changes consistent with monocytic differentiation (Fig. 1h), indicating that *IKZF1* and the NuRD complex have a fundamentally important role in leukemia

maintenance. Additionally, *IKZF1* loss impaired colony formation in colony-forming assays (Fig. 1i and Extended Data Fig. 2e), and, in a MOLM-13 xenograft experiment, *IKZF1* knockout enhanced MENIN inhibition in terms of reducing disease burden and increasing differentiation markers in vivo (Fig. 1k,l), further implicating *IKZF1* as essential to *MLL*-r leukemia maintenance.

IMiDs efficiently drive IKAROS protein degradation in AML.
We next sought to leverage this finding by targeting the IKAROS protein in AML using IMiDs. Lenalidomide (LEN) and related

thalidomide (THAL) analogs promote cereblon (CRBN)-mediated degradation of the neo-substrates IKAROS, AIOLOS[37,38], casein kinase 1α (CK1α)[39] and others. THAL and newer-generation IMiDs, LEN, pomalidomide (POM) and iberdomide (CC220), display differing neo-substrate profiles and potency of IKAROS protein degradation[40]. Detailed evaluation of these drugs in *MLL*-r AML has not been previously reported. Thus, we evaluated all four drugs for potency of IKAROS degradation in three *MLL*-r human AML cell lines (Fig. 2a and Extended Data Fig. 3a,b); increasing potency of IKAROS degradation was observed for THAL, LEN, POM and CC220. Each IMiD impaired cell proliferation in a manner correlating with the degree of IKAROS degradation (Fig. 2b), and, notably, a defect in proliferation was not observed until 6–9 d. The therapeutic dose–response relationship was strongly correlated with the degree of IKAROS degradation (CC220≫POM>LEN≫THAL) (Fig. 2c,d). In accordance with genetic deletion, IMiD treatment also impaired proliferation of the *NPM1*c AML cell lines IMS-M2 and OCI-AML3 (Extended Data Fig. 3c). A detailed neo-substrate profile for each drug in all three *MLL*-r cell lines tested (MV4;11, MOLM-13, OCI-AML2) was determined using multiplexed mass spectrometry (MS)-based global proteomics. This confirmed IKAROS as the primary neo-substrate (Fig. 2e, Extended Data Fig. 3d and Supplementary Table 2) without obvious new neo-substrate degradation detected; notably, *ZFP91* and *ZNF692* were not detected as AML dependencies in the DepMap dataset (data not shown). CK1α peptides were not efficiently detected by MS but were confirmed by western blot analysis to only be a substrate of LEN (Extended Data Fig. 3a,b); CC220 elicited the most potent inhibitory effect on cell growth while exhibiting profound IKAROS degradation and minimal effect on CK1α, consistent with IKAROS being the primary substrate mediating these effects. Furthermore, overexpression of a non-degradable IKAROS mutant with a single amino acid substitution rendering it incapable of being degraded (Q146H)[38] rescued the anti-proliferative effects of IMiDs (Fig. 2f–h). Altogether, these data support IMiDs as a potential new therapeutic approach for *MLL*-r AML through their ability to degrade the IKAROS protein.
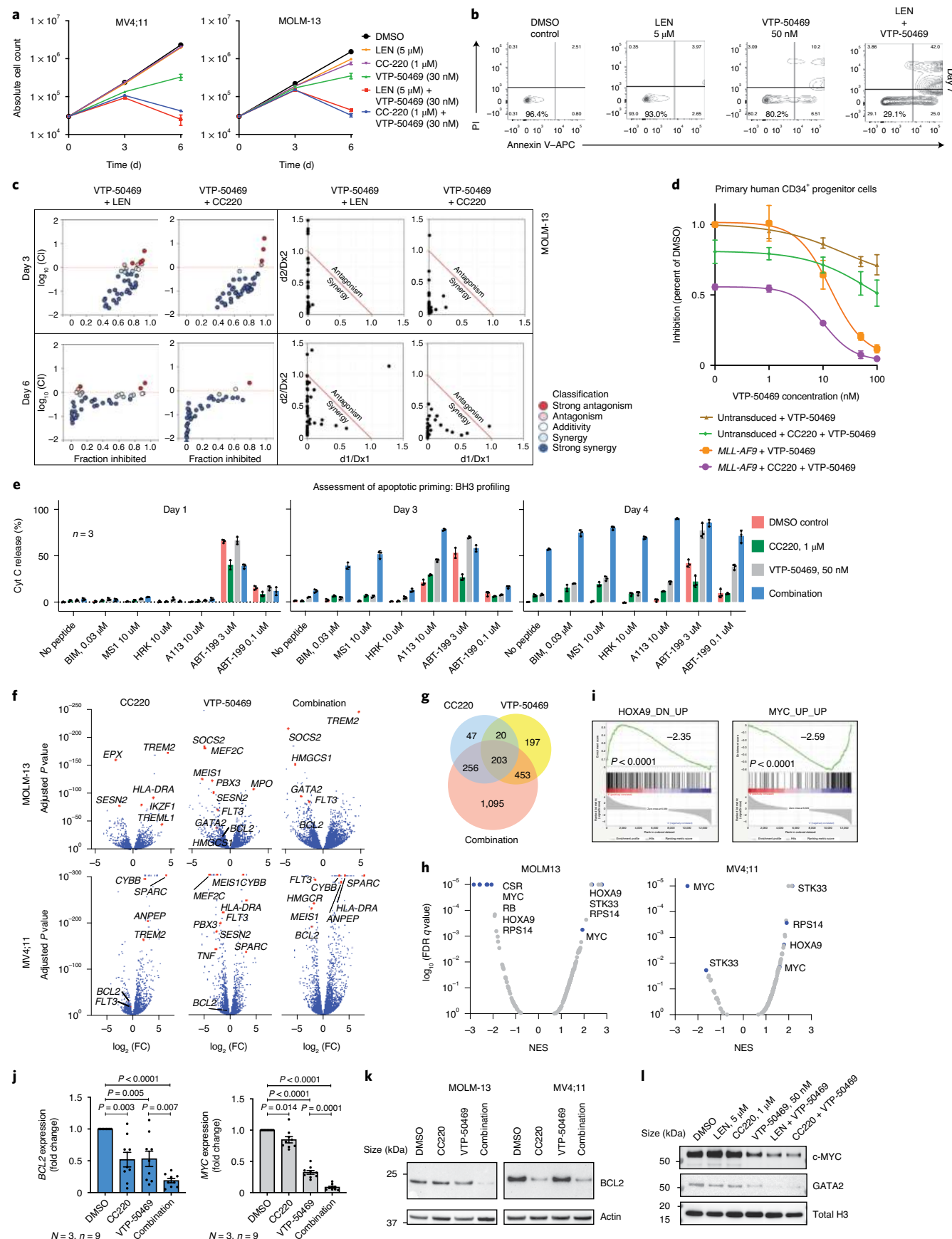
IKAROS is a core transcriptional regulator in *MLL*-r AML. We next determined the transcriptional changes following IKAROS degradation in *MLL*-r AML using RNA sequencing (RNA-seq) (Fig. 3a and Supplementary Table 3). LEN and CC220 treatment resulted in highly correlated gene expression changes (Extended Data Fig. 4a).
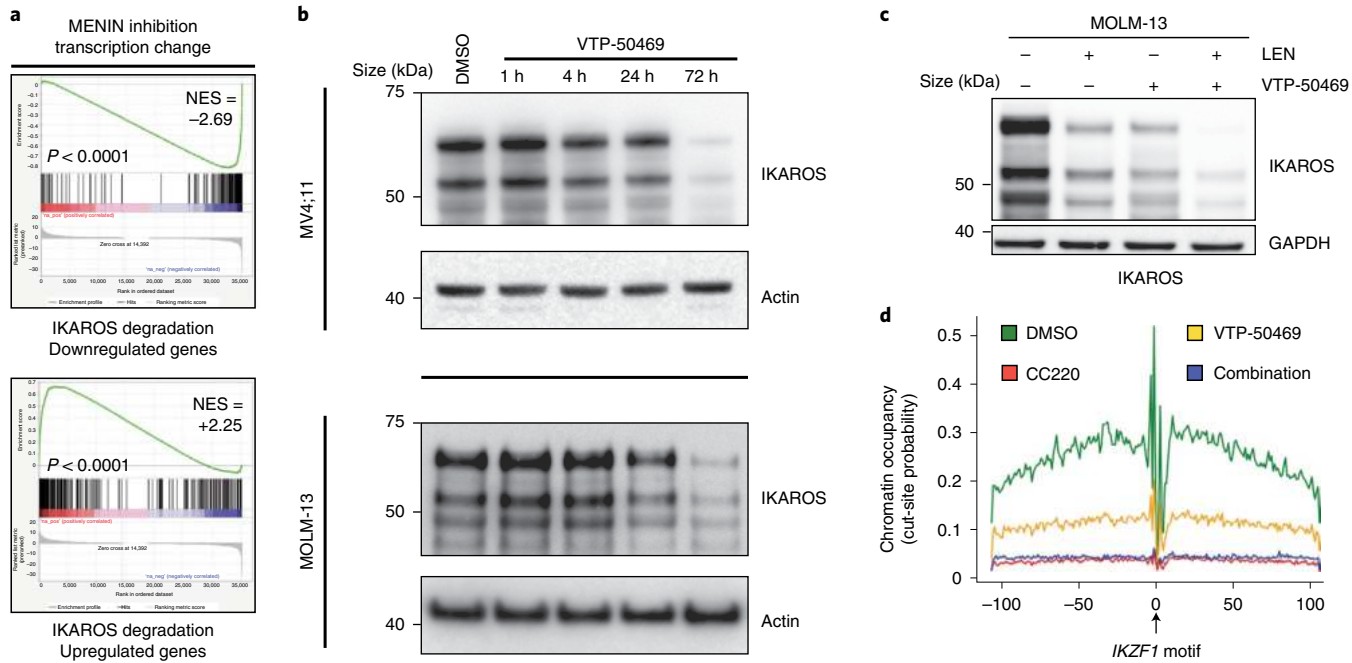
Gene set enrichment analysis (GSEA) highlighted gene expression changes related to *HOXA9* (Fig. 3b), stem cell biology, myeloid differentiation, the mTOR pathway, inflammatory and immune signaling and cell death regulators (Extended Data Fig. 4c,d). Remarkably, after 6 d of LEN treatment, the critical pro-survival gene *BCL2* was the most significantly downregulated gene in the MV4;11 cell line (Extended Data Fig. 4b and Supplementary Table 3). IKAROS degradation resulted in induction of gene expression associated with myelomonocytic differentiation and loss of stem cell-associated genes (Fig. 3b), demonstrating therapeutic response at the level of transcription and indicating that IKAROS is required to sustain the differentiation block. IMiD treatment perturbed the expression of HOXA9 target genes without impacting the expression of the *HOXA9* gene itself or other canonical MLL fusion target genes (Fig. 3c), implicating a functional interaction between IKAROS and HOXA–MEIS1. The HOXA–MEIS1 transcriptional program is considered critical for the oncogenicity of the MLL fusion protein[13,21] and is a shared feature with *NPM1*c AML[36]. More broadly, IKAROS loss impacted non-canonical MLL fusion target genes, including *FLT3* and *BCL2* (Extended Data Fig. 4e)[8,41]. Prominently, IMiD treatment strongly activated pathways involving the immune response (*SOX4*, *SOCS2*, TREM signaling, the TNF pathway, IL-6–STAT signaling, HLA gene expression) (Extended Data Fig. 4f), also suggesting an important role for IKAROS in immune regulation in AML.

We next defined genome-wide chromatin occupancy for IKAROS using a combination of chromatin immunoprecipitation followed by next-generation DNA sequencing (ChIP–seq) and the cleavage under target and release using nuclease (CUT&RUN) assay[42–44]. To delineate IKAROS occupancy at functional regulatory regions, we defined a genome-wide map of enhancers and enhancer–promoter connections using the activity-by-contact (ABC) model[45]. ChIP–seq revealed widespread IKAROS binding in MOLM-13 (21,816 peaks showing more than fivefold enrichment over background) and MV4;11 (50,897 peaks at more than fivefold enrichment) cells with frequent occupancy in proximity to transcriptional start sites (TSSs) (<1 kb from the TSS) and at enhancers (Fig. 3d) (see also Fig. 6b,c, Extended Data Fig. 8b,c and Supplementary Table 4). In MOLM-13 cells, 8,079 genes exhibited an IKAROS peak in proximity to the TSS, including many MLL fusion- and HOXA9-regulated genes (Fig. 3e). A context-dependent role for IKAROS was observed with substantial cell line-specific gene expression changes (Extended Data Fig. 4g). Globally, IKAROS-bound TSSs were strongly

Fig. 4 | Combined targeting of MENIN and IKAROS results in synergistic induction of apoptosis and cooperative deregulation of gene expression.
a, Proliferation assay measuring cell numbers over time for the MV4;11 and MOLM-13 cell lines following drug treatment. Data represent mean ± s.d. (*n* = 3). **b**, Analysis of annexin V staining (apoptosis) following drug treatment. Viable cell percentages are indicated. A representative experiment is shown. PI, propidium iodide. **c**, Synergy analysis of proliferation assays using VTP-50469 in combination with LEN or CC220. Chou-Talalay Combination Index (CI) plots (left panel) and normalized isobolograms depicting CI scores over a range of concentrations (right panel) for each drug combination. The coordinates of the CI scores are d1/Dx1 and d2/Dx2, where Dx1 is the concentration of drug 1 (IMiD) that alone produces the fractional inhibition effect *x*, and Dx2 is the concentration of drug 2 (VTP-50469) that alone produces the fractional inhibition effect x. Line of additivity shown (red). **d**, Proliferation assay after a 6-d treatment of human CD34+ progenitor cells that were not transformed versus CD34+ progenitor cells transformed with *MLL-AF9*. Data represent mean ± s.e.m. (*n* = 3) relative to the DMSO control. **e**, BH3 profiling in MOLM-13 cells following drug treatments. Cytochrome C (Cyt C) release was measured. Data represent mean ± s.e.m. (*n* = 3). **f**, Volcano plots displaying RNA-seq data for MOLM-13 and MV4;11 cells following 3 d of drug treatment (*n* = 3 per condition). FC, fold change. **g**, Venn diagram for overlapping transcriptional changes between CC220, VTP-50469 and the combination treatment (total number of genes with more than twofold change and *P* adjusted <0.05 is indicated as determined by the DESeq2 package). **h**, GSEA results querying the Broad 'oncogenic signatures', comparing combination treatment with VTP-50469 monotherapy. Results are displayed as dot plots of the $\log_{10}$ (false discovery rate (FDR) *q* value) and normalized enrichment scores. RB, RB1; CSR, Broad Molecular Signatures Database gene set CSR_LATE_UP.V1_UP. **i**, Barcode plots depicting selected GSEA results in MOLM-13 cells from **h**. The additive effect of the combination compared to VTP-50469 therapy alone is depicted. Normalized enrichment scores and family-wise error rate *P* values were determined by the GSEA computational method. **j**, *BCL2* and *MYC* gene expression assessed by quantitative reverse transcription PCR (RT-qPCR) following treatment with CC220 at 1 μM, VTP-50469 at 250 nM and the combination. Data represent mean ± s.e.m. for the combined analysis of three AML cell lines (MOLM-13, MV4;11 and OCI-AML2) with *n* = 3 replicates each (*N* = 3, *n* = 9). *P* values were determined by paired, two-tailed *t*-tests. **k**, Western blot for BCL2 protein following treatment of MOLM-13 and MV4;11 cells for 72 h with CC220 at 1 μM, VTP-50469 at 50 nM and in combination, using actin as a loading control. **l**, Western blot for MYC and GATA2 protein following drug treatment of MOLM-13 cells for 72 h. Histone H3 was used as a loading control.

Fig. 5 | Inhibition of MENIN–MLL1 protein–protein interaction leads to proteasomal degradation of IKAROS protein. a, Barcode plots depicting the effect of MENIN inhibition on the set of genes deregulated following IKAROS degradation during CC220 treatment according to RNA-seq data on day 3. Normalized enrichment scores and family-wise error rate *P* values were determined by the GSEA computational method. **b**, Western blot analysis for IKAROS protein following treatment of the MV4;11 and MOLM-13 cell lines for 1, 4, 24 and 72 h, using actin as a loading control. **c**, Western blot analysis for IKAROS protein following treatment of the MOLM-13 human *MLL*-r AML cell line for 72 h with LEN, VTP-50469 and in combination, using GAPDH as a loading control. **d**, IKAROS protein chromatin binding at the *IKZF1* motif displayed as the cut-site probability ±100 bp around the *IKZF1* motif under each drug treatment as indicated.

predictive of gene expression changes (Extended Data Fig. 4h) with a modest predominance of activated gene expression. Extensive IKAROS occupancy was also noted at enhancers (including those for *MYC*, *BCL2*, *FLT3*, *MYB* and *TNF*), and this also correlated with gene expression changes using enhancer–gene connection predictions by the ABC model. Notably, many genes exhibited IKAROS peaks at their TSS as well as at a connecting enhancer (see also Fig. 6b,c and Extended Data Fig. 8b,c), and approximately 30% of all genes deregulated following IMiD treatment were found to have an associated IKAROS-bound enhancer (Extended Data Fig. 4i). We next used CUT&RUN to define the repertoire of TF-binding motifs present at IKAROS-bound sites. Discriminative regular expression motif elicitation (DREME) detected two motifs with homology to reported *IKZF1* motifs (Extended Data Fig. 5a) among the highest-ranking motifs in both cell lines (Fig. 3f); CCCTC-binding factor (CTCF) and immunoglobulin (Ig)G were used as positive and negative controls, respectively (Extended Data Fig. 5b,c). IKAROS peaks were detected at motifs for critical myeloid TFs (Fig. 3f and Extended Data Fig. 5d) including those for the ETS family (*FLI1*, *SPI1* (PU.1)) and those encoded by *RUNX1–RUNX3* and *CBFB*; *SP1*; *CEBPA*, *NFYA* and *NFYB*; and *JUN* and *FOS*. Notably, all of these TFs play an important role in transcriptional deregulation by the MLL fusion protein, placing IKAROS within this critical transcriptional network. Overall, these findings position IKAROS as a core transcriptional regulator in *MLL*-r AML.

Co-targeting MENIN and IKAROS drives synergistic cell death.
We next evaluated combined IKAROS degradation using IMiDs and MENIN inhibition with VTP-50469. Combined treatment resulted in more potent anti-proliferative effects compared to VTP-50469 treatment alone (Fig. 4a). VTP-50469 drives a cellular response typified by cell cycle arrest and differentiation[24]; however,

when used in combination with IMiDs, early loss of cell number was observed due to marked, early induction of apoptosis (Fig. 4b and Extended Data Fig. 6a), representing a potent switch from VTP-50469-induced differentiation to apoptotic cell death. IMiD treatment alone was sufficient to produce immunophenotypic evidence of differentiation and cell cycle arrest, and this was enhanced with combination treatment (Extended Data Fig. 6b,c). The IMiD–VTP-50469 combination displayed synergy, with the response correlating with the potency of IKAROS degradation (CC220 > LEN) (Fig. 4c and Extended Data Fig. 6d,e). The IMiD effect was rescued by overexpression of a non-degradable IKAROS mutant (Extended Data Fig. 6f,g). To assess for toxicity to normal hematopoietic cells, we treated untransformed CD34+ cells and *KMT2A-MLLT3* (MLL-AF9)-transformed CD34+ cells, demonstrating a potential therapeutic window (Fig. 4d). Given the profound apoptotic response, we used MS to exclude the possibility that concomitant VTP-50469 treatment may alter the IMiD neo-substrate profile (Extended Data Fig. 6h and Supplementary Table 2). To characterize the mechanism of enhanced apoptosis, we evaluated apoptotic priming according to mitochondrial sensitivity to pro-apoptotic BCL-2 homology domain 3 (BH3) peptides and small molecule BH3 mimetics (BH3 profiling)[46]. At baseline, the MV4;11 and MOLM-13 cell lines were primarily dependent on BCL2 for survival, based on mitochondrial sensitivity to BCL2-selective ABT-199 (day 1; Fig. 4e and Extended Data Fig. 6i). With combination treatment, the cells became globally primed for apoptosis (increasing BIM sensitivity on day 3), which progressed to a state of initiated apoptosis (no peptide) by day 4. On day 3, cells showed a dramatic increase in sensitivity to BH3 peptides that specifically neutralise MCL1 (MS1) and BCL-XL (HRK) and to the BCL-XL-specific small molecule BH3 mimetic A-1331852 (A113), which is in keeping with loss of *BCL2* expression following IKAROS degradation (Extended Data Fig. 6j)

while MCL1 and BCL-XL protein levels remained unchanged. Remarkably, this combination converts two small molecules that primarily induce differentiation into potent inducers of cell death.

MENIN and IKAROS support leukemia-promoting transcription. We next evaluated the impact of IKAROS degradation on the transcriptional response to MENIN inhibition (Fig. 4f). Surprisingly, IMiD and VTP-50469 treatments produced strongly overlapping transcriptional changes (Fig. 4f,g), and a large number of genes were differentially expressed only with the combination. For MOLM-13 cells, 42% of all genes differentially expressed during CC220 treatment (fold change > 2) were shared with those differentially expressed during VTP-50469 treatment, and 1,095 genes (54.6% of the combination drug response) were unique to the drug combination (Extended Data Fig. 7a). Therefore, numerous genes are commonly regulated by IKAROS and MENIN (Extended Data Fig. 7b,c), and many are only perturbed under the combination treatment. GSEA identified *HOXA9* and *MYC* among pathways accentuated by the combination (Fig. 4h,i) as compared to VTP-50469 monotherapy. This finding demonstrates that, although VTP-50469 drives rapid downregulation of *MEIS1* gene expression, combined IKAROS targeting results in more profound disruption of the downstream HOX–MEIS-regulated network; importantly, combined IKAROS targeting did not impact the VTP-50469 effect on *MEIS1*, *HOXA9* or *HOXA10* gene expression. Combination treatment led to further downregulation of *MYC* and *BCL2* gene expression (Fig. 4j). Reductions in BCL2, MYC and GATA-binding protein (GATA)2) protein levels were confirmed by western blot (Fig. 4k,l), and there was loss of cell surface expression of the FMS-related receptor tyrosine kinase 3 (FLT3) protein (Extended Data Fig. 7d). Notably, *MYC*, *BCL2* and *FLT3* were all identified as strong dependencies in MOLM-13 cells (Extended Data Fig. 7e). MENIN inhibition significantly altered expression of genes also deregulated following IKAROS degradation (Fig. 5a), prompting examination of IKAROS protein levels during VTP-50469 treatment. VTP-50469 caused substantial loss of IKAROS protein over 72 h (Fig. 5b) that was additive with the IMiD–VTP-50469 combination (Fig. 5c) and associated with a compensatory increase in *IKZF1* gene expression (Extended Data Fig. 7f). VTP-50469-induced loss of IKAROS protein was partially rescued using the proteosome inhibitor bortezomib (Extended Data Fig. 7g), in keeping with IKAROS loss via proteasomal degradation. Furthermore, MENIN-inhibitor treatment led to loss of IKAROS binding proximal to TSSs (Extended Data Fig. 7h) and loss of the IKAROS footprint over the *IKZF1* motif (Fig. 5d), directly linking MENIN with regulation of IKAROS protein stability.
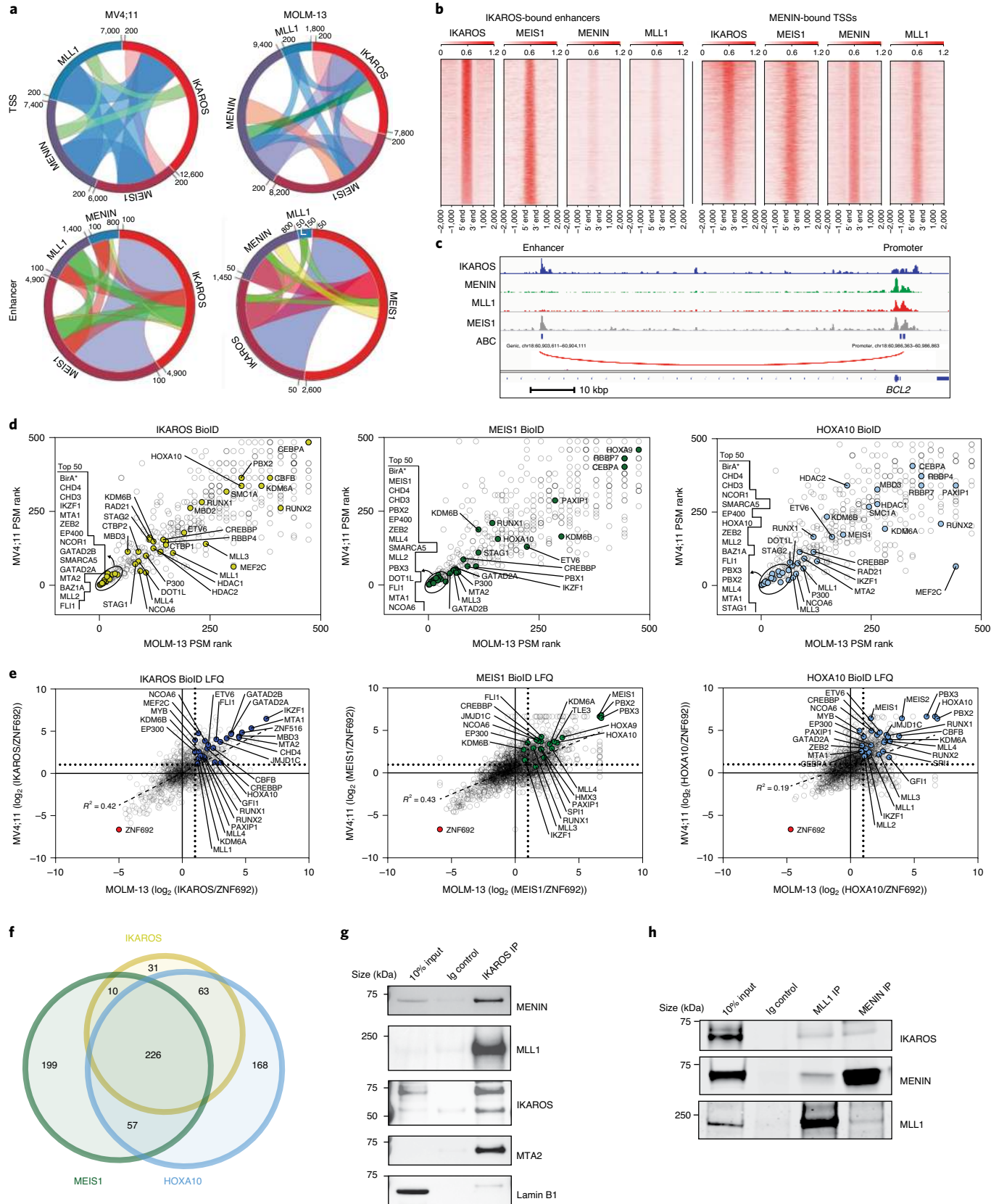
IKAROS, MENIN–MLL1 and MEIS1–HOXA chromatin co-occupancy. We next profiled the genome-wide chromatin binding of IKAROS in relation to the key regulators of these transcriptional programs: MEIS1, MLL1 and MENIN. Significant overlap was observed between IKAROS and each of the other factors (Extended Data Fig. 8a), with a high level of co-occupancy between IKAROS and MENIN proximal to TSSs and co-occupancy of IKAROS and MEIS1 at enhancers (Fig. 6a–c). MENIN-bound TSSs showed co-occupancy with IKAROS at 62.0% and 85.2% for MOLM-13 and MV4;11 cells, respectively, while IKAROS-bound enhancers showed co-occupancy with MEIS1 at 81.4% and 62.8% for MOLM-13 and MV4;11 cells, respectively. IKAROS co-occupancy peaks with MEIS1 were detected at enhancers with predicted connections to genes exhibiting IKAROS peaks proximal to the TSS (Fig. 6c and Extended Data Fig. 8b,c). Thus, IKAROS is extensively intertwined on the chromatin with MENIN, MLL1 and MEIS1. To investigate how IKAROS may be engaged in protein complexes at these locations, we examined the IKAROS, MEIS1 and HOXA10 proximal interactome using global proteomic proximity-based in-cell labeling (BioID)[47]. BioID uses an engineered promiscuous biotin ligase, BirA*, (labeling radius of ~10 nm), fused to a protein of interest enabling biotinylation of direct and proximal interacting proteins (IKAROS, MEIS1, HOXA10), and, as a control, cloning was performed to produce ZNF692–BirA* fusion proteins that were constitutively expressed in MV4;11 and MOLM-13 cells (Extended Data Fig. 8d,e). ZNF692 is a zinc finger-containing TF used as a control because it is not a dependency in *MLL*-r leukemia and was considered an inert chromatin-binding control. Stable BioID cell lines were grown in the presence of biotin for 24 h before nuclear isolation, lysis, streptavidin capture of biotinylated proteins, on-bead tryptic digestion and LC–MS/MS analysis. Proteins were first ranked by peptide spectral matches (PSMs) (Fig. 6d and Supplementary Table 7); IKAROS BioID strongly detected chromodomain helicase DNA-binding protein (CHD)4, CHD3, metastasis-associated 1 family member (MTA)2, MTA1, GATAD2A (p66α) and GATAD2B (p66β), confirming its association with the NuRD complex. IKAROS BioID analysis also detected interactions with MLL2 (*KMT2B*), DOT1L and MLL1 (*KMT2A*), suggesting proximity between IKAROS and MLL1-containing protein complexes. IKAROS BioID enriched for proteins associated with active enhancers (P300, CREBBP, MLL3 (*KMT2C*), MLL4 (*KMT2D*), NCOA6 and UTX (*KDM6A*)) and myeloid TFs (HOXA10, CEBPA, RUNX1, RUNX2, ETV6 and PBX2). Complementary to these findings, HOXA10 and MEIS1 BioID both enriched for IKAROS and components of the NuRD complex. Protein abundances were also determined using label-free quantitation (LFQ) and expressed relative to the control construct ZNF692 (Fig. 6e, Extended Data Fig. 8d and Supplementary Table 8), with findings consistent with the PSM analysis. Striking overlap among enriched proteins by the IKAROS, MEIS1 and HOXA10 BioID systems was observed (Fig. 6f and Extended Data Fig. 8f,g), which included numerous TFs (IKAROS, MEF2A, MEF2C, MEF2D, ETV6, RUNX1–RUNX3, TLE1, TLE3, ZEB2, GFI1, FLI1, MYB and HOXA10). The BioID data confirm, at the level of protein–protein proximity, that IKAROS is physically intertwined within the core transcriptional circuitry of *MLL*-r

Fig. 6 | Chromatin co-occupancy and proximal protein–protein interactions of IKAROS and the MLL fusion network. a, Circos plots displaying co-occupancy between IKAROS, MEIS1, MENIN and MLL1 determined by ChIP–seq at all TSSs and active enhancers bound by at least one factor genome wide. **b**, Tornado plots depicting chromatin occupancy as determined by ChIP–seq from the MOLM-13 cell line at the indicated regulatory regions of interest: IKAROS-bound enhancers and MENIN-bound TSSs. **c**, Integrative Genomics Viewer (IGV) tracks depicting binding of IKAROS, MENIN, MLL1 and MEIS1 at the *BCL2* gene. The promoter and a selected intragenic enhancer are indicated (genomic location is indicated in hg19). The predicted enhancer–promoter connection is indicated (red line). chr, chromosome. **d**, Dot plots displaying PSM rank values from spectral counting on proteins identified in IKAROS, MEIS1 and HOXA10 BioID in MV4;11 versus MOLM-13 cell lines by LC–MS/MS. Notable proteins ranked in the top 50 are circled and labeled on the left of each plot in order of lowest to highest rank (*n* = 2). **e**, Dot plots displaying the log₂ abundance ratios of IKAROS/ZNF692, MEIS1/ZNF692 and HOXA10/ZNF692 BioID in MV4;11 versus MOLM-13 cell lines derived from LFQ analysis of LC–MS/MS data (*n* = 2). **f**, Venn diagram displaying the number of proteins identified in LFQ analysis of the MV4;11 IKAROS, MEIS1 and HOXA10 BioID LC–MS/MS data. All proteins included in the Venn diagram have a more than twofold enrichment over the ZNF692 control. **g**, Direct protein co-IP using IKAROS as the bait and probing for MLL1, MENIN, MEIS1 and MTA2 and lamin B1 for a negative control in the MV4;11 cell line. IP, immunoprecipitation. **h**, Direct protein co-IP using MLL1 and MENIN as the bait and probing for MENIN, MLL1 and IKAROS in the MV4;11 cell line.

leukemia. MENIN was poorly detected by LC–MS/MS; therefore, we further explored the possibility that IKAROS may be a constituent of an isolatable MENIN-containing chromatin complex using co-immunoprecipitation (co-IP). Co-IP using antibodies specific to (1) MENIN or MLL1 and (2) IKAROS resulted in enrichment of

IKAROS and MENIN, respectively (Fig. 6g,h and Extended Data Fig. 9b–e), suggesting the presence of shared protein complex(es); by contrast, co-IP using IKAROS as bait did not enrich for MEIS1 and HOXA9 under these experimental conditions. Finally, we found that inhibition of MENIN–MLL1 protein–protein interaction

by VTP-50469 disrupted MENIN–IKAROS co-IP (Extended Data Fig. 9f). We propose that dual targeting of this putative protein complex containing MENIN and IKAROS contributes to the observed drug synergy.

Combined therapeutic effect of VTP-50469 and LEN in vivo. LEN monotherapy and the VTP-50469 combination were then evaluated for in vivo efficacy. We evaluated LEN because it is supported by clinical experience, a good safety profile and multiple Food and Drug Administration approvals[48], providing opportunity for rapid clinical translation. LEN exhibits high oral bioavailability and has been used in mouse models[49]; by contrast, CC220, although a more potent IKAROS degrader, exhibits poor oral bioavailability and has more limited use in vivo. We used three *MLL*-r and one *NPM1*c AML patient-derived xenograft (PDX) models (Fig. 7a). Human PDX cells were transplanted into non-conditioned immunodeficient recipient mice, and, following engraftment, treatment was commenced with vehicle control, LEN (50 mg per kg daily *per os* (PO)), continuous VTP-50469 treatment in a rodent special diet or the drug combination. Combination treatment led to more rapid clearance of leukemia cells from peripheral blood than that with VTP-50469 alone ($P = 0.024$) (Fig. 7b) and induced strong myelomonocytic differentiation (Extended Data Fig. 10b). After 7–21 d of treatment and according to the VTP-50469 sensitivity of each PDX model, mice were killed for analysis. LEN monotherapy reduced bone marrow disease burden (Fig. 7c), demonstrating in vivo efficacy for IMiD monotherapy in *MLL*-r AML. Furthermore, mice receiving combination treatment displayed a further reduction in bone marrow infiltration compared to mice on either monotherapy (Fig. 7c and Extended Data Fig. 10a) with morphologic evidence of differentiation. LEN- and combination-treated mice exhibited evidence of apoptosis induction in accordance with improved clearance of leukemia (Extended Data Fig. 10c,d). We used RNA-seq to evaluate gene expression changes for each drug in vivo. This confirmed a strong in vivo effect of LEN in altering transcription (Fig. 7d and Supplementary Table 3). LEN elicited expression of differentiation-associated genes (Fig. 7d) and enhanced the VTP-50469 effect when used in combination (Extended Data Fig. 10e,f). An enhanced effect on the HOXA9 transcriptional program was observed in vivo (Extended Data Fig. 10g), and LEN treatment resulted in downregulation of MLL fusion target genes (Extended Data Fig. 10h). Ingenuity upstream regulator analysis using Ingenuity Pathway Analysis showed upregulation of pathways associated with myeloid differentiation, immune activation and inflammation (Lipopolysaccharide, *TNF*, *IL1B*, *INFG*) and tumor-suppressor pathways (*TP53*) (Extended Data Fig. 10i). Finally, we evaluated whether LEN monotherapy and the VTP-50469 combination improves survival. LEN monotherapy at 50 mg per kg once daily resulted in a modest survival advantage (Fig. 7e–h), which could be improved by increasing the dose to 50 mg per kg twice daily (Fig. 7f); combination treatment extended survival of the mice compared to VTP-50469 monotherapy in all three *MLL*-r models. In the *NPM1*c PDX, survival was extended by LEN monotherapy, indicating efficacy for the IMiDs in this distinct AML subtype, but the drug combination did not significantly extend survival compared to VTP-50469 monotherapy, although it resulted in more rapid clearance of leukemia cells from the peripheral blood (Extended Data Fig. 10j). These studies demonstrate in vivo efficacy using a series of human PDX AML models, supporting this approach as a new treatment strategy for patients with *MLL*-r AML.

Discussion

Genome-scale functional genetic screening in *MLL*-r AML identified mechanisms of drug resistance to clinically relevant DOT1L (EPZ-5676) and MENIN (VTP-50469) inhibitors and guided the design of a highly effective combination drug treatment using IMiDs. EPZ-5676 and VTP-50469 therapeutically target *MLL*-r-driven transcriptional dependencies. We identified pathways toward drug resistance involving transcriptional regulators and chromatin-remodeling complexes (for example, NuRD and SWI–SNF), suggesting that cells can undergo transcriptional alterations to escape the effect of these drugs. Complementary to this finding, we found that concomitant targeting of transcriptional regulators that support leukemogenic transcription, such as IKAROS (*IKZF1*), enhance the therapeutic effect of these drugs.
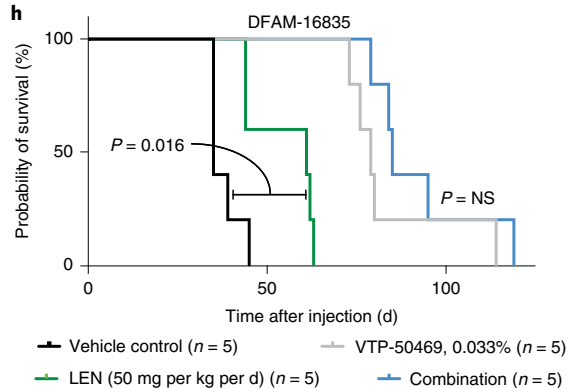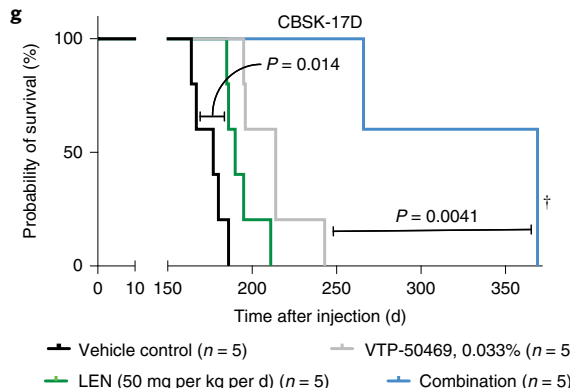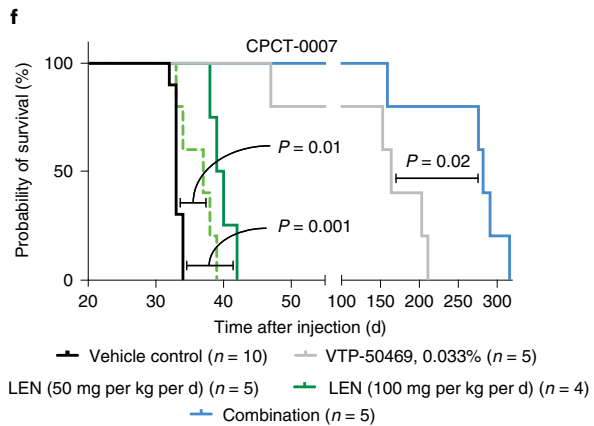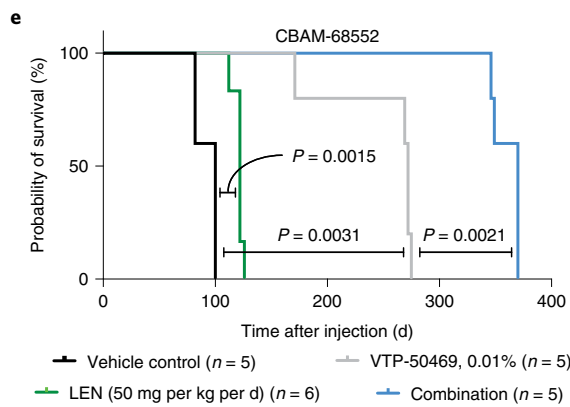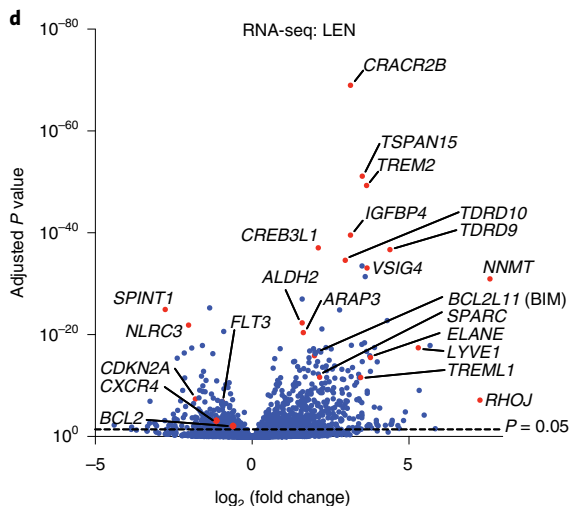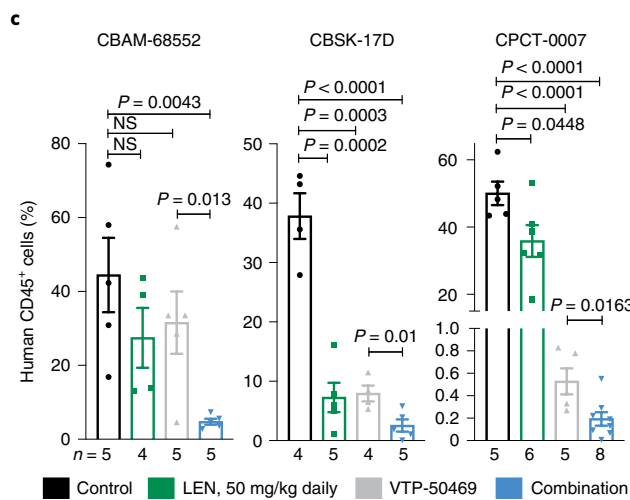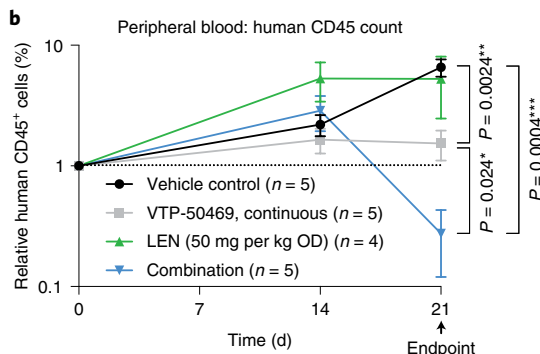
We found a diverse role for IKAROS in supporting leukemia-promoting gene expression, including HOXA–MEIS1-driven gene expression, and repressing pathways for tumor suppression, immune signaling and differentiation. IKAROS function during hematopoiesis has been extensively studied in the lymphoid lineage due to its role as a tumor suppressor in acute lymphoblastic leukemia and a therapeutic target in multiple myeloma; however, less is known about its role in myeloid neoplasia. The *IKZF1* gene is expressed and tightly regulated throughout myeloid maturation, and loss of *IKZF1* or IKAROS during normal hematopoiesis impairs myeloid maturation[50]. Patients with germline dominant negative *IKZF1* gene mutations exhibit multi-lineage hematopoietic defects including abnormal myeloid maturation[51]. Furthermore, IKAROS is a critical regulator of hematopoietic stem and progenitor cell function, implying a potential role in AML stem cell function[52]. Loss of IKAROS in a cell line model of deletion 5q myelodysplastic syndrome results in megakaryocytic differentiation[53], reflecting features that we observed in *MLL*-r AML. In *MLL*-r AML, we found that IKAROS regulates diverse, essential transcriptional processes while displaying extensive chromatin co-occupancy with key regulators of the *MLL*-r transcriptional program: MLL1, MENIN and MEIS1.

Fig. 7 | Combination therapy with VTP-50469 and LEN results in synergistic anti-leukemic activity in vivo. a, Four PDX models were used; PDX identification numbers (ID), whether the MLL fusion was present and additional molecular features are indicated. n.d., not detected; ITD, internal tandem duplication; TKD, tyrosine kinase domain mutation. **b**, Peripheral blood circulating human leukemia cells were indicated by human CD45-positive cells using flow cytometry during treatment with vehicle, LEN at 50 mg per kg daily, VTP-50469 continuously and the drug combination in CBAM-68552. Data represent mean ± s.e.m. with pairwise *P* values calculated using two-tailed *t*-tests. **c**, Analysis of bone marrow from transplanted mice following 3 weeks (CBAM-68552), 2 weeks (CBSK-17D) or 1 week (CPCT-0007) of drug treatment for leukemia burden (human CD45$^+$ cells) as assessed by flow cytometry. Data represent mean ± s.e.m. with *P* values calculated using two-tailed *t*-tests ($n = 4–5$ mice in each group). NS, not significant. **d**, Volcano plot depicting RNA-seq results from human leukemia cells isolated from CBAM-68552 mouse bone marrow following in vivo treatment with LEN ($n = 4$) versus vehicle control ($n = 5$). Selected genes are indicated. **e**, Kaplan–Meier survival curves for CBAM-68552 following 4 weeks of treatment with vehicle, LEN at 50 mg per kg per d or VTP-50469 (0.1% continuously); *P* values were determined by log-rank (Mantel–Cox) tests. **f**, Kaplan–Meier survival curves for CPCT-0007 following 2 weeks of treatment with vehicle, LEN at 50 mg per kg d, LEN at 100 mg per kg per d, VTP-50469 (0.033% continuously) or the combination of LEN at 50 mg per kg per d with VTP-50469 at 0.033%; *P* values were determined by log-rank (Mantel–Cox) tests. **g**, Kaplan–Meier survival curves for CBSK-17D following 2 weeks of treatment with vehicle, LEN at 50 mg per kg per d or VTP-50469 (0.033% continuously); *P* values were determined by log-rank (Mantel–Cox) tests. †Three combination-treated mice were killed after 350 d without evidence for leukemia by flow cytometry of bone marrow. **h**, Kaplan–Meier survival curves for DFAM-16835 following 2 weeks of treatment with vehicle, LEN at 50 mg per kg per d or VTP-50469 (0.033% continuously); *P* values were determined by log-rank (Mantel–Cox) tests.

This is in keeping with known functions of IKAROS: IKAROS can mediate transcriptional repression and activation via recruitment of the NuRD complex[54], it can support active transcription through recruitment of the SWI–SNF complex[54] and the SEC[55], and can also act as a pioneer TF with enhancer-remodeling activity[56]. Thus, we identify IKAROS is a central component of a TF-driven circuitry in

a PDX AML models

PDX ID	Fusion	Molecular
CBAM-68552	*MLL-AF6*	n.d.
CPCT-0007	*MLL-PICALM*	NRAS^{Q61L}
CBSK-17D	*MLL-AF9*	ECT2L^{R852Q}, PTPN11^{G503A}, NRAS^{G12S}
DFAM-16835	None	*NPM1c*, gain MYC, FLT3 ITD, FLT3 TKD

b Peripheral blood: human CD45 count

c

d RNA-seq: LEN

e CBAM-68552

f CPCT-0007

g CBSK-17D

h DFAM-16835

MLL-r AML and likely other AML subtypes that are dependent on HOX–MEIS1-driven gene expression such as *NPM1*c AML.

IKAROS displays extensive chromatin co-occupancy with MENIN, MLL1 and MEIS1, with a pattern of overlap suggesting a role for co-occupancy of IKAROS and MEIS1 at enhancers and a distinct co-occupancy involving MENIN, MLL1 and IKAROS proximal to the TSS. Of particular note, proximity labeling experiments using BioID revealed that IKAROS, MEIS1 and HOXA10 share a similar proximal protein environment populated by important transcriptional regulatory protein complexes such as NuRD and MLL3 and MLL4 COMPASS as well as TFs well known for their role in hematopoietic development and leukemia. This nominates IKAROS as a critical regulator of myeloid leukemia-associated gene expression. Furthermore, these data define the proximal protein network that comprises the HOXA10–MEIS1 regulatory complex, which is central to hematopoietic development and multiple AML subtypes. Notably, MEIS1–HOXA9 has been reported to play a key role in enhancer regulation[18], and MENIN is thought to primarily act proximal to the TSS[57], whereas IKAROS has diverse described functions at both the TSS and the enhancer[54], supporting a role for IKAROS at both of these locations in *MLL*-r AML. Importantly, chromatin co-occupancy at the TSS by IKAROS and MENIN raises the possibility that IKAROS may participate in the MLL fusion protein complex. In support of this possibility, IKAROS and other components of the NuRD complex have been previously reported to co-immunoprecipitate with seven different MLL fusion proteins[58]. Interestingly, as a sequence-specific DNA-binding protein, IKAROS could potentially play a role in directing the genomic localization of the MLL fusion protein and other components of its transcriptional network. It is also important to note that, outside of its well-defined protein–protein interaction with MLL1 (*KMT2A*)[59] and the MLL1 fusion protein[5], MENIN is reported to interact with a number of TFs including c-MYC[60] and JUND[61,62], which may be akin to our observations for IKAROS. We also found post-translational loss of IKAROS protein following treatment with the MENIN inhibitor, similar to what has been described for MENIN[24,63] and partially attributed to its eviction from stabilizing chromatin-bound complexes; we hypothesize that IKAROS may be similarly stabilized within such chromatin-bound complexes involving MENIN–MLL1 that then become destabilized following MENIN-inhibitor treatment. Indeed, we find that IKAROS exhibits a physical interaction with both MENIN and MLL1 (albeit this may be direct or through interaction with a larger multiprotein complex) using a series of targeted co-IPs.

From the perspective of clinical translation, these findings support a new therapeutic approach for the treatment of *MLL*-r AML, using drugs that target IKAROS for degradation in combination with small-molecule inhibitors of MENIN and DOT1L. IMiDs have already been evaluated in numerous clinical trials for AML[64] with encouraging but variable evidence for efficacy; however, these trials have not evaluated specific leukemia subtypes. The rationale for using these drugs in the setting of AML has been attributed to targeting CK1α[65], immune modulation[66] and activation of calpain-dependent[67] apoptosis. In addition to these important features of the mode of action of IMiDs, we present data that therapeutic targeting of IKAROS is a critical determinant of the drug's efficacy in AML, supporting the optimization of IMiD-induced IKAROS degradation as a goal for improved AML therapeutics. Having defined overlapping functions of MENIN and IKAROS in *MLL*-r AML, we show that combined therapeutic targeting of these two AML dependencies leads to profound anti-leukemic effects both in vitro and in vivo, supporting this as a new therapeutic approach and highlighting an essential functional interaction between MENIN and IKAROS in leukemic transcriptional regulation. This serves as an example of dual therapeutic targeting of a robust transcriptional network and a putative chromatin-bound

protein complex that more effectively shuts down its oncogenic function than either drug alone. Furthermore, combining MENIN inhibition and IKAROS degradation converts two small molecules that primarily induce AML differentiation into a combination that potently induces apoptosis, an effect that is predicted to provide therapeutic benefit.

Methods

Animals and patient-derived cells. Animal experiments were approved by Dana-Farber Cancer Institute's (DFCI) Institutional Animal Care and Use Committee (DFCI protocol number 16-021; principal investigator, S. Armstrong). PDX models were provided by the Center for Pediatric Cancer Therapeutics (CPCT) at the DFCI. CPCT-0007 is a newly generated model: primary human leukemic cells obtained from the Pediatric LEAP Consortium were injected intravenously into sublethally irradiated (200 Gy, 4 h before injection) 6–8-week-old NSG-S mice (genotype, NOD.Cg-*Prkdc*^scid *Il2rg*^tm1Wjl Tg(CMV-IL3,CSF2,KITLG)1Eav/MloySzJ) (Jackson Laboratory, 013062). When animals developed signs of leukemia, bone marrow and spleen were collected, and cells were frozen for banking purposes. After secondary transplantation, samples were analyzed using a targeted next-generation sequencing panel (Rapid Heme Panel, Brigham and Women's Hospital)[68]. The source patient (0.75-year-old male) had refractory *MLL*-r AML. CBAM-68552 (refs. [24,69]) and DFAM-16835 were previously described[29], and CBSK-17D was a kind gift from R. Levine, Memorial Sloan Kettering Cancer Center. Laboratory mice were housed in solid-bottom, polysulfone micro-isolator cages (75 square inches). The cages were used in conjunction with the Optimice rack systems with integrated automatic watering. Temperature and humidity in the rodent facilities were controlled at 72 ± 2 °F and a target range of 35–55% relative humidity. A standard photoperiod of 12 h of light and 12 h of dark was controlled by an automated system.

Cell lines. Cell lines were acquired from the American Type Culture Collection (ATCC) or the Deutsche Sammlung von Mikroorganismen und Zellkulturen (DSMZ) as indicated: HEK293T (ATCC, CRL-3216), MOLM-13 (DSMZ, ACC554), MV4;11 (ATCC, CRL-9591), OCI-AML2 (DSMZ, ACC-99), THP-1 (ATCC, TIB-202), OCI-AML3 (DSMZ, ACC-582), U937 (ATCC, CRL-1593.2) and HL60 (ATCC, CCL-240) cells. The IMS-M2 cell line (*NPM1*c) was a kind gift from D. Tenen, Harvard Medical School, with the original source as previously described[70]. Identification of cell lines was independently confirmed by cytogenetic profiling. Routine mycoplasma testing results were negative. Cells were cultured in RPMI 1640 (Gibco, 11875-093) supplemented with 10% FBS, 100 U ml⁻¹ penicillin (Gibco), 100 μg ml⁻¹ streptomycin (Gibco) and ʟ-glutamine (2 mM) at 37 °C with 5% CO_2.

Genome-scale functional genetic screen. Functional genetic screening was carried out as previously described[71] using paired whole-genome libraries (denoted as H1 and H2) (Addgene, 1000000132). Each library contains approximately 90,000 sgRNA species with five sgRNA species per gene and a panel of *AAVS1* negative control sgRNA species. The H1 and H2 libraries combined target over 18,000 genes with a total of 185,634 sgRNA species. The sgRNA vector combines both Cas9 and sgRNA expression along with a puromycin resistance cassette in a single construct. The H1 and H2 libraries were prepared by electroporation (10 μF, 600 Ω, 1,800 V) E. cloni high-efficiency bacteria (Lucigen) and culturing on agar plates overnight before DNA purification using Maxiprep DNA-purification columns (Invitrogen, K210017). Prepared libraries were sequenced before performing the screen, showing Gini index <0.1, zero sgRNA count <0.5% and sgRNA representation of the parental library >99.5%. Virus production was carried out in 10-cm plates using HEK293T cells with 10 μg library plasmid per 10-cm plate along with packaging plasmids psPAX2 (Addgene, 12260, 7.5 μg) and pMD2.G (Addgene, 12259, 3 μg). X-tremeGENE 9 DNA transfection reagent (Sigma-Aldrich) was used to deliver DNA into HEK293T cells in Opti-MEM medium (Gibco, 31985062). Viral supernatant was collected at 24 and 48 h and pooled. Viral supernatant was titrated to produce an MOI of approximately 0.2. For each experimental replicate, 50 × 10⁶ cells were infected at an MOI of 0.2, resulting in ~10 × 10⁶ transduced cells, providing for 100× coverage of the sgRNA library. Infections were carried out as a 2-h co-incubation with viral supernatant followed by 2 h of centrifugation at 800*g* and 37 °C. After recovery from infection (48 h), cells were placed in puromycin (1 μg ml⁻¹) for 72 h to enrich for sgRNA-transduced cells. Cells were then collected and placed in fresh medium to recover for a further 48 h before commencing the screen. A library coverage of 300× (30 × 10⁶ cells) was maintained throughout the experiment. Cell pellets were obtained at day 0 and day 14, containing 30 × 10⁶ cells. Cells were washed with PBS and lysed in 8 ml lysis buffer (NaCl, 300 mM; SDS, 0.2%; EDTA, 1 mM; Tris-HCl, pH 8.0, 10 mM). Samples were then incubated with RNase A (100 μg ml⁻¹) for 1 h at 65 °C and then incubated overnight with proteinase K (100 μg ml⁻¹) at 55 °C with constant rotation. Genomic DNA was then purified by phenol–chloroform extraction. Amplicon sequencing libraries were then produced using 200 μg genomic DNA from each experimental replicate as follows: a first-round PCR reaction was carried out in 32 separate 100-μl reactions, using Q5 High-Fidelity DNA Polymerase (NEB) to amplify the region of the

sgRNA corresponding to that between U6 and EF-1α using primers (forward, AATGGACTATCATATGCTTACCGTAACTTGAAAGTATTTCG and reverse, TCTACTATTCTTTCCCCTGCACTGTACCTGTGGGCGATGTGCGCTCTG); the product was pooled from the primary PCR reaction. A second PCR was carried out to incorporate Illumina adaptors and a 6-bp barcode for identification of samples (Supplementary Table 5). A third PCR reaction was carried out to enrich for the full-length amplicon using primers (forward, AATGATACGGCGACCACCGAGATC and reverse, CAAGCAGAAGACGGCATACGAGAT). Final amplicon libraries were purified by gel electrophoresis, and extraction of the library followed by gel purification using the QIAquick Gel Extraction kit (Qiagen, 28704) was performed. Sequencing was carried out by Novogene, and results were analyzed using the MAGeCK and MAGeCKFlute computational pipeline[32,72]. FASTQ files were converted to read-count tables using the MAGeCK 'count' command. Each genetic screen was carried out in $n=2$ replicates for each of the H1 and H2 libraries (total $n=4$ for each drug and control condition). H1 and H2 libraries were combined into a single analysis using the MAGeCK maximum likelihood estimation (MLE) function using read-normalized count tables and *AAVS1* normalization. MLE calculations were then analyzed using the MAGeCKFlute package in RStudio to apply corrections for cell cycle bias and categorize genetic hits as pathway (group 1), resistance (group 2) or synthetic lethal (group 4). For the combined EPZ-5676–VTP-50469 analysis, each set of screens was treated as an experimental replicate and analyzed using the MAGeCK MLE function followed by MAGeCKFlute.

Drug-treatment studies: in vivo. For PDX experiments, 1×10^6 human cells were injected into the tail vein of non-irradiated NOG-F mice (NOD.Cg-*Prkdc^scid Il2rg^{tm1Sug}*/JicTac) (Taconic BioSciences). For the cell line xenograft experiment, MOLM-13 Cas9-expressing cell lines with sgRNA against the luciferase gene (non-targeting) and two sgRNA species against *IKZF1* were used. All transplanted mice were female, aged between 8 and 10 weeks on delivery to the facility and received injections 1–2 weeks thereafter. Drug treatment began after engraftment was confirmed by flow cytometric detection of human CD45-expressing cells in the peripheral blood. VTP-50469-containing chow (0.1% and 0.03% as indicated) was provided by Syndax Pharmaceuticals. LEN (MedChemExpress) was reconstituted in 0.5% carboxymethylcellulose (Sigma, C4888) and 0.25% Tween-80 (Sigma, P1754) in water and sonicated until a homogeneous suspension was formed immediately before dosing by oral gavage. Peripheral blood leukemia burden was monitored by blood sampling. Red blood cells in blood samples were lysed using Pharm Lyse (BD, 555899) before staining with PE-conjugated anti-human CD45 (BioLegend, 304058, 5 μl antibody per 100 μl solution), BV421-conjugated anti-CD11b (BioLegend, 5 μl antibody per 100 μl solution) or APC-conjugated anti-CD14 (BioLegend, 5 μl antibody per 100 μl solution) antibodies as indicated. Samples were then analyzed on an LSR Fortessa flow cytometer (Becton Dickinson). For survival experiments, mice were killed when showing signs of illness. We adhered to the DFCI standard operating procedure for humane experimental endpoints, which includes tumors measuring 2 cm, ulceration or infection of the tumor site, tumors that compromise mobility, tumors that have become necrotic, weight loss exceeding 15% of the animal's body weight, interference with the animal's ability to eat, drink, urinate or defecate, and anorexia. Leukemia burden was assessed by measuring human CD45-positive cells by flow cytometry or by immunohistochemistry (Servicebio).

Drug treatment studies: in vitro. All drugs were diluted from stock solutions into full tissue culture medium (RPMI, 10% FBS). Bortezomib (Thermo Fisher) was reconstituted in DMSO to make a 10 mM stock solution and used at a final working concentration of 50 nM. A 10 mM stock solution of QVD-OPh (Abcam) was diluted to a final working concentration of 10 μM. All IMiD drugs were obtained from MedChemExpress: THAL (MedChemExpress, HY-14658), POM (MedChemExpress, HY-10984), LEN (MedChemExpress, HY-A0003) and CC220 (MedChemExpress, HY-101291) were made into single-use aliquots at 10 mM in DMSO, stored at −80 °C and diluted. An equivalent proportion of DMSO was added to all control samples.

Cell viability, differentiation, apoptosis, cell cycle and morphology analysis. For cell-proliferation assays, MOLM-13, MV4;11, OCI-AML-2 and IMS-M2 cells were plated in 96-well plates. IMiD drug dilutions were made on a half-log scale and plated in triplicate. Cells were split 1:10 on days 3, 6, 9, 12 and 15 into fresh drug-containing medium. Viable cells were measured using an LSR Fortessa (Becton Dickinson) every 3 d with DAPI used as a viability stain. Cell counts were normalized to counts of the DMSO control. Apoptosis was measured using the Annexin V Apoptosis Detection kit (eBioScience, 88-8007074). For cell cycle analysis, cells were collected after the indicated drug treatment, washed with PBS and fixed using the Cytofix/Cytoperm kit (BD Biosciences, 554714) before DAPI staining and analysis by flow cytometry. For assessment of differentiation, after indicated drug treatment or CRISPR–Cas9 modification, cells were stained with BV421-conjugated anti-CD11b (BioLegend, 301324) and APC-conjugated anti-CD14 (BioLegend, 367118), each with 5 μl antibody per 100 μl solution. Samples were then analyzed on an LSR Fortessa flow cytometer. For morphology assessment, cells were collected after CRISPR modification, centrifuged onto

slides using a cytocentrifuge (Thermo Scientific) and stained for microscopy using the JorVet Dip Quick Stain (Jorgensen Laboratories, JO322). FLT3 cell surface expression was assessed by flow cytometry using the anti-CD135/FLT3/Flk-2 antibody (BioLegend, 313306) with 5 μl antibody per 100 μl solution.

Lentivirus production and CRISPR–Cas9-mediated cell modification. Sequences for selected sgRNA species targeting human *IKZF1* and *MTA2* were extracted from the H1 and H2 sgRNA libraries, and additional sgRNA species were designed using the Broad Genetic Perturbation Platform web tool[73]. Sequences used are listed in Supplementary Table 5. Oligonucleotides for sgRNA species were synthesized by Integrated DNA Technologies and cloned into the lentiviral vector, improved-scaffold-pU6-sgRNA-EF1alpha_PURO-T2A-RFP (ipUSEPR) (gift from Y. Soto-Feliciano and D. Allis, Rockefeller University). Constitutive Cas9 expression was achieved using pLentiCas9-Blast (Addgene, 52962). Lentivirus was produced in HEK293T cells following transient cotransfection with ipUSEPR or pLentiCas9 (10 μg), pMD2.G (3 μg) and psPAX2 (5 μg) in 10-cm tissue culture plates. Viral supernatant was collected at 24 and 48 h after transfection and passed through a 0.45-μm filter. Viral supernatant produced for pLentiCas9-Blast was concentrated approximately 30-fold by ultracentrifugation in an SW-28 rotor at 112,700g for 90 min. Viral supernatant for ipUSEPR was used neat. All human AML cell lines were transduced by co-incubation of 10^5 cells with viral supernatant supplemented with polybrene at 0.8 μg ml⁻¹ followed by centrifugation at 800g and 37 °C for 2 h. Cells infected with pLentiCas9-Blast were selected with blasticidin (10 μg ml⁻¹) for 6 d. For competition assays, Cas9-expressing human AML cell lines were infected with the respective sgRNA construct and were not sorted (yielding a mixed population of RFP⁺ and RFP⁻ cells), and RFP expression was measured over time by flow cytometry. For assessment of proliferation, apoptosis and morphology, sgRNA-transduced cell populations were sorted using a FACSMelody Cell Sorter (BD) to produce a uniform population of high-RFP-expressing cells before commencing the assay; experiments were performed on bulk cell populations. For all experiments, a control non-targeting sgRNA construct was used for comparison (Supplementary Table 5).

Western blot analysis and protein immunoprecipitation. For western blots, cells were collected and washed once with PBS, and the protein was collected by lysis in 1× Laemmli buffer containing 10 mM dithiothreitol (DTT), sonicated and denatured for 5 min at 95 °C. For MLL1 (*KMT2A*), samples were loaded onto a 3–8% Tris–acetate polyacrylamide gel (Thermo Fisher) and separated by electrophoresis in 1× Tris–acetate running buffer (Novex, LA0041). Protein was then transferred to PVDF membranes using wet transfer in 1× Transfer Buffer (Novex, NP0006-1) containing 10% methanol for 2 h at 32 V and 4 °C. Western blotting for all other proteins was carried out using 10% Bis-Tris polyacrylamide gels and then transferred onto nitrocellulose membranes using the iBlot 2 Gel Transfer Device (Thermo Fisher). The membranes were blocked in 5% milk in TBS–Tween buffer (TBST) for 1 h and incubated overnight; as indicated, rabbit anti-IKAROS (Cell Signaling, 14859S, 1:1,000 dilution), mouse anti-IKAROS (Invitrogen, MA5-28613, 1:2,000 dilution), anti-KMT2A/MLL1 (Bethyl, A300-086A, 1:5,000 dilution), anti-MENIN (Bethyl, A300-105A, 1:5,000 dilution), anti-HOXA9 (Abcam, ab140631, 1:5,000 dilution), anti-MEIS1 (Abcam, 19867, 1:1,000 dilution), anti-MTA2 (Abcam, ab8106, 1:1,000 dilution), anti-c-MYC (Abcam, ab32072, 1:1,000 dilution), anti-BCL2 (Cell Signaling, 15071, 1:1,000 dilution), anti-BCL-XL (Cell Signaling, 2764S, 1:1,000 dilution), anti-MCL1 (Cell Signaling, 94296S, 1:1,000 dilution), anti-CK1α (Abcam, ab108296, 1:1,000 dilution), anti-histone H3 (Abcam, ab1791, 1:2,500 dilution), anti-β-actin (Cell Signaling, 12620S, 1:1,000 dilution), anti-lamin B1 (Abcam, ab16048, 1:1,000 dilution) or anti-GAPDH (Cell Signaling, 97166S, 1:1,000 dilution) antibodies were used to immunostain the membrane. Membranes were washed with TBST more than six times and developed using a secondary HRP-linked anti-rabbit IgG (Thermo Fisher, 45000682, 1:10,000) or secondary HRP-linked anti-mouse IgG (Cell Signaling, 7076S, 1:2,000) antibody and a chemiluminescence kit (Pierce). The Precision Plus Dual Color protein standard (Bio-Rad) was used to determine molecular weight. Blots were imaged using the ChemiDoc MP Imaging System (Bio-Rad). Protein co-IP was carried out using 20 million cells per co-IP assay according to two different approaches: (1) high salt nuclear extraction with an NP-40 wash[74] (with modification): cells were washed with PBS and then washed with hypotonic buffer (10 mM Tris, pH 7.5, 10 mM KCl, 1.5 mM MgCl₂) and then incubated for 10 min on ice in hypotonic buffer before dounce homogenization and centrifugation at 2,600g for 10 min. Samples were then resuspended in low salt buffer (20 mM Tris, pH 7.5, 12.5% glycerol, 1.5 mM MgCl₂, 0.2 mM EDTA, pH 8.0), and then an equal volume of high salt buffer (20 mM Tris, pH 7.5, 12.5% glycerol, 1.5 mM MgCl₂, 0.2 mM EDTA, pH 8.0, 1.2 M KCl) was added dropwise during continuous mixing, and then samples were agitated at 4 °C for 25 min before centrifugation at 17,000g for 25 min. The supernatant containing extracted protein was then diluted fourfold in low salt buffer before proceeding with immunoprecipitation. The resulting protein extract was then incubated with antibody-bound beads at 4 °C (as described below). After overnight incubation, protein-bound beads were then washed three times with wash buffer (20 mM Tris, pH 7.5, 150 mM NaCl, 0.25% NP-40, 0.2 mM phenylmethylsulfonyl fluoride (PMSF)). (2) High glycerol wash[75]: cells were collected and washed with PBS and

then incubated in nuclear lysis buffer (50 mM KCl, 10 mM MgSO₄•7H₂O, 5 mM HEPES, 0.05% NP-40, 1 mM PMSF, 3 mM DTT, supplemented with cOmplete protease inhibitor), followed by washing nuclei with nuclei wash buffer (NaCl, 300 mM; Tris, pH 7.5, 50 mM; MgCl₂, 1 mM) and subsequent disruption using dounce homogenization in buffer EB300 (Tris, pH 7.5, 50 mM; EDTA, 1 mM; NP-40, 1%; NaCl, 300 mM) and centrifugation at 17,000g for 15 min. The resulting nuclear extract was supplemented with 250 U benzonase (Sigma) and then incubated with antibody-bound beads overnight at 4 °C. Protein-bound beads were washed with buffer BC200 (20 mM Tris (pH 7.9), 0.2 mM EDTA, 1 mM DTT, 0.2 mM PMSF, 20% glycerol and 200 mM KCl) three times. In both protocols, protein was eluted from beads by incubating in 1× Laemmli buffer at 95 °C for 10 min before western blot analysis. Immunoprecipitation of each protein of interest was carried out using 5 µg antibody with Protein A Dynabeads (for the rabbit antibody) or Protein G Dynabeads (for the mouse antibody). Beads were washed three times (0.5% BSA, 0.05% Triton X-100 in PBS) and incubated with antibody overnight with constant turning; 5 µg of antibody was used for each immunoprecipitation. Beads were washed again three times before adding the protein preparation. Antibodies used were anti-MENIN antibody (Bethyl), anti-IKAROS antibody (Invitrogen, mouse antibody), anti-KMT2A/MLL1 antibody (Bethyl), normal rabbit IgG control (Bethyl) or normal mouse IgG control (Cell Signaling). All buffers were supplemented with 1× cOmplete protease-inhibitor tablets (Roche, 11836145001).

RNA isolation, quantitative real-time PCR and RNA-seq. For all cell line experiments, RNA was isolated from cells following the indicated drug treatments using the RNeasy Mini kit (Qiagen). RNA samples from in vivo experiments were obtained by isolating human cells from mouse marrow using the EasySep mouse–human chimera kit (Stemcell Technologies) followed by RNA extraction using the PicoPure RNA isolation kit (Thermo Fisher). For RT–qPCR, cDNA synthesis was carried out using the AzuraFlex cDNA Synthesis kit (Azura Genomics). The TaqMan gene expression assay for *BCL2* (Thermo Fisher, 4331182) and *MYC* (Thermo Fisher, 4331182) was used for the RT–qPCR reaction on the ViiA 7 Real-Time PCR system (Applied Biosystems). *GAPDH* was used as the housekeeping control. For next-generation RNA-seq, RNA quality was assessed using the Agilent TapeStation 4200 (Agilent Technologies). Library preparation was performed using the NEBNext Ultra II RNA Library Prep kit for Illumina (New England Biolabs). Sequencing was performed on an Illumina NextSeq 550 system (Illumina), acquiring 37-bp, paired-end reads.

Chromatin immunoprecipitation and next-generation sequencing. ChIP–seq was performed in MV4;11 and MOLM-13 cells. Cells were cross-linked in 1% methanol-free formaldehyde (Thermo Fisher) for 7 min at room temperature, followed by formaldehyde quenching using 100 mM Tris, pH 8.0, and 250 mM glycine. Cells were then lysed using 50 mM Tris-HCl, pH 8.0, 100 mM NaCl, 5 mM EDTA and 1% SDS for 10 min at ambient temperature, and chromatin was collected by centrifugation at 15,000g for 10 min. Chromatin was then resuspended in 66 mM Tris-HCl, pH 8.0, 100 mM NaCl, 5 mM EDTA, 1.7% Triton X-100 and 0.5% SDS and sheared using an E100S sonicator (Covaris) to DNA chromatin fragments 200–400 bp in size. Sheared chromatin from the 20 million cells was used in each immunoprecipitation using the respective antibodies: anti-MENIN (Bethyl, A300-105A), anti-KMT2A/MLL1 (Bethyl, A300-086A), anti-MEIS1 (Abcam, ab19867) and anti-IKAROS (Cell Signaling, 14859S) antibodies and protein A magnetic beads (Dynal). Immunoprecipitated DNA fragments were eluted and de-cross-linked in 100 mM NaHCO₃, 100 mM NaCl and 1% SDS and quantified by TapeStation 4200 (Agilent) and Qubit (Thermo Fisher). DNA (1–10 ng) was used to prepare Illumina-compatible libraries using the SMARTer ThruPLEX DNA-seq kit (Takara) followed by sequencing using the NextSeq 550 system (Illumina) to obtain paired-end reads (R1, 37 bp; R2, 37 bp).

CUT&RUN sequencing. The protein A–MNase fusion protein (pA–MNase) was produced by transforming the pK19pA-MN plasmid (Addgene, 86973) into Rosetta (DE3) competent cells (Novagen). Expression of pA–MNase was induced in liquid LB culture at an optical density of 0.7 with IPTG treatment for 2 h. Following cell lysis, pA–MNase was purified using IgG Sepharose 6 Fast Flow beads (GE Healthcare, 17-0969-01), followed by concentration in a 20,000 MWCO Slide-A-Lyzer cassette (Thermo Fisher, 66012). The pA–MNase product was assessed by BCA quantification and western blot analysis. CUT&RUN was performed as previously described[42]. In short, 5 × 10⁵ cells were washed twice with PBS and then once with a wash buffer (20 mM HEPES, pH 8.0, 150 mM NaCl, 0.5 mM spermidine), followed by immobilization on concanavalin A magnetic beads activated in binding buffer (20 mM HEPES, pH 8.0, 10 mM KCl, 1 mM CaCl₂, 1 mM MnCl₂) (PolyScience). The immobilized cells were permeabilized by washing with wash buffer supplemented with 0.1% Triton X-100 and incubated with anti-IKAROS antibody (Cell Signaling, 14859S), rabbit IgG control (Bethyl, P120-201), anti-CTCF antibody (Cell Signaling, 3418S) or anti-H3K27Ac antibody (Diagenode, 15410196) at 4 °C with addition of EDTA to 2 mM. After a 2-h incubation, the cells were washed twice and incubated with the pA–MNase conjugate at 4 °C. After 4 h, the cells were washed twice, and MNase was activated by adding CaCl₂ to 20 mM. DNA digestion was stopped by adding EDTA and

EGTA, both to 10 mM. DNA fragments were collected in the supernatant and purified using 1.8× AMPure XP beads (Beckman Coulter), which were then converted to Illumina-compatible libraries using the NEBNext Ultra II DNA Library Prep kit for Illumina (New England Biolabs), followed by sequencing using the NextSeq 550 system (Illumina). For the drug-treatment experiment, carryover *Escherichia coli* DNA from the pA–MNase preparation was used for sample normalization during bioinformatic analysis.

ATAC sequencing. Five million cells from MV4;11 and MOLM-13 cells were washed with PBS and resuspend in a hypotonic buffer (50 mM KCl, 10 mM MgSO₄, 5 mM HEPES, 0.05% NP-40, 1 mM PMSF, 3 mM DTT) to generate intact nuclei and washed three times with a nuclear wash buffer (10 mM Tris-HCl, pH 7.5, 10 mM NaCl, 3 mM MgCl₂). A total of 50,000 nuclei per cell line were used for the transposition reaction. Nuclei were incubated in 1× TD Buffer (Illumina) and 2.5 µM transposase enzyme (Illumina) for 30 min at 37 °C. Transposed DNA was then extracted from nuclei using the MinElute PCR Purification kit (Qiagen). Transposed DNA fragments were amplified using the NEBNext High-Fidelity PCR kit (NEB) with a universal Nextera primer and a unique indexing primer and sequenced using the NextSeq 550 system (Illumina), obtaining paired-end reads (R1, 75 bp; R2, 75 bp), with 57 million and 48 million reads obtained for the MOLM-13 and MV4;11 cell lines, respectively.

Sample preparation for quantitative mass spectrometry-based global protein measurements. Ten million cells from each cell line (MV4;11, MOLM-13 and OCI-AML2) were treated with DMSO, THAL at 10 µM, LEN at 5 µM, POM at 1 µM or CC220 at 0.1 µM for 5 h, and cells were collected by centrifugation and washed three times with PBS. For combination drug treatment, cells were first treated with DMSO or VTP-50469 at 50 nM for 5 d before IMiD treatment. Lysis buffer (8 M urea, 50 mM NaCl, 50 mM 4-(2-hydroxyethyl)-1-piperazineethanesulfonic acid (EPPS), pH 8.5, protease and phosphatase inhibitors) was added to the cell pellets, and samples were manually homogenized by 20 passes through a 21-gauge (1.25-inch-long) needle. The resulting cell lysate was clarified by centrifugation. The Bradford assay (Bio-Rad) was used to determine protein concentration. Protein (200 µg) from each sample was reduced, alkylated, digested with LysC and trypsin and TMT labeled as previously described[40]. Each of the sample channels was combined in a 1:1 ratio, desalted using C18 solid-phase extraction cartridges (Waters) and analyzed by LC–MS/MS for quality-control analysis and channel ratio comparison. Equally combined samples were then offline fractionated into 96 fractions by high-pH reverse-phase HPLC (Agilent, LC1260) through an Aeris PEPTIDE XB-C18 column (Phenomenex) with mobile phase A containing 5% acetonitrile and 10 mM NH₄HCO₃ in LC–MS grade water and mobile phase B containing 90% acetonitrile and 5 mM NH₄HCO₃ in LC–MS grade water (both at pH 8.0). The resulting fractions were then pooled into 24 fractions, desalted and submitted for MS analysis.

Sample preparation for BioID interaction analysis. To generate BioID systems, coding sequences for IKAROS, MEIS1, HOXA10 and ZNF692 were synthesized and cloned by Twist Bioscience to produce N- and C-terminally BirA*-tagged pTwist-Lenti-SFFV-Puro-WPRE constructs. Stably expressing MV4;11 and MOLM-13 cell lines were then generated, and the near-equal biotin labeling was determined by western blotting with streptavidin–HRP (data not shown) and N-terminally BirA*-tagged IKAROS, C-terminally BirA*-tagged MEIS1, C-terminally BirA*-tagged HOXA10 and C-terminally BirA*-tagged ZNF692. MV4;11 and MOLM-13 cell lines were chosen for subsequent experiments. Cell lines were expanded to large volumes, and 50 µM biotin was added to culture medium 24 h before collection. Cells were collected and washed three times with PBS and then resuspended in a hypotonic buffer (50 mM KCl, 10 mM MgSO₄, 5 mM HEPES, 0.05% NP-40, 1 mM PMSF) followed by three washes with a nuclear wash buffer (10 mM Tris-HCl, pH 7.5, 10 mM NaCl, 3 mM MgCl₂) to generate intact nuclei. Nuclei were lysed in BioID lysis buffer (50 mM Tris, pH 7.5, 500 mM NaCl, 0.4% SDS, 2% Triton X-100 supplemented with Roche protease-inhibitor tablets), followed by probe tip sonication (three rounds; duty cycle, 65%; 30-s pulses). Samples were clarified by centrifugation, and lysates were quantified by the BCA assay. A total of 10 mg protein per replicate with two replicates per cell line was incubated with 80 µl streptavidin Sepharose high-performance beads (MilliporeSigma) overnight at 4 °C. After incubation, beads were washed with 2 ml 2% SDS, 2 ml BioID lysis buffer three times, 10 ml 50 mM Tris six times and 5 ml 50 mM triethylammonium bicarbonate once. Streptavidin-bound proteins then underwent on-bead tryptic digestion by adding 1 µg sequencing-grade trypsin (Promega) and incubating the beads overnight at 37 °C. After digestion, the supernatant was separated from the streptavidin beads and acidified to 1% formic acid. Acidified peptides were then desalted and purified using SOLAµ solid-phase extraction plates (Thermo Fisher Scientific).

Mass spectrometry data collection. All MS data were collected using an Orbitrap Fusion Lumos mass spectrometer (Thermo Fisher Scientific) coupled with a Proxeon EASY-nLC 1200 LC pump (Thermo Fisher Scientific). Peptides were separated on an EASY-Spray ES803a microcapillary column (inner diameter of 75 µm, Thermo Fisher Scientific). For global quantitative proteomics and BioID

interaction proteomics, peptides were separated using a 190 min and 140 min gradient of 6–27% and 5–34% buffer B (95% acetonitrile) in 1.0% formic acid with a flow rate of 300 nl min⁻¹, respectively. For global quantitative proteomics, each analysis used an MS³-based TMT method as described previously[76]. For global quantitative proteomics and BioID interaction proteomics, the data were acquired using a mass range of m/z 340–1,350 and 375–1,500, a resolution of 120,000, an AGC target of 5×10^5, a maximum injection time of 100 and 50 ms and dynamic exclusion of 120 s for the peptide measurements in the Orbitrap, respectively. For global quantitative proteomics and BioID interaction proteomics, data-dependent MS² spectra were acquired in the ion trap with normalized collision energy set to 35%, AGC target set to 1.8×10^4 and 4×10^5 and a maximum injection time of 120 and 50 ms, respectively. MS³ scans were acquired in the Orbitrap with HCD collision energy set to 55%, AGC target set to 2×10^5, a maximum injection time of 150 ms, resolution at 50,000 and with maximum SPS precursors set to 10. For BioID interaction proteomics, data-dependent MS/MS spectra were acquired in the ion trap in centroid mode with the collision energy set to 30%, AGC target set to 1×10^4 and a maximum injection time of 30 ms.

Mass spectrometry data analysis. Proteome Discoverer 2.2 (Thermo Fisher Scientific) was used for .RAW file processing and controlling peptide- and protein-level FDRs, assembling proteins from peptides and protein quantification from peptides. MS/MS spectra were searched against a Swiss-Prot human database (December 2016) with both the forward and reverse sequences. For BioID data searches, a FASTA entry was included for the protein sequence of BirA*. Database search criteria were as previously described[75]. Reporter ion intensities were normalized and scaled using in-house scripts in the R framework[77]. Statistical analysis was carried out using the limma package within the R framework[78]. For BioID data spectral counting analysis, individual Proteome Discoverer searches were conducted on IKAROS, MEIS1 and HOXA10 BioID .RAW files, combining both replicates. The protein identities and their corresponding PSM values were then merged between MV4;11 and MOLM-13 cell lines to create a unified dataset with proteins uniquely detected in MV4;11 or MOLM-13 cells excluded. The protein identities were then referenced against the CRAPome repository[79] to remove contaminants common to affinity purification MS experiments. The dataset was further filtered by removal of proteins that met either of the following two criteria: if the number of 'experiments detected' in the CRAPome repository was greater than the average of the number of 'experiments detected' values across our BioID datasets or if the 'average spectral count' reported in the CRAPome repository was greater than the average of the 'average spectral count' values detected in our BioID datasets. NuRD complex member proteins are highly prevalent in the CRAPome, and, because of the biological relevance of this study, we made a special exemption for removal. After CRAPome proteins were removed, the resulting proteins were ranked by descending number of PSMs and plotted in rank order. For LFQ, analysis was carried out using Proteome Discoverer 2.2. Separate analyses were made for MV4;11 and MOLM-13 cells using corresponding IKAROS, MEIS1, HOXA10 and ZNF692 BioID .RAW files that were searched together, and the Minora Feature Detector was used to generate abundance values for proteins across the different samples. Normalization was applied with the Precursor Ions Quantifier tool using the Total Peptide Amount feature. Retention time alignment was set at 15 min. $\log_2$ abundance ratios were generated for IKAROS, MEIS1 and HOXA10 over ZNF692, and a threshold was set to define enrichment as being greater than twofold ($\log_2$ ratio = 1). Based on western blot analysis and the median value of $\log_2$ ratios called in the MOLM-13 experiment (IKAROS/ZNF692 = −1.64, MEIS1/ZNF692 = −0.73 and IKAROS/ZNF692 = −1.95), we concluded that ZNF692–BirA* induced significantly higher labeling than IKAROS, MEIS1 or HOXA10. Thus, MOLM-13 BioID data were further normalized by subtracting the median value of all $\log_2$ ratios in each comparison from each individual value. No extra normalization was applied to the MV4;11 LFQ data. PSM values from the individual searches described above were added, and any protein with less than two PSMs was excluded from the LFQ analysis. Of those proteins that had one or more isoform detected, the isoform with the most PSMs was retained and the others were removed.

BH3 profiling. BH3 profiling was performed as described previously[46]. Cells were permeabilized with 0.001% digitonin suspended in MEB2 buffer (150 mM mannitol, 10 mM HEPES–KOH, pH 7.5, 150 mM KCl, 1 mM EGTA, 1 mM EDTA, 0.1% BSA, 5 mM succinate) and treated with different BH3-only peptides in a 384-well plate. After a 60-min incubation at 25 °C, cells were fixed with 4% formaldehyde for 10 min at room temperature, followed by neutralization by adding N2 buffer (1.7 M Tris base, 1.25 M glycine, pH 9.1). Cells were stained overnight at 4 °C with Hoechst 33342 (H3570, Invitrogen) and anti-cytochrome C Alexa Fluor 488 antibody (6H2.B4/612308). The rate of loss of cytochrome C was analyzed using the Intellicyt iQue flow cytometer in response to each BH3 peptide. Assays were conducted in triplicate. DMSO and alamethicin were used as negative and positive controls for cytochrome C release.

IKAROS-overexpression cell lines. IKAROS-overexpression vectors were a kind gift from W.G. Kaelin and V. Koduri, DFCI: (1) the wild-type

IKAROS-overexpression vector (CAG-*IKZF1*-WT-FLAG-IRES-GFP, https://www.addgene.org/107387/), (2) a non-degradable mutant IKAROS-overexpression vector (CAG-*IKZF1-V1-Q146H*-FLAG-IRES-GFP, https://www.addgene.org/69048/) and (3) the empty vector control (pLKO5-GFP, https://www.addgene.org/57822). Lentivirus was produced as described above. The MOLM-13 cell line was transduced as described above and sorted using a FACSMelody Cell Sorter (BD) to produce a uniform population of GFP-expressing cells.

Human CD34⁺ cell isolation and *MLL-AF9* transduction. Production of *MLL-AF9*-transduced human CD34⁺ cells has been described[80]. Human CD34⁺ cells were isolated from human cord blood (New York Blood Center) using the EasySep Human Cord Blood CD34 Positive Selection Kit II (Stemcell Technologies). For pre-enrichment, Lymphoprep (Stemcell Technologies) and SepMate columns (Stemcell Technologies) were used. Viral supernatants were generated by cotransfection of HEK293T cells with a retroviral (pMSCV-MLL-AF9-IRES-GFP)[80] expression vector with packaging and envelope vectors (human retrovirus, pUMVC and VSV-G) and X-tremeGene transfection reagent (Millipore). The viral supernatant was filtered through a 0.45-µm filter and was concentrated using Amicon Ultra centrifugal filters (Millipore). Human CD34⁺ cells were plated on RetroNectin-coated plates (Takara) and were spin infected at a 1:1 dilution of virus:medium at 800g and 37 °C for 1.5 h. The cells were dissociated from the plates using enzyme-free dissociation buffer (Gibco) and were plated in fresh medium. Cells were maintained in IMDM with 20% FBS, 1× penicillin–streptomycin (Gibco), 1× β-mercaptoethanol (Gibco), 6 µg ml⁻¹ hIL-3, 10 µg ml⁻¹ hIL-6, 10 µg ml⁻¹ hSCF, 10 µg ml⁻¹ TPO and 10 µg ml⁻¹ FLT3 (Stemcell Technologies) at 37 °C with 5% CO_2. Two days after transduction, GFP-positive cells were sorted using the FACSAria cell sorter (BD Biosciences).

Colony-formation assay. Colony-forming unit assays were performed by plating 200 MOLM-13 CRISPR-modified cells in 3 ml MethoCult GF M3434 medium (Stemcell Technologies). For each sgRNA, four separate methylcellulose plates were used. Colonies were quantified 9 and 12 d after plating by manual counting. On the 13th day of the experiment, each plate was washed with PBS, and cells were centrifuged and resuspended in quadruplicate to run on the LSR Fortessa to quantify the number of cells per plate.

Statistical analysis and reproducibility. No statistical methods were used to predetermine sample sizes, but our sample sizes are similar to those reported in previous publications[24]. Single experiments shown are representative of at least three independent experimental replicates. Data collection and analysis were not performed blind to the conditions of the experiments. For PDX studies, animals were randomized according to weight and leukemia burden before treatment using Excel (Microsoft). Animals injured by gavage and required to be killed were excluded from the analysis. For proliferation assays, dose–response curves were calculated in a variable slope model as a four-parameter dose–response curve (GraphPad Software). Absolute IC_{50} values were calculated by setting the maximal inhibition baseline parameter to 0% and constraining the minimal inhibition top parameter to 100%. The calculation was carried out via non-linear regression of the log of the dose (GraphPad Software). Kaplan–Meier survival curves and paired t-tests were performed using statistical software (GraphPad Prism). GSEA (version 3.0 software, Broad Institute)[81,82] was used to identify functional associations from the described RNA-seq profiles. Global analysis was performed on raw RNA-seq counts; specific query of gene sets of interest was performed in 'pre-ranked' mode using gene lists ranked according to DESeq statistical z scores. Significance cutoffs were assessed on the basis of GSEA standard recommendations: absolute NES ≥ 1, $P \leq 0.05$, Benjamini–Hochberg FDR ≤ 0.25. Gene sets used in the presented data are listed in Supplementary Table 6. Bliss independence and Loewe additivity models were used to assess synergy as described previously[83]. The Bliss independence model calculates a quantitative measure, called the excess over Bliss, which represents the difference between the observed combined effect and the expected combined effect of the two compounds. The Chou–Talalay combination index for the Loewe additivity model is a dose–effect approach to estimate the effect of combining two compounds based upon the dose of each individual compound that produces the same quantitative effect. All data from flow cytometry were analyzed using FlowJo software (Becton Dickinson, version 10.6.2).

Bioinformatic analysis. Raw Illumina sequencer output was converted to FASTQ format using bcl2fastq (version 2.20.0.422) (Illumina). Reads (paired-end 37-mers) were aligned to the human genome (hg19) using STAR (version 2.7.5a)[84] and sorted, and duplicates were marked and removed with picard pipeline tools (version 2.9.4). Final 'deduped' .BAM files were indexed using SAMtools (version 1.95)[85]. Files for data visualization were produced using IGVtools (TDF signal pileups, version 2.3.75)[86] and ngs.plot (pileup heatmaps, ChIP–seq only). ChIP–seq signal peaks were called using MACS2 (version 2.1.4). For RNA-seq data, raw counts were calculated with HTSeq (htseq-count, version 0.11.2)[87]. Raw counts were used to calculate differential expression values with the R Bioconductor DESeq2 package (version 1.24.0)[88]. Results were filtered to exclude non-protein-coding genes (based on Ensembl gene biotype annotations) and low-expressed genes (those with average values <1 in rlog scale for both treatments in comparison).

Expression differentials with adjusted *P* value < 0.05 were considered significant with the additional requirement of a greater than twofold change when indicated. RNA-seq data were further analyzed by using Ingenuity Pathway Analysis (Qiagen, https://www.qiagenbioinformatics.com/products/ingenuitypathway-analysis). For CUT&RUN-seq analysis, FASTQ files were processed using a version of the published CUT&RUNTools suite[44] (release date, 19 August 2019), modified to run on a local computer cluster. Briefly, reads were trimmed using Trimmomatic and aligned to the human genome (hg19) with Bowtie 2 (version 2.3.4.3)[89]. Resulting BAM files were sorted, duplicates were marked and filtered for fragments <120 bp (all with SAMtools version 1.95), and peaks were called (with MACS2 version 2.1.4). ATAC-seq data were processed as described above for ChIP–seq data. Enhancer prediction using the ABC model was carried out as previously described[45]. Heatmap displays for RNA-seq data were generated using the Bioconductor package ComplexHeatmap (version 3.14)[90] and RStudio (version 1.4.1106) with R (version 3.6.0). GNU parallel (version 20161222)[91] was used to facilitate simultaneous processing and analysis of samples.

Publicly available data usage. The Cancer Dependency Map (DepMap) from the Broad Institute of MIT and Harvard[35] was used to examine cancer dependencies on *IKZF1*, *MEN1*, *DOT1L* and *ZFP91* (DepMap 21Q4 Public, figshare dataset, https://doi.org/10.6084/m9.figshare.12280541.v3). The cBio Cancer Genomics Portal (cBioPortal)[34,92] was used to examine *IKZF1* gene expression across a range of cancer subtypes using data from the Cancer Genome Atlas (https://www.cancer.gov/tcga). For ABC enhancer predictions, average Hi-C matrix data were used as recommended[45] and obtained from the Broad Institute of MIT and Harvard (https://github.com/broadinstitute/ABC-Enhancer-Gene-Prediction) as well as an additional publicly available Hi-C dataset for MV4;11 cells[93].

Data availability

Raw and analyzed data for ChIP–seq, CUT&RUN-seq, RNA-seq, ATAC-seq and ABC model predictions have been deposited at the National Center for Biotechnology Information Gene Expression Omnibus under the accession number GSE168463; deposited data correspond to Figs. 3–7 and associated Extended Data Figs 4, 5 and 7–10. All MS data and search results have been deposited to the ProteomeXchange Consortium (http://proteomecentral.proteomexchange.org/cgi/GetDataset?ID=PXD007862) via the PRIDE partner repository with the dataset identifiers PXD025227, PXD025228, PXD025229, PXD025230, PXD025231, PXD025232, PXD025271 and PXD025272. Additional data that support the findings of this study are available from the corresponding author upon reasonable request. Source data are provided with this paper.

References

1. Valk, P. J. et al. Prognostically useful gene-expression profiles in acute myeloid leukemia. *N. Engl. J. Med.* **350**, 1617–1628 (2004).
2. Bullinger, L. et al. Use of gene-expression profiling to identify prognostic subclasses in adult acute myeloid leukemia. *N. Engl. J. Med.* **350**, 1605–1616 (2004).
3. Krivtsov, A. V., Hoshii, T. & Armstrong, S. A. Mixed-lineage leukemia fusions and chromatin in leukemia. *Cold Spring Harb. Perspect. Med.* **7**, a026658 (2017).
4. Novershtern, N. et al. Densely interconnected transcriptional circuits control cell states in human hematopoiesis. *Cell* **144**, 296–309 (2011).
5. Yokoyama, A. et al. The menin tumor suppressor protein is an essential oncogenic cofactor for MLL-associated leukemogenesis. *Cell* **123**, 207–218 (2005).
6. Yokoyama, A. & Cleary, M. L. Menin critically links MLL proteins with LEDGF on cancer-associated target genes. *Cancer Cell* **14**, 36–46 (2008).
7. Okada, Y. et al. hDOT1L links histone methylation to leukemogenesis. *Cell* **121**, 167–178 (2005).
8. Bernt, K. M. et al. MLL-rearranged leukemia is dependent on aberrant H3K79 methylation by DOT1L. *Cancer Cell* **20**, 66–78 (2011).
9. Smith, E., Lin, C. & Shilatifard, A. The super elongation complex (SEC) and MLL in development and disease. *Genes Dev.* **25**, 661–672 (2011).
10. Brown, F. C. et al. MEF2C phosphorylation is required for chemotherapy resistance in acute myeloid leukemia. *Cancer Discov.* **8**, 478–497 (2018).
11. Krivtsov, A. V. et al. Transformation from committed progenitor to leukaemia stem cell initiated by MLL-AF9. *Nature* **442**, 818–822 (2006).
12. Placke, T. et al. Requirement for CDK6 in *MLL*-rearranged acute myeloid leukemia. *Blood* **124**, 13–23 (2014).
13. Faber, J. et al. HOXA9 is required for survival in human *MLL*-rearranged acute leukemias. *Blood* **113**, 2375–2385 (2009).
14. Guo, H. et al. PBX3 is essential for leukemia stem cell maintenance in *MLL*-rearranged leukemia. *Int. J. Cancer* **141**, 324–335 (2017).
15. Kumar, A. R. et al. A role for MEIS1 in *MLL*-fusion gene leukemia. *Blood* **113**, 1756–1758 (2009).
16. Collins, C. et al. C/EBPα is an essential collaborator in Hoxa9/Meis1-mediated leukemogenesis. *Proc. Natl Acad. Sci. USA* **111**, 9899–9904 (2014).
17. Wilkinson, A. C. et al. *RUNX1* is a key target in t(4;11) leukemias that contributes to gene activation through an AF4-MLL complex interaction. *Cell Rep.* **3**, 116–127 (2013).
18. Sun, Y. et al. HOXA9 reprograms the enhancer landscape to promote leukemogenesis. *Cancer Cell* **34**, 643–658 (2018).
19. Cusan, M. et al. LSD1 inhibition exerts its antileukemic effect by recommissioning PU.1- and C/EBPα-dependent enhancers in AML. *Blood* **131**, 1730–1742 (2018).
20. Zhu, N. et al. MLL-AF9- and HOXA9-mediated acute myeloid leukemia stem cell self-renewal requires JMJD1C. *J. Clin. Invest.* **126**, 997–1011 (2016).
21. Zeisig, B. B. et al. *Hoxa9* and *Meis1* are key targets for MLL-ENL-mediated cellular immortalization. *Mol. Cell. Biol.* **24**, 617–628 (2004).
22. Kuhn, M. W. et al. Targeting chromatin regulators inhibits leukemogenic gene expression in *NPM1* mutant leukemia. *Cancer Discov.* **6**, 1166–1181 (2016).
23. Bradner, J. E., Hnisz, D. & Young, R. A. Transcriptional addiction in cancer. *Cell* **168**, 629–643 (2017).
24. Krivtsov, A. V. et al. A menin–MLL inhibitor induces specific chromatin changes and eradicates disease in models of *MLL*-rearranged leukemia. *Cancer Cell* **36**, 660–673 (2019).
25. Borkin, D. et al. Pharmacologic inhibition of the menin–MLL interaction blocks progression of MLL leukemia in vivo. *Cancer Cell* **27**, 589–602 (2015).
26. Klossowski, S. et al. Menin inhibitor MI-3454 induces remission in *MLL1*-rearranged and *NPM1*-mutated models of leukemia. *J. Clin. Invest.* **130**, 981–997 (2020).
27. Daigle, S. R. et al. Potent inhibition of DOT1L as treatment of MLL-fusion leukemia. *Blood* **122**, 1017–1025 (2013).
28. Perner, F. et al. Novel inhibitors of the histone methyltransferase DOT1L show potent antileukemic activity in patient-derived xenografts. *Blood* **136**, 1983–1988 (2020).
29. Uckelmann, H. J. et al. Therapeutic targeting of preleukemia cells in a mouse model of *NPM1* mutant acute myeloid leukemia. *Science* **367**, 586–590 (2020).
30. Stein, E. M. et al. The DOT1L inhibitor pinometostat reduces H3K79 methylation and has modest clinical activity in adult acute leukemia. *Blood* **131**, 2661–2669 (2018).
31. Perner, F. & Armstrong, S. A. Targeting chromatin complexes in myeloid malignancies and beyond: from basic mechanisms to clinical innovation. *Cells* **9**, 2721 (2020).
32. Wang, B. et al. Integrative analysis of pooled CRISPR genetic screens using MAGeCKFlute. *Nat. Protoc.* **14**, 756–780 (2019).
33. Lai, A. Y. & Wade, P. A. Cancer biology and NuRD: a multifaceted chromatin remodelling complex. *Nat. Rev. Cancer* **11**, 588–596 (2011).
34. Cerami, E. et al. The cBio Cancer Genomics Portal: an open platform for exploring multidimensional cancer genomics data. *Cancer Discov.* **2**, 401–404 (2012).
35. Meyers, R. M. et al. Computational correction of copy number effect improves specificity of CRISPR–Cas9 essentiality screens in cancer cells. *Nat. Genet.* **49**, 1779–1784 (2017).
36. Brunetti, L. et al. Mutant NPM1 maintains the leukemic state through HOX expression. *Cancer Cell* **34**, 499–512 (2018).
37. Kronke, J. et al. Lenalidomide causes selective degradation of IKZF1 and IKZF3 in multiple myeloma cells. *Science* **343**, 301–305 (2014).
38. Lu, G. et al. The myeloma drug lenalidomide promotes the cereblon-dependent destruction of Ikaros proteins. *Science* **343**, 305–309 (2014).
39. Kronke, J. et al. Lenalidomide induces ubiquitination and degradation of CK1α in del(5q) MDS. *Nature* **523**, 183–188 (2015).
40. Donovan, K. A. et al. Thalidomide promotes degradation of SALL4, a transcription factor implicated in Duane Radial Ray syndrome. *eLife* **7**, e38430 (2018).
41. Guenther, M. G. et al. Aberrant chromatin at genes encoding stem cell regulators in human mixed-lineage leukemia. *Genes Dev.* **22**, 3403–3408 (2008).
42. Skene, P. J. & Henikoff, S. An efficient targeted nuclease strategy for high-resolution mapping of DNA binding sites. *eLife* **6**, e21856 (2017).
43. Meers, M. P., Bryson, T. D., Henikoff, J. G. & Henikoff, S. Improved CUT&RUN chromatin profiling tools. *eLife* **8**, e46314 (2019).
44. Zhu, Q., Liu, N., Orkin, S. H. & Yuan, G. C. CUT&RUNTools: a flexible pipeline for CUT&RUN processing and footprint analysis. *Genome Biol.* **20**, 192 (2019).
45. Fulco, C. P. et al. Activity-by-contact model of enhancer–promoter regulation from thousands of CRISPR perturbations. *Nat. Genet.* **51**, 1664–1669 (2019).
46. Ryan, J. A., Brunelle, J. K. & Letai, A. Heightened mitochondrial priming is the basis for apoptotic hypersensitivity of CD4+ CD8+ thymocytes. *Proc. Natl Acad. Sci. USA* **107**, 12895–12900 (2010).

47. Samavarchi-Tehrani, P., Samson, R. & Gingras, A. C. Proximity dependent biotinylation: key enzymes and adaptation to proteomics approaches. *Mol. Cell. Proteomics* **19**, 757–773 (2020).

48. Guirguis, A. A. & Ebert, B. L. Lenalidomide: deciphering mechanisms of action in myeloma, myelodysplastic syndrome and beyond. *Curr. Opin. Cell Biol.* **37**, 61–67 (2015).

49. Fink, E. C. et al. Crbn^I391V is sufficient to confer in vivo sensitivity to thalidomide and its derivatives in mice. *Blood* **132**, 1535–1544 (2018).

50. Francis, O. L., Payne, J. L., Su, R. J. & Payne, K. J. Regulator of myeloid differentiation and function: the secret life of Ikaros. *World J. Biol. Chem.* **2**, 119–125 (2011).

51. Boutboul, D. et al. Dominant-negative *IKZF1* mutations cause a T, B, and myeloid cell combined immunodeficiency. *J. Clin. Invest.* **128**, 3071–3087 (2018).

52. Yoshida, T., Ng, S. Y., Zuniga-Pflucker, J. C. & Georgopoulos, K. Early hematopoietic lineage restrictions directed by Ikaros. *Nat. Immunol.* **7**, 382–391 (2006).

53. Martinez-Hoyer, S. et al. Loss of lenalidomide-induced megakaryocytic differentiation leads to therapy resistance in del(5q) myelodysplastic syndrome. *Nat. Cell Biol.* **22**, 526–533 (2020).

54. Georgopoulos, K. Haematopoietic cell-fate decisions, chromatin regulation and ikaros. *Nat. Rev. Immunol.* **2**, 162–174 (2002).

55. Bottardi, S., Mavoungou, L. & Milot, E. IKAROS: a multifunctional regulator of the polymerase II transcription cycle. *Trends Genet.* **31**, 500–508 (2015).

56. Ding, Y. et al. Ikaros tumor suppressor function includes induction of active enhancers and super-enhancers along with pioneering activity. *Leukemia* **33**, 2720–2731 (2019).

57. Scacheri, P. C. et al. Genome-wide analysis of menin binding provides insights into MEN1 tumorigenesis. *PLoS Genet.* **2**, e51 (2006).

58. Skucha, A. et al. MLL-fusion-driven leukemia requires SETD2 to safeguard genomic integrity. *Nat. Commun.* **9**, 1983 (2018).

59. Hughes, C. M. et al. Menin associates with a trithorax family histone methyltransferase complex and with the *Hoxc8* locus. *Mol. Cell* **13**, 587–597 (2004).

60. Bres, V., Yoshida, T., Pickle, L. & Jones, K. A. SKIP interacts with c-Myc and menin to promote HIV-1 Tat transactivation. *Mol. Cell* **36**, 75–87 (2009).

61. Agarwal, S. K. et al. Menin interacts with the AP1 transcription factor JunD and represses JunD-activated transcription. *Cell* **96**, 143–152 (1999).

62. Huang, J. et al. The same pocket in menin binds both MLL and JUND but has opposite effects on transcription. *Nature* **482**, 542–546 (2012).

63. Wu, Y. et al. Disruption of the menin–MLL interaction triggers menin protein degradation via ubiquitin-proteasome pathway. *Am. J. Cancer Res.* **9**, 1682–1694 (2019).

64. Xie, C. H. et al. Efficacy and safety of lenalidomide for the treatment of acute myeloid leukemia: a systematic review and meta-analysis. *Cancer Manag. Res.* **10**, 3637–3648 (2018).

65. Ebert, B. L. & Kronke, J. Inhibition of casein kinase 1 α in acute myeloid leukemia. *N. Engl. J. Med.* **379**, 1873–1874 (2018).

66. Le Roy, A. et al. Immunomodulatory drugs exert anti-leukemia effects in acute myeloid leukemia by direct and immunostimulatory activities. *Front. Immunol.* **9**, 977 (2018).

67. Fang, J. et al. A calcium- and calpain-dependent pathway determines the response to lenalidomide in myelodysplastic syndromes. *Nat. Med.* **22**, 727–734 (2016).

68. Kluk, M. J. et al. Validation and implementation of a custom next-generation sequencing clinical assay for hematologic malignancies. *J. Mol. Diagn.* **18**, 507–515 (2016).

69. Townsend, E. C. et al. The public repository of xenografts enables discovery and randomized phase II-like trials in mice. *Cancer Cell* **29**, 574–586 (2016).

70. Chi, H. T. et al. Detection of exon 12 type A mutation of *NPM1* gene in IMS-M2 cell line. *Leuk. Res.* **34**, 261–262 (2010).

71. Fei, T. et al. Deciphering essential cistromes using genome-wide CRISPR screens. *Proc. Natl Acad. Sci. USA* **116**, 25186–25195 (2019).

72. Li, W. et al. MAGeCK enables robust identification of essential genes from genome-scale CRISPR/Cas9 knockout screens. *Genome Biol.* **15**, 554 (2014).

73. Doench, J. G. et al. Rational design of highly active sgRNAs for CRISPR–Cas9-mediated gene inactivation. *Nat. Biotechnol.* **32**, 1262–1267 (2014).

74. Dignam, J. D., Lebovitz, R. M. & Roeder, R. G. Accurate transcription initiation by RNA polymerase II in a soluble extract from isolated mammalian nuclei. *Nucleic Acids Res.* **11**, 1475–1489 (1983).

75. Lu, X. et al. MTA2/NuRD regulates B cell development and cooperates with OCA-B in controlling the pre-B to immature B cell transition. *Cell Rep.* **28**, 472–485 (2019).

76. McAlister, G. C. et al. MultiNotch MS³ enables accurate, sensitive, and multiplexed detection of differential expression across cancer cell line proteomes. *Anal. Chem.* **86**, 7150–7158 (2014).

77. R Core Team. *R: A Language and Environment for Statistical Computing* (R Foundation for Statistical Computing, 2014).

78. Ritchie, M. E. et al. Limma powers differential expression analyses for RNA-sequencing and microarray studies. *Nucleic Acids Res.* **43**, e47–e47 (2015).

79. Mellacheruvu, D. et al. The CRAPome: a contaminant repository for affinity purification–mass spectrometry data. *Nat. Methods* **10**, 730–736 (2013).

80. Olsen, S. N. et al. MLL::AF9 degradation induces rapid changes in transcriptional elongation and subsequent loss of an active chromatin landscape. *Mol. Cell* **82**, 1140–1155 (2022).

81. Subramanian, A. et al. Gene set enrichment analysis: a knowledge-based approach for interpreting genome-wide expression profiles. *Proc. Natl Acad. Sci. USA* **102**, 15545–15550 (2005).

82. Mootha, V. K. et al. PGC-1α-responsive genes involved in oxidative phosphorylation are coordinately downregulated in human diabetes. *Nat. Genet.* **34**, 267–273 (2003).

83. Iniguez, A. B. et al. Resistance to epigenetic-targeted therapy engenders tumor cell vulnerabilities associated with enhancer remodeling. *Cancer Cell* **34**, 922–938 (2018).

84. Dobin, A. et al. STAR: ultrafast universal RNA-seq aligner. *Bioinformatics* **29**, 15–21 (2013).

85. Li, H. et al. The Sequence Alignment/Map format and SAMtools. *Bioinformatics* **25**, 2078–2079 (2009).

86. Robinson, J. T. et al. Integrative genomics viewer. *Nat. Biotechnol.* **29**, 24–26 (2011).

87. Anders, S., Pyl, P. T. & Huber, W. HTSeq—a Python framework to work with high-throughput sequencing data. *Bioinformatics* **31**, 166–169 (2015).

88. Love, M. I., Huber, W. & Anders, S. Moderated estimation of fold change and dispersion for RNA-seq data with DESeq2. *Genome Biol.* **15**, 550 (2014).

89. Langmead, B. & Salzberg, S. L. Fast gapped-read alignment with Bowtie 2. *Nat. Methods* **9**, 357–359 (2012).

90. Gu, Z., Eils, R. & Schlesner, M. Complex heatmaps reveal patterns and correlations in multidimensional genomic data. *Bioinformatics* **32**, 2847–2849 (2016).

91. Tange, O. GNU parallel—the command-line power tool. *The USENIX Magazine* **36**, 42–47 (2011).

92. Gao, J. et al. Integrative analysis of complex cancer genomics and clinical profiles using the cBioPortal. *Sci. Signal.* **6**, pl1 (2013).

93. Wang, X. Q. D. et al. Three-dimensional regulation of *HOXA* cluster genes by a cis-element in hematopoietic stem cell and leukemia. Preprint at *bioRxiv* https://doi.org/10.1101/2020.04.16.017533 (2020).

Author contributions

S.A.A. supervised the study. S.A.A., B.J.A., J.A.C. and W.B. conceived the study and performed data analysis. C.H. and Q.Z. performed bioinformatic analysis. B.J.A., J.A.C., W.B., R.P.N., S. Parvin and K.A.D. performed experiments. A.C.P.T., S. Perlee, Y.J.K., J.A.H. and N.A.E. provided technical assistance. A.C., S.N.O., F.P., H.R., G.M.M., A.L., E.S.F., Y.P. and X.S.L. contributed to critical experimental planning and resources. B.J.A. and S.A.A. wrote the first draft of the manuscript. All authors contributed to editing subsequent manuscript drafts.

Competing interests

S.A.A. has been a consultant and/or shareholder for Neomorph, Imago BioSciences, Vitae–Allergan Pharma, Cyteir Therapeutics, C4 Therapeutics, Accent Therapeutics and Mana Therapeutics. S.A.A. is an inventor on a patent application related to MENIN inhibition WO/2017/132398A1. S.A.A. has received research support from

Additional information

Extended data is available for this paper at https://doi.org/10.1038/s43018-022-00366-1.

Supplementary information The online version contains supplementary material
available at https://doi.org/10.1038/s43018-022-00366-1.
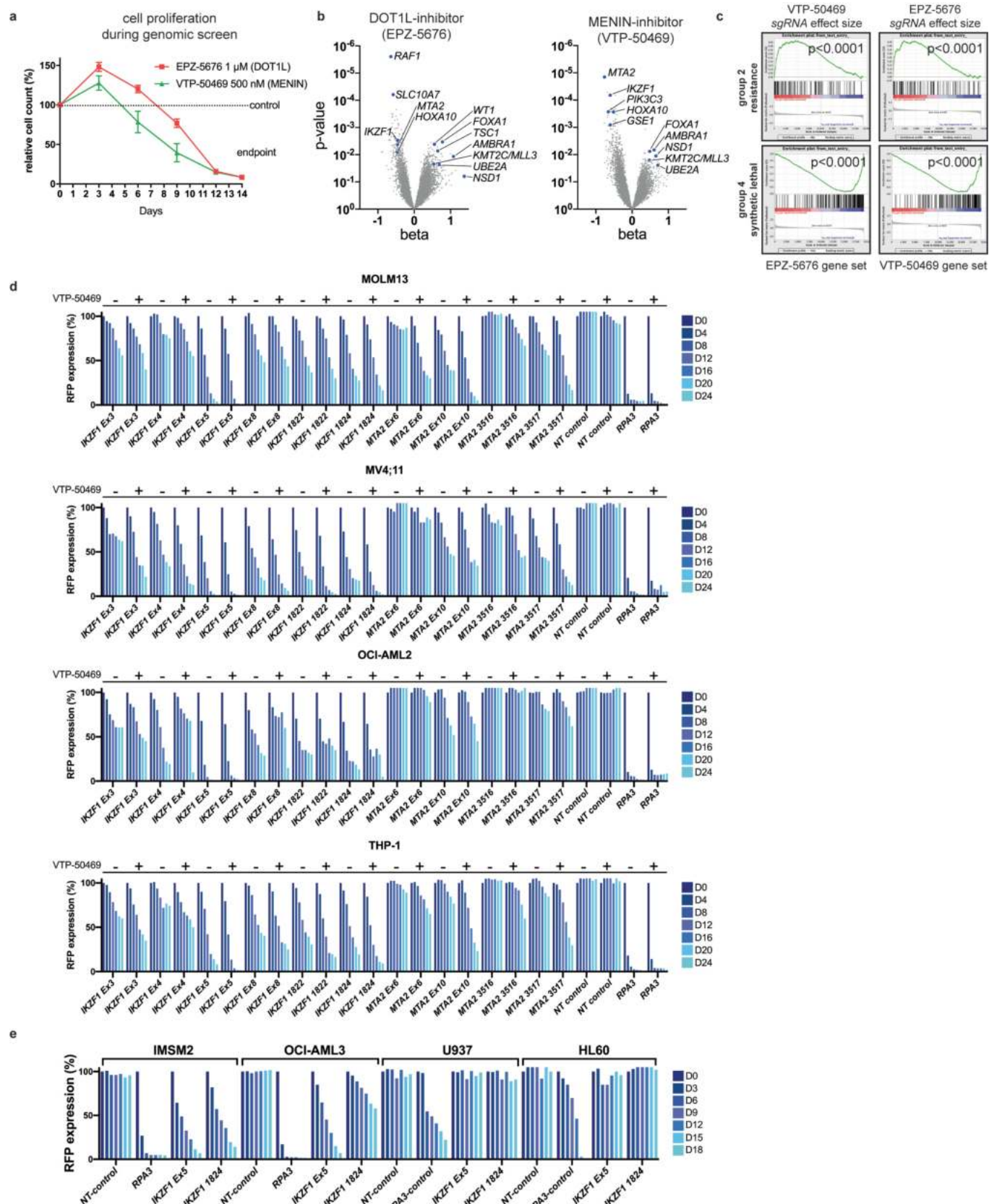
Correspondence and requests for materials should be addressed to Scott A. Armstrong.

Peer review information *Nature Cancer* thanks the anonymous reviewers for their
contribution to the peer review of this work.

Reprints and permissions information is available at www.nature.com/reprints.

Publisher's note Springer Nature remains neutral with regard to jurisdictional claims in
published maps and institutional affiliations.
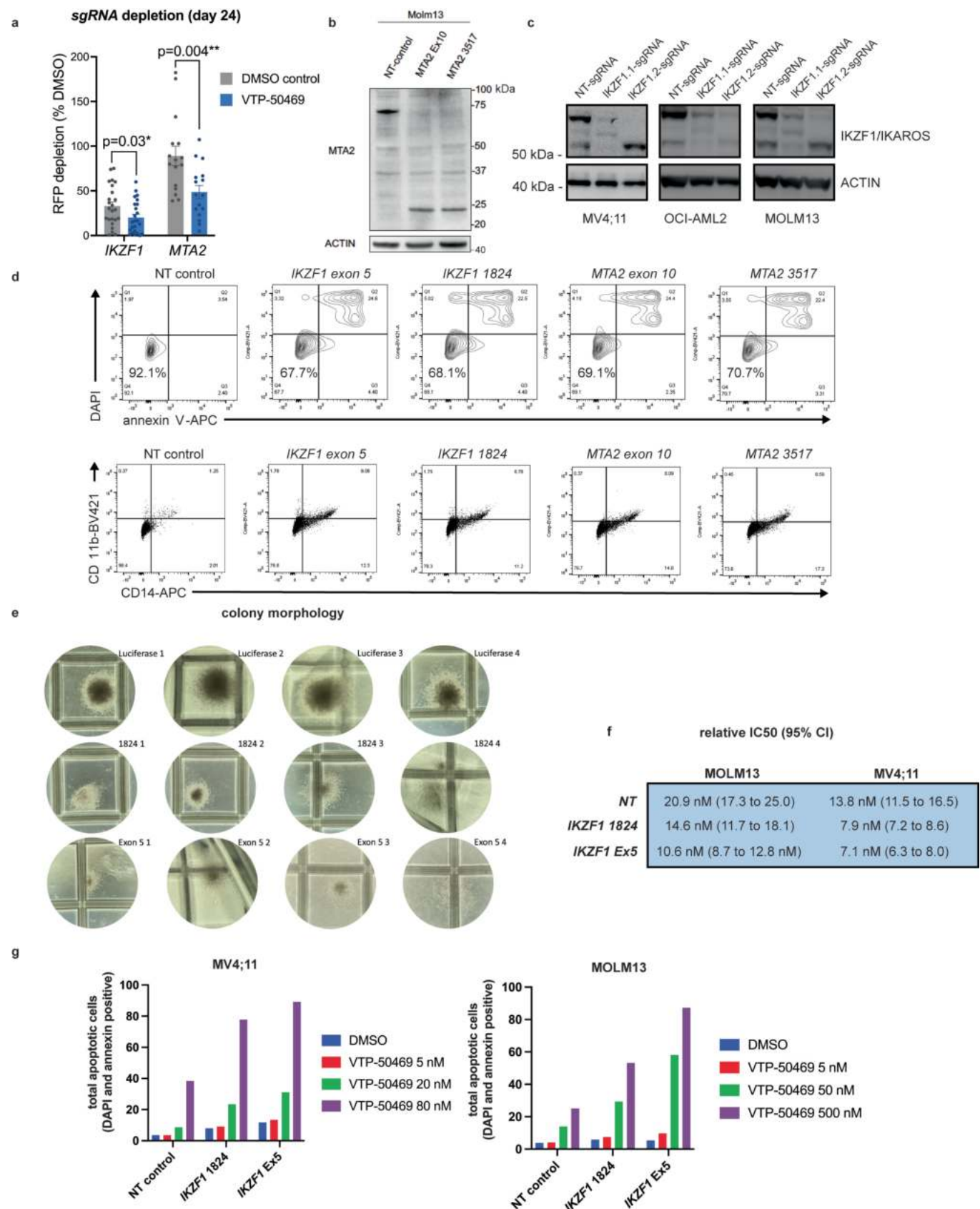
**Extended Data Fig. 1 | See next page for caption.**
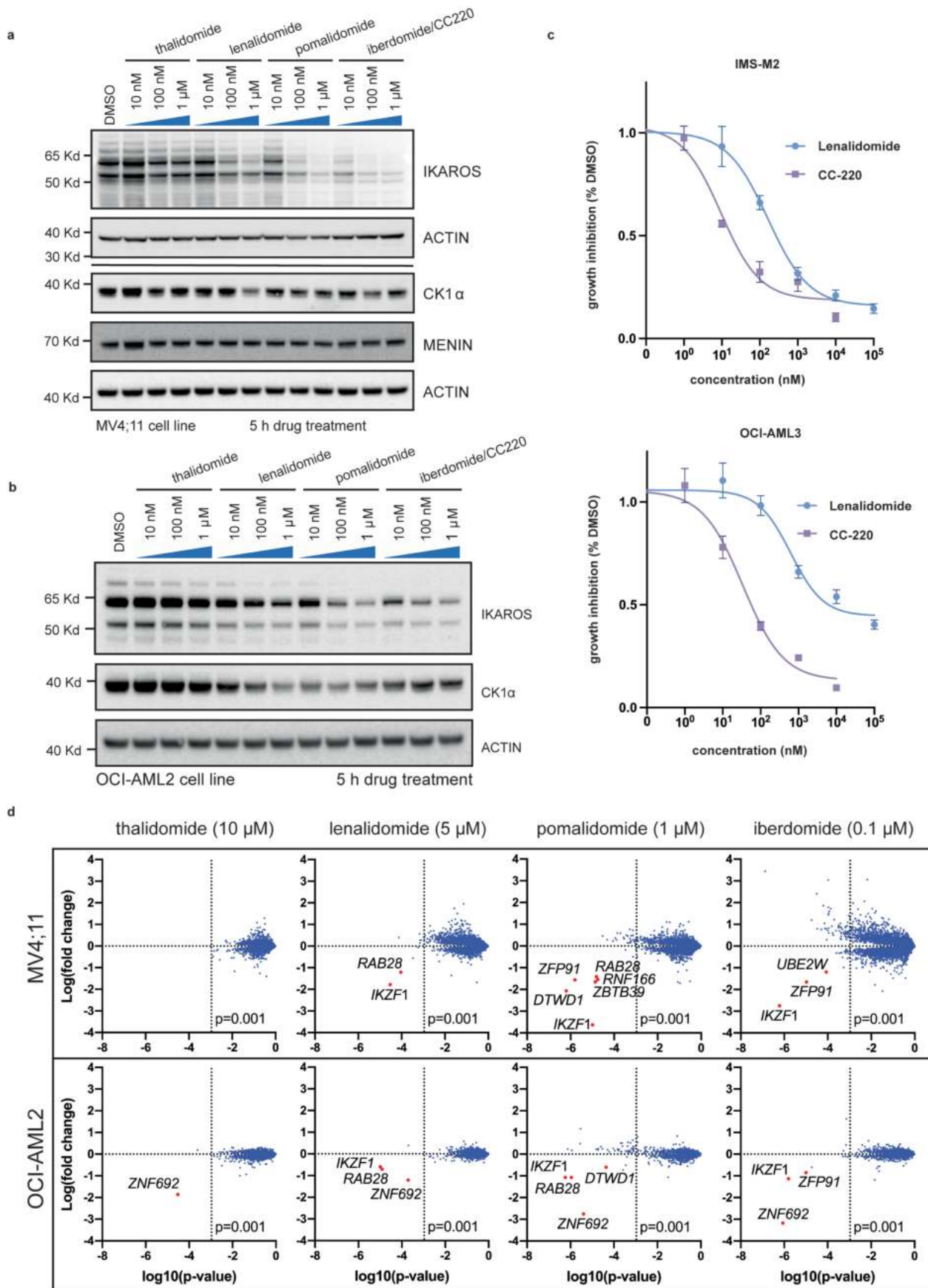
Extended Data Fig. 1 | Chromatin remodeling complexes modulate the cellular response to therapeutic targeting of *MLL-r* driven gene expression.
a, Proliferation assay conducted in real-time during the functional genomic screen showing cell number over time. Data represent mean +/−SEM (n = 4).
b, Volcano plots depicting Wald p-value and beta value calculated using MAGeCK MLE for VTP-50469 and EPZ-5676, comparing the vehicle-treated and drug-treated state on Day 14. **c**, Gene set testing comparing the behaviour of group 2 (resistance) and group 4 (synthetic lethal) genetic hits between each screen. Family-wise error rate p-value determined by GSEA computational method. **d**, Expanded panels of CRISPR/Cas9-based competition assays targeting either *IKZF1* or *MTA2* monitoring *sgRNA*-RFP expression over time in Cas9-expressing in 4 *MLL-r* human AML cell lines (MOLM13, MV4;11, OCI-AML2 and THP-1), with and without concurrent treatment with the MENIN inhibitor, VTP-50469. **e**, CRISPR/Cas9-based competition assays targeting *IKZF1* monitoring *sgRNA*-RFP expression over time in 4 non-MLL-fusion human AML cell lines (IMSM2, OCI-AML3, U937 and HL60) expressing Cas9. IMSM2 and OCI-AML3 carry the *NPM1c* mutation.
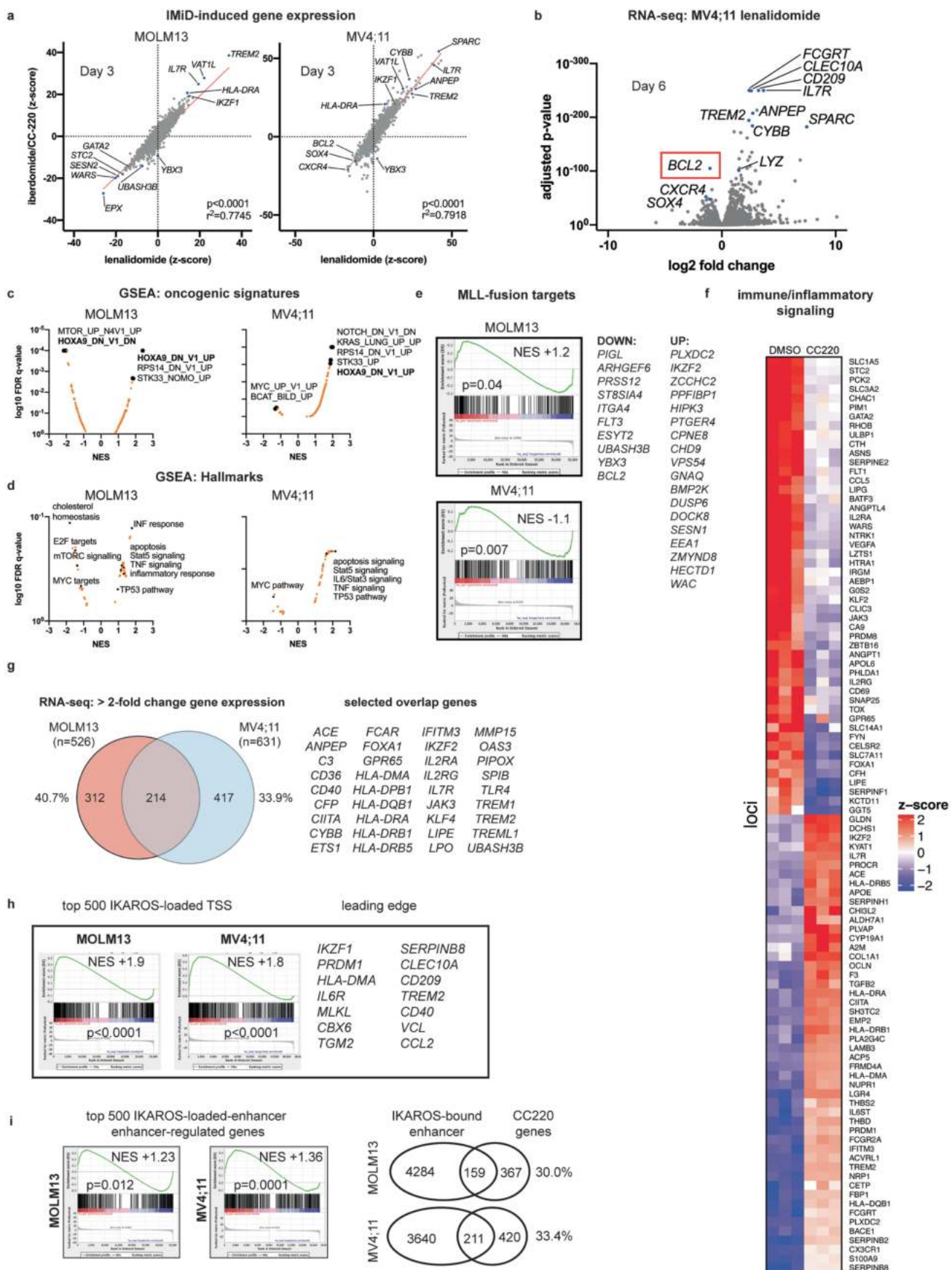
Extended Data Fig. 2 | See next page for caption.

Extended Data Fig. 2 | Using CRISPR/Cas9 to genetically target *IKZF1* and *MTA2* and validate genomic screen findings. a, Combined analysis of sgRNA depletion across samples, depicted in Extended Data Fig. 1d, showing enhanced sgRNA depletion in the presence of the MENIN-inhibitor, VTP-50469, despite the disadvantage of drug-induced cell cycle arrest. Data represent mean $+/-$ SEM with p-value by two-tail t-test evaluated for n $=$ 4 cell lines and n $=$ 6 sgRNAs targeting *IKZF1* or n $=$ 4 sgRNAs targeting *MTA2*. **b**, Western blot analysis for MTA2 protein in sgRNA-RFP sorted cells comparing *MTA2*-targeted bulk cell populations with non-targeting control and ACTIN used as a loading control. **c**, Western blot analysis for IKAROS protein in sgRNA-RFP sorted cells comparing *IKZF1*-targeted bulk cell populations with non-targeting control and ACTIN used as loading control. **d**, Analysis of annexin V staining (apoptosis) and CD11b/CD14 (monocytic differentiation) using flow cytometry 7 days following CRISPR/Cas9-mediated deletion of either *IKZF1* or *MTA2*. Representative experiment is shown. **e**, Colony forming assay comparing MOLM13 cells with sgRNA targeting *Luciferase* (Non-Targeting) control versus two different sgRNAs targeting *IKZF1* (n $=$ 4 per sgRNA), representative colony morphology is shown. **f**, Relative IC$_{50}$ for proliferation assays, pertaining to Fig. 1j, comparing MOLM13 cells with sgRNA targeting *Luciferase* (Non-Targeting control) and two sgRNAs targeting *IKZF1* (n $=$ 3 per sgRNA) upon treatment with MENIN inhibition. **g**, Apoptosis assay in MOLM13 and MV4;11 cell lines testing the impact of *sgRNA*s targeting *Luciferase* (NT control) versus two sgRNAs targeting *IKZF1* on the response to MENIN inhibition with VTP-50469, using doses indicated. Apoptosis was assessed by DAPI exclusion (viability) and annexin V staining with 50,000 cells analysed per sample. Representative example of multiple independent experiments.
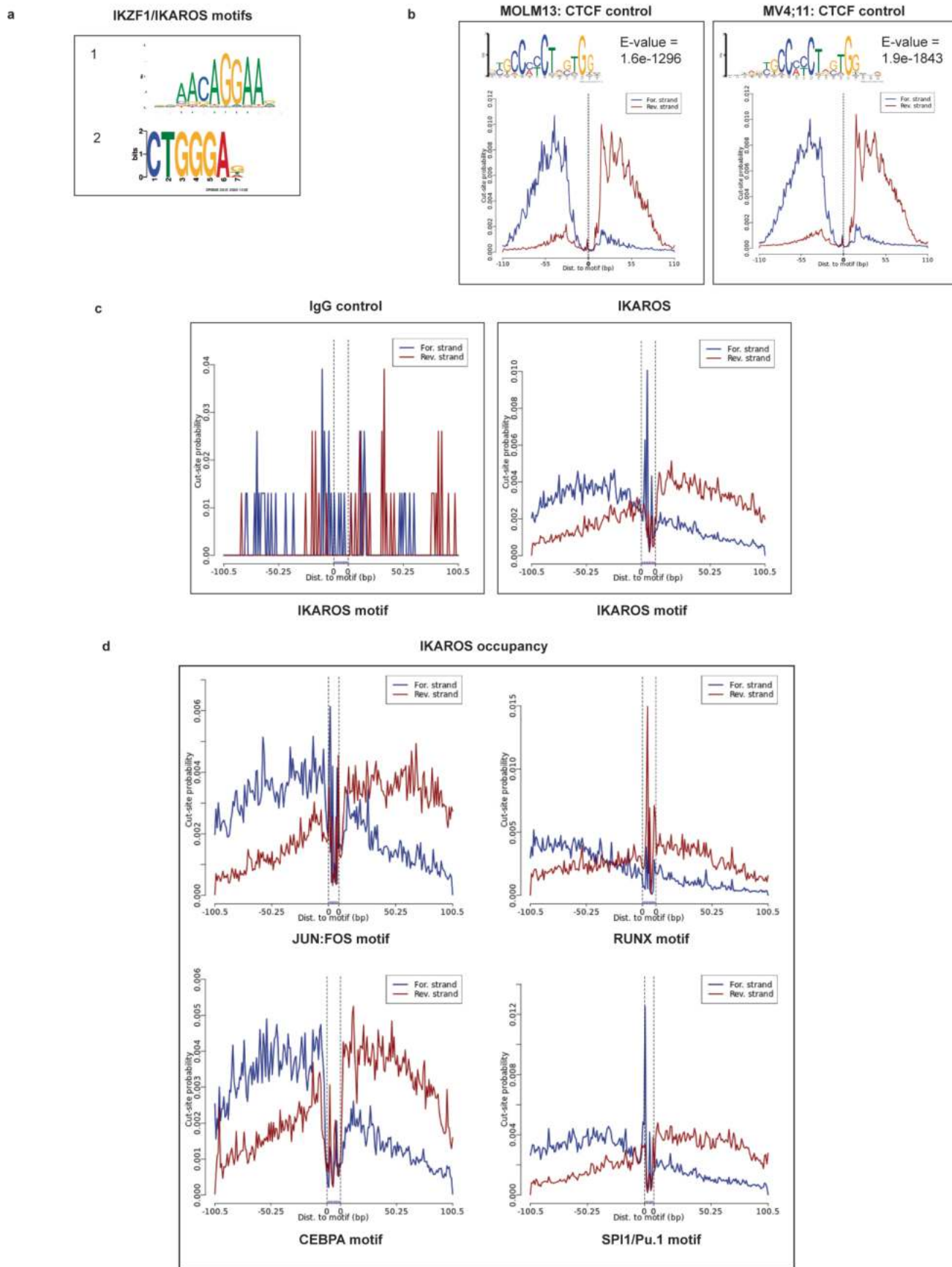
Extended Data Fig. 3 | See next page for caption.

Extended Data Fig. 3 | IMiDs effectively target IKAROS protein for degradation in human *MLL-r* AML. a, Western blot analysis for IKAROS, CK1α and MENIN protein following treatment of MV4;11 human *MLL-r* AML cell line for 5 hours with increasing doses of THAL, LEN, POM and CC220, using ACTIN as a loading control. **b**, Western blot analysis for IKAROS and CK1α following treatment of OCI-AML2 human *MLL-r* AML cell line for 5 hours with increasing doses of THAL, LEN, POM and CC220, using ACTIN as a loading control. **c**, LEN and CC220 dose-response curves on: Day 9 of treatment for the *NPM1*-mutant (*NPM1c*) IMSM2 human AML cell line cell (Absolute IC_{50} 267.0 nM [95% CI 189.6 to 381.0] for LEN, 17.3 nM [95% CI 9.3 to 37.8] for CC220) and Day 18 of treatment for the *NPM1*-mutant (*NPM1c*) OCI-AML3 human AML cell line (Absolute IC_{50} 4626 nM [95% CI could not be calculated] for LEN, 57.7 nM [95% CI 33.1 to 101.5] for CC220). Data represent mean +/−SEM with absolute IC50 indicated (n = 3). **d**, Scatterplot for MS determination of IMiD substrates 5 hours after drug treatment in the MV4;11 and OCI-AML2 cell lines. Data represent the log-fold change in abundance and log10(p-value). p-value determined by moderated t-test as implemented by the Bioconductor Limma package.
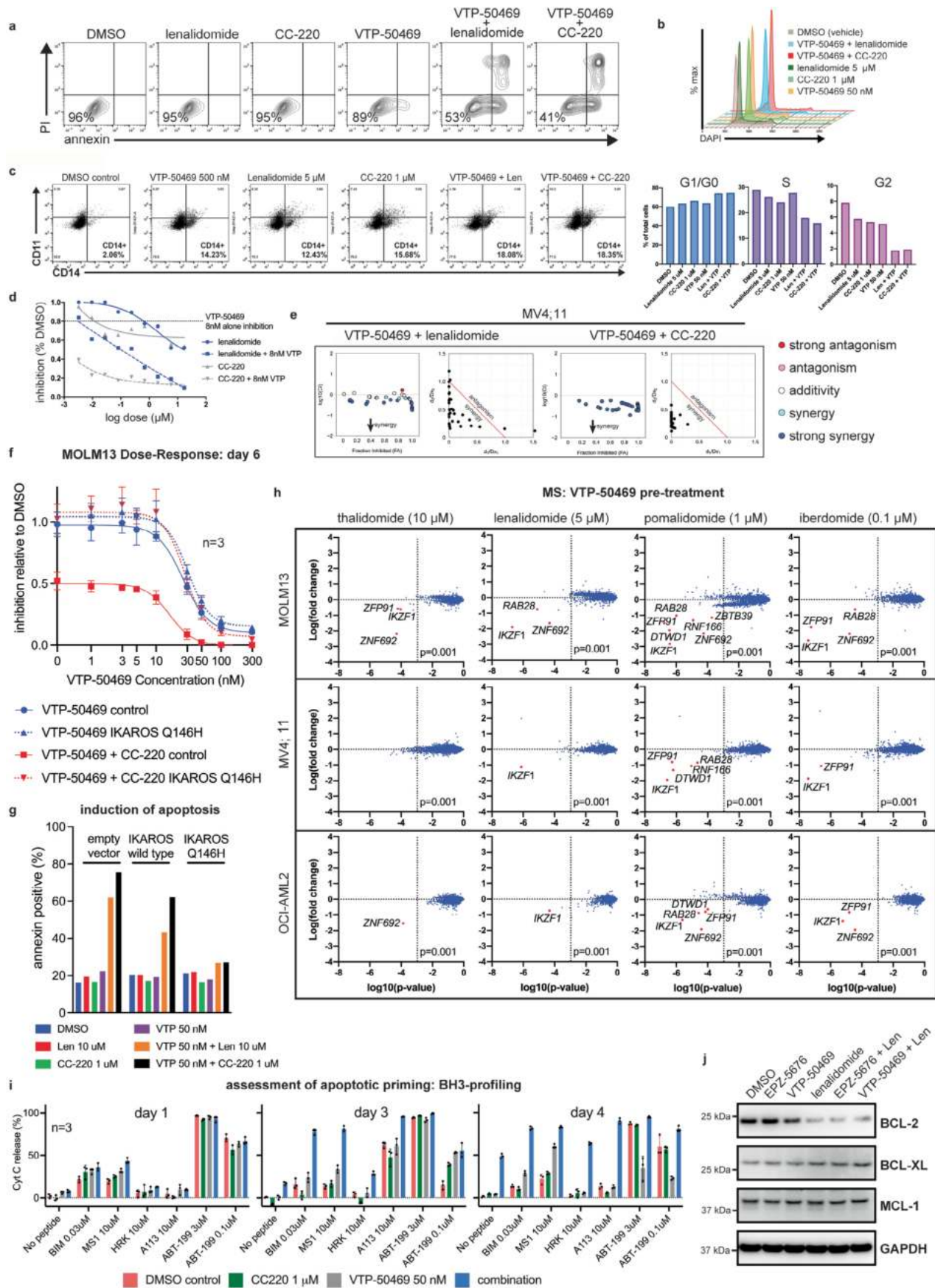
Extended Data Fig. 4 | See next page for caption.

Extended Data Fig. 4 | IKAROS degradation perturbs diverse cellular pathways. a, RNA-seq dot-plot with linear regression showing z-score for differential gene expression correlating LEN (5 µM) and CC220 (1 µM) treatment for 3 days. **b**, RNA-seq volcano plot for MV4;11 treated with LEN for 6 days. **c**, GSEA results for 'oncogenic signatures' for RNA-seq data on Day 3. Dot plot is shown of the log10 false discovery rate (FDR) q-value and normalized enrichment score (NES) as determined by GSEA computational method. **d**, GSEA results for 'Hallmarks' signatures. Dot plot is shown of the log10 false discovery rate (FDR) q-value and normalized enrichment score (NES) as determined by the GSEA computational method. **e**, Bar code plots created using the GSEA tool for putative MLL-fusion target genes with selected genes from leading edge analysis indicated with adj-p-value<0.05 in MOLM13 or MV4;11. Normalized enrichment score and family-wise error rate p-value as determined by GSEA computational method. **f**, Gene expression z-score heatmap for selected genes within immune regulatory and inflammatory pathways under treatment with CC220 (n=3) compared to DMSO-treated control (n=3). **g**, Venn diagram for genes displaying > 2-fold change in expression following CC-220 treatment comparing cell lines. Gene number and percentage overlap is indicated. Selected genes deregulated in both cell lines are indicated. **h**, Correlation of IKAROS-bound gene TSSes, determined by ChIP-seq, with RNA-seq changes. Bar code plot showing gene expression changes following treatment with CC220 (3 days) for the top 500 genes bound by IKAROS (by peak enrichment over background). Selected genes from leading edge analysis indicated. Normalized enrichment score and family-wise error rate p-value determined by GSEA computational method. **i**, Correlation of IKAROS-bound enhancers, determined by ChIP-seq and the ABC prediction tool, with RNA-seq gene expression changes. Bar code plots display gene expression changes following treatment with CC-220 (3 days) for the top 500 genes predicted to be regulated by IKAROS-bound enhancers (by peak enrichment over background at enhancers). Normalized enrichment score and family-wise error rate p-value determined by GSEA computational method. Venn diagram for overlap between gene expression change and genes predicted to be regulated by the top 1000 IKAROS-bound enhancers.
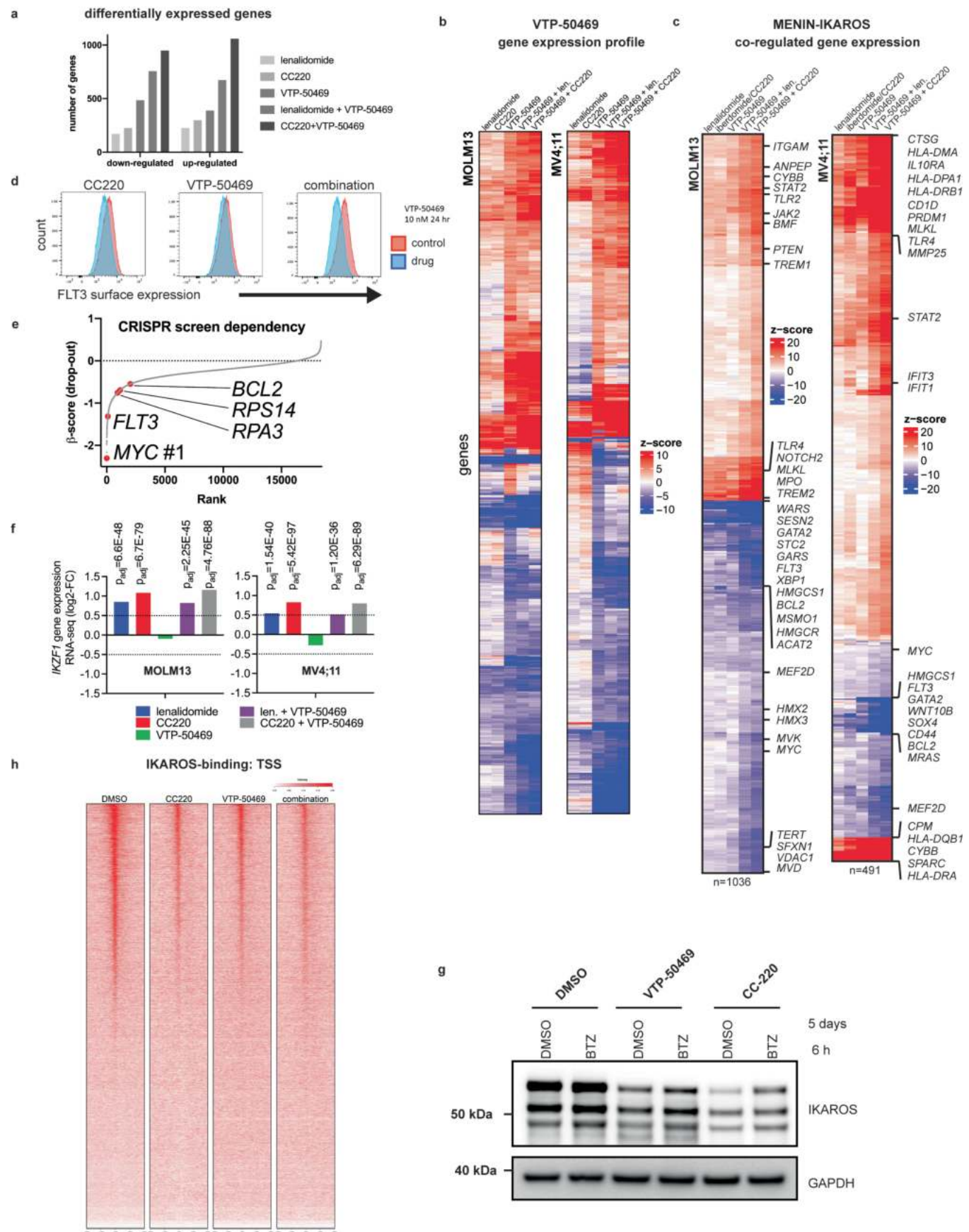
Extended Data Fig. 5 | See next page for caption.

Extended Data Fig. 5 | IKAROS CUT&RUN motif foot printing. a, *IKZF1* DNA-binding motifs. **b**, Foot printing for CTCF protein over the *CTCF* motif for each cell line; used as a positive control for motif detection. Result for CUT&RUNTools *de novo* DREME motif detection is shown with highly significant discovery of the known *CTCF* motif. MEME and E-value is indicated. **c**, CUT&RUNTools foot printing for IKAROS and IgG control over the *IKZF1* motif in the MOLM13 cell line. Cut site probability distribution as determined by CUT&RUNTools. **d**, CUT&RUNTools foot printing for IKAROS over the JUN:FOS motif (centrally bound), CEBPα motif (centrally bound), SPI/Pu.1 motif (centrally bound) and the RUNX motif (non-centrally bound), as indicated, in the MOLM13 cell line. Cut site probability distribution as determined by CUT&RUNTools.
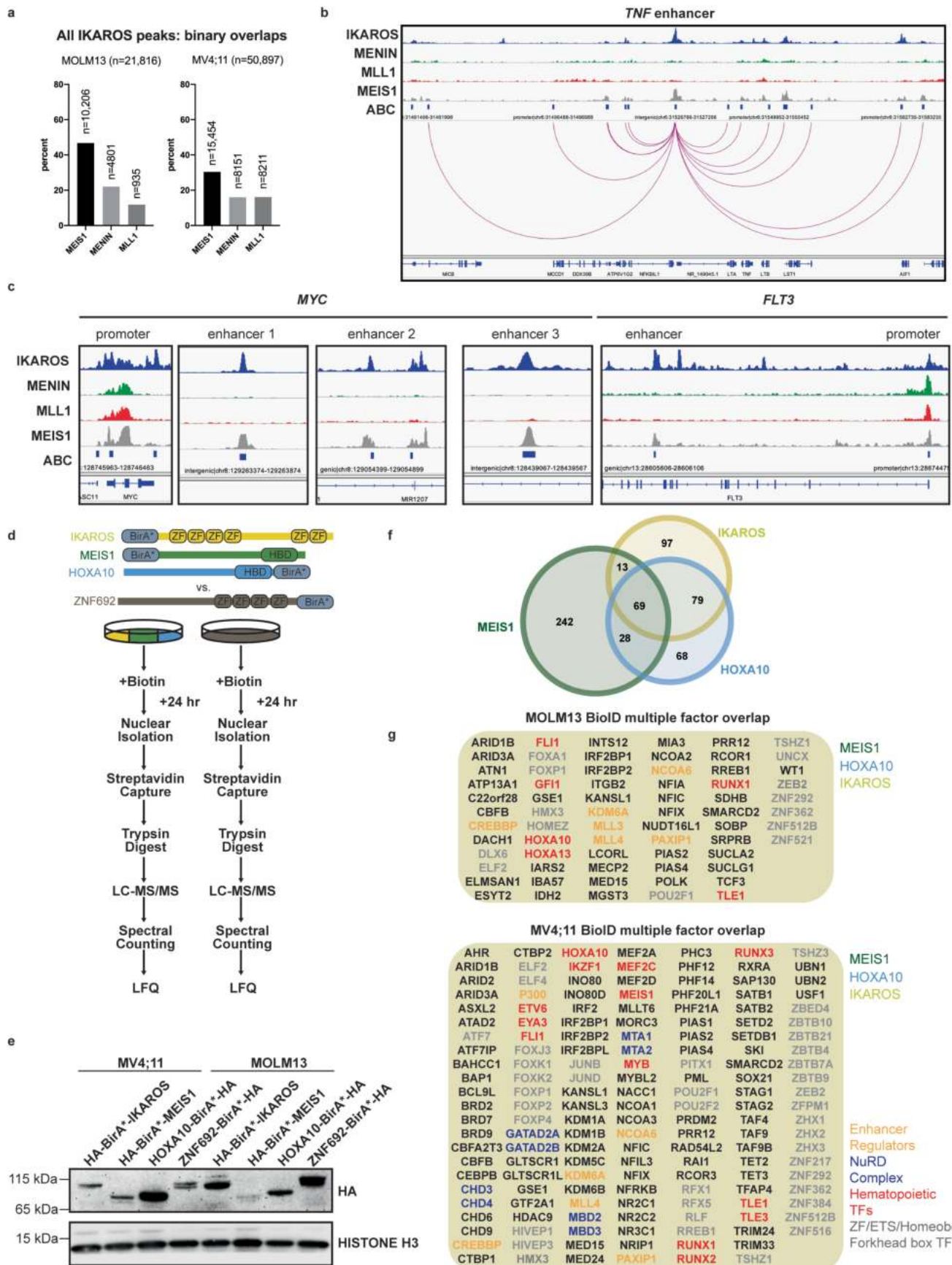
**Extended Data Fig. 6 | See next page for caption.**

Extended Data Fig. 6 | Combined targeting of MENIN and IKAROS. a, Annexin V staining (apoptosis) by flow cytometry following 6 days treatment with VTP-50469, LEN, CC220 and combination (MOLM13). **b**, Cell cycle analysis: histogram for DAPI stain and bar graphs displaying cell cycle stage (%) are shown for each condition. Representative experiment shown. (MOLM13) **c**, CD11b/CD14 expression measured by flow cytometry 6 days following treatment with VTP-50469, LEN, CC220 and combination (MOLM13). Representative experiment shown. **d**, Dose-response curves for LEN and CC220, with and without VTP-50469 (8 nM), compared to VTP-50469 alone (dotted line) measured by Cell-Titer Glo in MV4;11 for synergy studies. **e**, Chou-Talalay synergy analysis for VTP-50469 in combination with LEN or CC-220 (MV4;11). Chou-Talalay Combination Index (CI) plots (left panel) and normalized isobolograms (right panel) are shown for each IMiD-VTP-50469 combination (day 6). Line of additivity is shown (red). **f**, CC-220 and MENIN inhibitor dose response curves (day 6) with and without overexpression of non-degradable IKAROS (Q146H) in MOLM13. Data represent mean +/−SD with non-linear regression curve fit shown. **g**, IMiD and MENIN inhibitor apoptosis after 6 days treatment, with and without overexpression of a wild-type IKAROS or non-degradable IKAROS mutant (Q146H) in MOLM13. **h**, Scatterplots for mass spectrometry (MS) results on MOLM13, MV4;11 and OCI-AML2 cell lines after 5 days pre-treatment with VTP-50469 and then treatment with THAL, LEN, POM and CC-220 (iberdomide), for 5 h. Data represent the log-fold change in abundance and log10(p-value). p-value determined by moderated t-test as implemented by the Bioconductor Limma package. **i**, BH3-profiling in MV4;11 under drug treatments indicated. Cytochrome C (Cyt C) release was measured. Data represent mean +/−SEM (n = 3). **j**, Western blot analysis for BCL2, MCL1 and BCL-XL protein following treatment of OCI-AML2 human *MLL-r* AML cell line for 72 hours with LEN, EPZ-5676, VTP-50469 and each combination, using GAPDH as a loading control.

**Extended Data Fig. 7 | See next page for caption.**
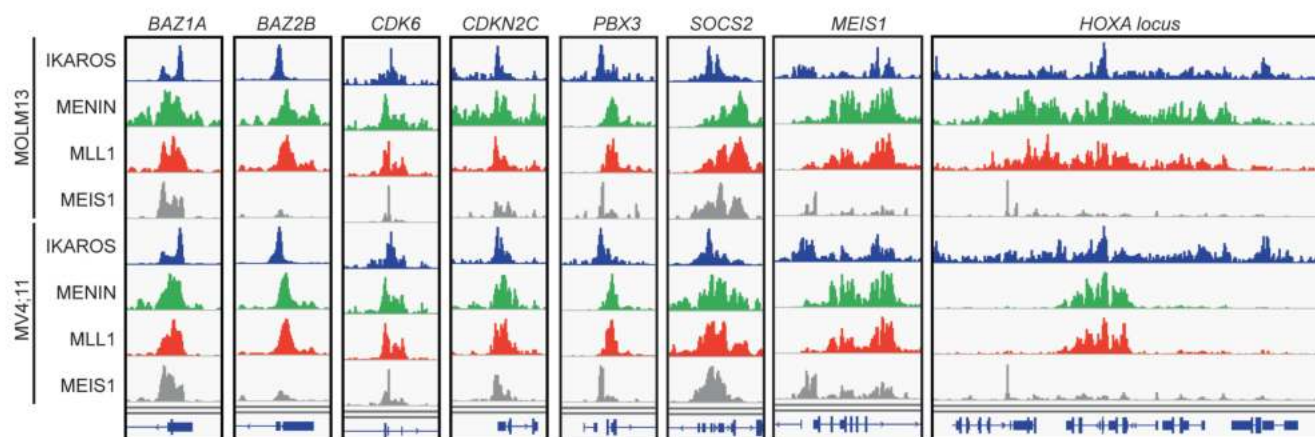
Extended Data Fig. 7 | MENIN and IKAROS display overlapping functions in regulation of gene expression. a, Number of differentially expressed genes (greater than 2-fold change and adjusted p-value <0.05) from RNA-seq data for MOLM13 and MV4;11 cell lines treated with CC220 1 μM (n = 3), VTP-50469 50 nM (n = 3) and the combination (n = 3) for 3 days. **b**, Heatmap showing DESeq2 statistical z-score for all genes deregulated under treatment with VTP-50469 alone across all other treatment groups. **c**, Heatmap of DESeq2 statistical z-score for MENIN and IKAROS co-regulated gene expression. Showing genes with shared or additive regulation. Selected genes are indicated. **d**, Cell surface expression of FLT3 as measured by flow cytometry in the MOLM13 cell line. Cells were pre-treated for 2 days with CC220 or DMSO control and then VTP-50469 was added for 24 hours. **e**, CRISPR screen beta scores from MAGeCK MLE comparing *sgRNA* representation at day 0 compared to day 14 in the DMSO-treated control samples for the MOLM13 cell line. Negative beta scores for *MYC*, *FLT3*, *RPA3* (common essential gene), *RPS14*, and *BCL2* are indicated. **f**, Gene expression for *IKZF1* as determined by RNA-seq in MOLM13 and MV4;11, indicating log-2-fold change value and adjusted p-value determined using DESeq2. **g**, Western blot analysis for IKAROS protein in the MOLM13 cell line following 5 days treatment with either VTP-50469 or iberdomide/CC220, followed by rescue treatment with bortezomib (BTZ) for 6 hours, using GAPDH as a loading control. Performed in the presence of the broad-spectrum caspase inhibitor, QV-D-OPH, to prevent cell death. **h**, Tornado plots depicting global IKAROS chromatin binding at TSSes, as determined by CUT&RUN in the MOLM13 cell line.
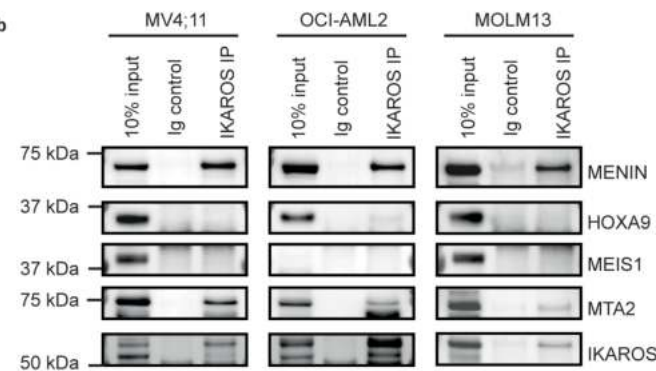
Extended Data Fig. 8 | See next page for caption.

Extended Data Fig. 8 | IKAROS protein interactome in *MLL-r* AML. a, Binary overlap percentage between all IKAROS peaks enriched 5-fold over background, genome-wide, with each of the other 3 factors, MEIS1 (at 15FE), MENIN (at 5FE) and MLL1 (at 5FE) according ChIP-seq data. **b**, IGV tracks depicting binding of IKAROS, MENIN, MLL1 and MEIS1, as determined by ChIP-seq, in the region of the TNF gene. Promoters and enhancers, predicted from the ABC tool, are indicated with genomic location indicated (Hg19). **c**, IGV tracks depicting binding of IKAROS, MENIN, MLL1 and MEIS1 at the *MYC* and *FLT3* genes as determined by ChIP-seq. Promoters and selected enhancers, predicted from the ABC tool, are indicated with genomic location indicated (Hg19). **d**, Schematic diagrams of protein domains and experimental workflow of BioID system. IKAROS, MEIS1, HOXA10 and ZNF692 proteins were tagged with the biotin ligase BirA*, the left side of the protein schematic diagram denotes N-terminal tagging and the right-side, C-terminal. MV4;11 and MOLM13 cells expressing BioID constructs, 8 total cell lines, were cultured separately. ZF = Zinc finger domain, HBD = homeobox domain, LFQ = label free quantitation, LC-MS/MS = liquid chromatography coupled tandem mass spectrometry. **e**, Western Blot analysis of the expression of BirA* and HA tagged fusion proteins in MV4;11 and MOLM13 cells, using total Histone H3 as a loading control. **f**, Venn diagram displaying the number of proteins identified in label free quantitation analysis of the MOLM13 IKAROS, MEIS1 and HOXA10 BioID LC-MS/MS data. All proteins included in Venn diagram have a > 2-fold enrichment over the ZNF692 control. **g**, List of proteins common to IKAROS, MEIS1, HOXA10 BioID identified in LFQ analysis having >2-fold enrichment over the ZNF692 control in the MV4;11 and MOLM13 cell lines.
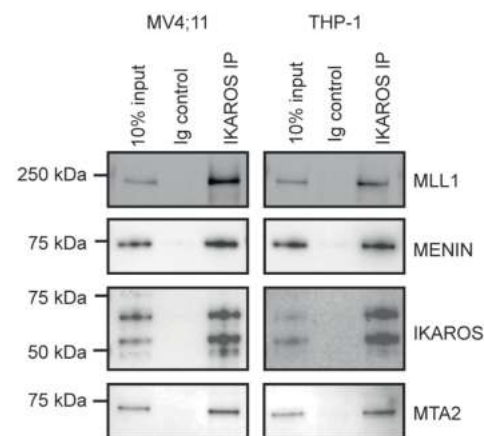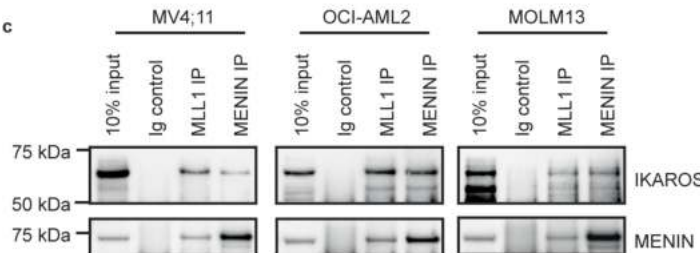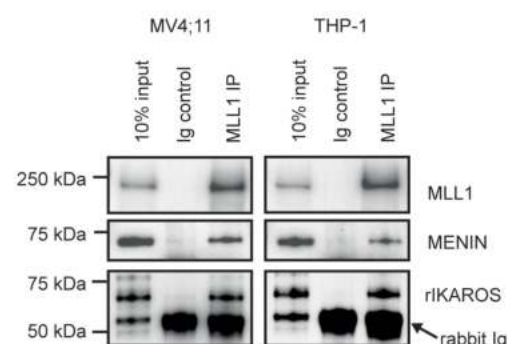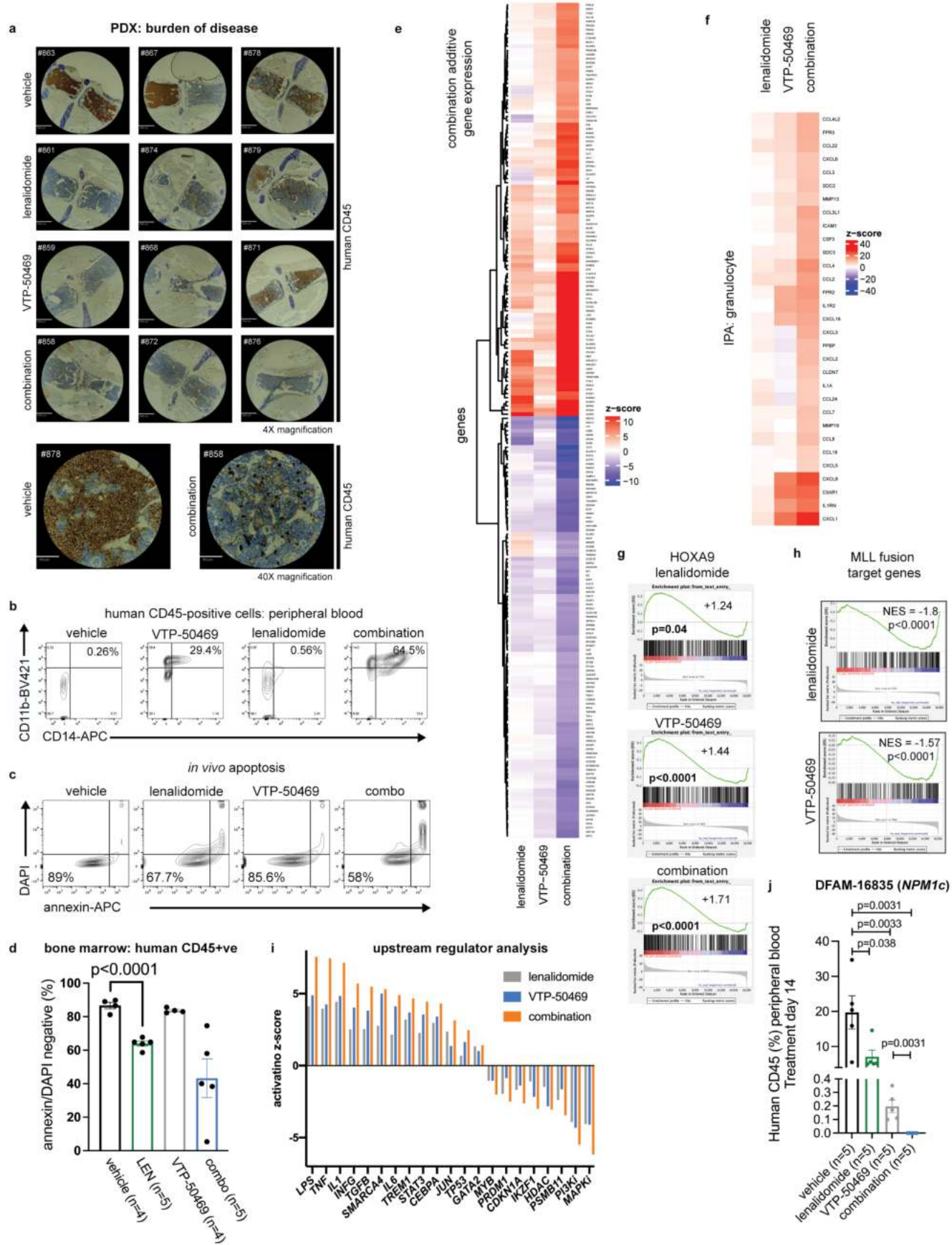
Extended Data Fig. 9 | See next page for caption.

Extended Data Fig. 9 | IKAROS and MENIN co-reside within an isolatable protein complex. a, IGV ChIP-seq tracks for IKAROS, MENIN, MEIS1 and MLL1 at selected gene TSSes. Tracks are derived from the same ChIP-seq experiments depicted in Fig. 6 and Extended Data Fig. 8. **b**, Direct protein Co-IP using IKAROS as the bait and probed for MENIN, HOXA9, MEIS1, MTA2 and IKAROS in the MV4;11, OCI-AML2 and MOLM13 cell lines using high salt nuclear extraction and detergent wash. **c**, Direct protein Co-IP using MLL1 and MENIN as the bait and probed for MENIN and IKAROS, in the MV4;11, OCI-AML2 and MOLM13 cell lines using high salt nuclear extraction and detergent wash. **d**, Direct protein Co-IP using IKAROS as the bait and probed for MENIN, MLL1, IKAROS and MTA2 in the MV4;11 and THP-1 cell lines using benzonase-treated nuclear extract and high glycerol wash. **e**, Direct protein Co-IP using MLL1 (rabbit antibody) and MENIN (rabbit antibody) as the bait and probed for MLL1, MENIN and rabbit IKAROS antibody (rIKAROS), in the MV4;11 and THP-1 cell lines using benzonase-treated nuclear extract and high glycerol wash. Rabbit immunoglobulin is seen overlying the IKAROS Western blot bands (indicated in the figure) due to the use of an anti-rabbit secondary antibody. **f**, Direct protein Co-IP using IKAROS as the bait, with and without prior VTP-50469 treatment (250 nM for 48 hr), and probed for MENIN, MTA2, and IKAROS, in the THP-1 cell line.

Extended Data Fig. 10 | See next page for caption.

Extended Data Fig. 10 | Combination therapy with VTP-50469 and LEN results in additive anti-leukemic activity *in vivo*. a, Immunohistochemistry for human CD45 antigen on bone marrow sections (sternum) on PDX/CBAM-68552 following 3 weeks treatment with vehicle, LEN 50 mg/kg daily, VTP-50469 0.1% rodent diet and the drug combination. **b**, Analysis of differentiation in circulating leukaemia cells using CD11b and CD14 expression assessed by flow cytometry in CBAM-68552 after 3 weeks drug treatment. Percentage of double-positive cells is indicated. Representative examples from individual mice are shown. **c**, Assessment of apoptosis in human CD45-positive cells from bone marrow of drug-treated mice using the CBSK-17D model following 2 weeks drug treatment. The percentage of total viable, human cells are indicated. Representative examples from individual mice are shown. **d**, Quantitation of apoptotic cells from bone marrow of mice transplanted with the CBSK-17D PDX model following 2 weeks drug treatment. Data represent mean+/−SEM with p-value by unpaired two-tail t-test. **e**, RNA-seq heatmap from PDX/CBAM-68552 following 3 weeks treatment with vehicle, LEN 50 mg/kg daily, VTP-50469 0.1% rodent diet and the drug combination. Heatmap displaying RNA-Seq DESeq2 statistical z-score for the co-regulated gene network between VTP-50469 and LEN **f**, RNA-seq heatmap displaying DESeq2 statistical z-score for genes detected in the 'granulocyte' pathway as additively deregulated using QIAGEN Ingenuity Pathway Analysis (IPA) analysis. **g**, Bar code plots using the gene set for HOXA9 regulated genes under each drug treatment from RNA-seq *in vivo* using the PDX/CBAM-68552 model. Normalized enrichment score and family-wise error rate p-value determined by the GSEA computational method. **h**, Gene set testing for reported MLL-fusion gene targets for LEN and VTP-50469. Family-wise p-value and normalized enrichment score (NES) determined by the GSEA computational method. **i**, IPA upstream regulator analysis. Graph displays selected activation z-scores for detected pathways with p-value <0.05. **j**, Measurement of peripheral blood circulating human CD45 positive cells from PDX mice transplanted with the DFAM-16835 PDX model (*NPM1c*) after two weeks of drug treatment *in vivo*. Data represent mean+/−SEM with p-value determined using unpaired, two-tail t-test.

Corresponding author(s):   Scott Armstrong

Last updated by author(s):   Mar 8, 2022

Reporting Summary

Nature Research wishes to improve the reproducibility of the work that we publish. This form provides structure for consistency and transparency in reporting. For further information on Nature Research policies, see our Editorial Policies and the Editorial Policy Checklist.

Statistics

For all statistical analyses, confirm that the following items are present in the figure legend, table legend, main text, or Methods section.

n/a	Confirmed	
☐	☒	The exact sample size (*n*) for each experimental group/condition, given as a discrete number and unit of measurement
☐	☒	A statement on whether measurements were taken from distinct samples or whether the same sample was measured repeatedly
☐	☒	The statistical test(s) used AND whether they are one- or two-sided *Only common tests should be described solely by name; describe more complex techniques in the Methods section.*
☒	☐	A description of all covariates tested
☐	☒	A description of any assumptions or corrections, such as tests of normality and adjustment for multiple comparisons
☐	☒	A full description of the statistical parameters including central tendency (e.g. means) or other basic estimates (e.g. regression coefficient) AND variation (e.g. standard deviation) or associated estimates of uncertainty (e.g. confidence intervals)
☐	☒	For null hypothesis testing, the test statistic (e.g. *F*, *t*, *r*) with confidence intervals, effect sizes, degrees of freedom and *P* value noted *Give P values as exact values whenever suitable.*
☒	☐	For Bayesian analysis, information on the choice of priors and Markov chain Monte Carlo settings
☒	☐	For hierarchical and complex designs, identification of the appropriate level for tests and full reporting of outcomes
☒	☐	Estimates of effect sizes (e.g. Cohen's *d*, Pearson's *r*), indicating how they were calculated

Our web collection on statistics for biologists contains articles on many of the points above.

Software and code

Policy information about availability of computer code

Data collection	No software was used for data collection.
Data analysis	1) bcl2fastq conversion software (v2.20.0.422; Illumina Inc.), 2) Bowtie2 (v2.3.4.3; Langmead and Salzberg, 2012), 3) STAR (v2.7.5a; Dobin et al., 2013), 4) IGVtools (2.3.75; Li et al, 2009), 5) Picard Tools (v2.9.4; Broad Institute), 6) GSEA (v3.160; Broad), 7) R Bioconductor DESeq2 package v1.24.0; Love et al., 2014), 8) CUT&RUNTools (Zhu et al., 2019), 9) MACS2 v2.1.4, 10) GNU parallel v20161222, 11) MAGeCK computational pipeline (Wang et al.; 2019), 12) Proteome Discoverer 2.2 (Thermo Fisher Scientific), 13) limma package (Ritchie et al, 2015). 14) Flowjo, Becton Dickinson (v10.6.2), 15) RStudio (v1.4.1106), 16) ComplexHeatmap (v3.14), 16) R (v3.6.0).

For manuscripts utilizing custom algorithms or software that are central to the research but not yet described in published literature, software must be made available to editors and reviewers. We strongly encourage code deposition in a community repository (e.g. GitHub). See the Nature Research guidelines for submitting code & software for further information.

Data

Policy information about availability of data

All manuscripts must include a data availability statement. This statement should provide the following information, where applicable:
- Accession codes, unique identifiers, or web links for publicly available datasets
- A list of figures that have associated raw data
- A description of any restrictions on data availability

Raw and analysed data for ChIP-seq, CUT&RUN-seq, RNA-seq, ATAC-seq and ABC model predictions have been deposited at the National Center for Biotechnology Information (NCBI) Gene Expression Omnibus (GEO) under the accession number GSE168463. Please see details for data access token below. All mass spectrometry data and search results have been deposited to the ProteomeXchange Consortium (http://proteomecentral.proteomexchange.org/cgi/GetDataset?ID=PXD007862) via the PRIDE partner repository with the data set identifiers PXD025227, PXD025228, PXD025229, PXD025230, PXD025231, PXD025232, PXD025271 and

Field-specific reporting

Please select the one below that is the best fit for your research. If you are not sure, read the appropriate sections before making your selection.

☒ Life sciences ☐ Behavioural & social sciences ☐ Ecological, evolutionary & environmental sciences

For a reference copy of the document with all sections, see nature.com/documents/nr-reporting-summary-flat.pdf

Life sciences study design

All studies must disclose on these points even when the disclosure is negative.

Sample size	For in vivo studies, mouse numbers were chosen to include at least 5 mice per treatment group. No statistical methods were used to determine sample sizes but our sample sizes are similar to those reported in previous publications.
Data exclusions	Some mice were injured during oral gavage and required euthanasia. These mice have been excluded from the analysis.
Replication	Findings underwent independent experimental validation as well as biological replication using either distinct cell line models or different patient-derived xenograft models. In vitro cell line experiments were performed at least 3 times. RNA-seq and ChIP-seq experiments were performed twice. IKZF1 CRISPR targeted MOLM13 xenograft experiment was performed once with multiple mice transplanted in each group, as indicated. PDX animal studies were performed as single cohorts of mice in 4 different patient-derived xenograft models. Replication experiments were successful.
Randomization	For in vivo studies, mice were allocated randomly to treatment groups based upon leukemia burden in the peripheral blood prior to commencing treatment. For cell line based experiments presented elsewhere in the manuscript, randomization was not required becuase the cells used represent a homogeneous population.
Blinding	No blinding was used in these studies. We did not have available resources for blinding of experiments because a small number of scientists performed the experiments.

Reporting for specific materials, systems and methods

We require information from authors about some types of materials, experimental systems and methods used in many studies. Here, indicate whether each material, system or method listed is relevant to your study. If you are not sure if a list item applies to your research, read the appropriate section before selecting a response.

Materials & experimental systems

n/a	Involved in the study
☐	☒ Antibodies
☐	☒ Eukaryotic cell lines
☒	☐ Palaeontology and archaeology
☐	☒ Animals and other organisms
☒	☐ Human research participants
☒	☐ Clinical data
☒	☐ Dual use research of concern

Methods

n/a	Involved in the study
☐	☒ ChIP-seq
☐	☒ Flow cytometry
☒	☐ MRI-based neuroimaging

Antibodies

Antibodies used	1) anti-IKAROS rabbit monoclonal antibody, Cell Signaling (Cat#14859S; D6N9Y), 2) anti-KMT2A/MLL1 rabbit antibody, Bethyl (Cat#A300-086A), 3) anti-MENIN rabbit antibody, Bethyl (Cat#A300-105A), 4) anti-MEIS1 rabbit antibody, Abcam (ChIP-grade, Cat#ab19867), 5) Mouse isotype IgG control (Cell Signaling (Cat#5415)), 6) anti-cMYC antibody (Abcam Cat#ab32072), 7) anti-Histone H3 antibody (Abcam Cat#ab1791), 8) anti-GAPDH, mouse monoclonal antibody (Cell Signaling Cat#97166S), 9) anti-beta-ACTIN rabbit monclonal HRP-conjugate (Cell Signaling Cat#12620S), 10) anti-CTCF (XP) R (Cell Signaling Cat#3418S/D31H2), 11) anti-IKAROS mouse monoclonal antibody (Invitrogen Cat#MA5-28613), 12) anti-human CD45, PE-conjugated (BioLegend Cat#304058), 13) anti-human CD11b, BV421-conjugated (BioLegend Cat#301324), 14) anti-human CD14, APC-conjugated (BioLegend Cat#367118), 15) rabbit isotype IgG control (Bethyl Cat#P120-201), 15) anti-MTA2/PID rabbit polyclonal (Abcam Cat#ab8106), 16) anti-HOXA9 rabbit antibody (Abcam Cat#ab140631), 17) anti-LAMINB1 (Abcam Cat#ab16048), 18) anti-Histone H3K27-acetyl (Diagenode Cat#C15410196), 19) anti-Casein Kinase 1-alpha (Abcam Cat#ab108296), 20) anti-MCL1 antibody (Cell Signaling Cat#94296S), 21) anti-BCL2 (Cell Signaling Cat#15071), 21) anti-BCL-XL (Cell Signaling Cat#2764S), 22) anti-human CD135 (FLT3/Flk-2) antibody, PE-

	conjugated (BioLegend Cat#313306/BV10A4H2) 23) anti-rabbit IgG, HRP-linked Antibody (Cell Signaling Cat#7074). Dilutions for each antibody are detailed in the Methods section.
Validation	We validated antibody specificity for the anti-IKAROS rabbit monoclonal antibody (Cell Signaling Cat#14859S) and the anti-MTA2/PID rabbit polyclonal antibody (Abcam Cat#ab8106) by CRISPR-CAS9 knockout; that is, genetic deletion of each gene resulted in loss of the target protein detection by Western blot.

Cell Signaling provides a generic "Antibody Performance Guarantee" to ensure product performance; Cell Signaling states that it validates all antibodies, in-house, in multiple research applications.

Bethyl antibodies are stated to undergo "strict validation testing" with details available online (https://www.fortislife.com/antibody-validation).

Abcam antibodies are also stated to undergo strict validation with details provided online (https://www.abcam.com/primary-antibodies/how-we-validate-our-antibodies).

Biolegend performs specificity testing of all antibodies in 1-3 target cell types with either single- or multi-color analysis (including positive and negative cell types). Once specificity is confirmed, each new lot must perform with similar intensity to the in-date reference lot. Brightness (MFI) is evaluated from both positive and negative populations. Each lot product is validated by QC testing with a series of titration dilutions.

For all applications and antibodies used in our study, the antibody was verified by the manufacturer to react specifically with the target protein of interest and was procedurally validated for the relevant application. For ChIP-seq experiments, we used ChIP-seq grade antibody. It was beyond the scope of our available resources to independently validate these antibodies beyond the information that is provided by the manufacturer. |

Eukaryotic cell lines

Policy information about cell lines

Cell line source(s)	Cell lines were acquired from American Type Culture Collection (ATCC) or the Deutsche Sammlung von Mikroorganismen und Zellkulturen (DSMZ), as indicated: HEK293T cells (ATCC #CRL-3216), MOLM13 (DSMZ Cat#ACC554), MV4;11 (ATCC Cat#CRL-9591), OCI-AML2 (DSMZ Cat#ACC-99), THP-1 (ATCC Cat#TIB-202), OCI-AML3 (DSMZ Cat#ACC-582), U937 (ATCC Cat#CRL-1593.2), and HL60 (ATCC Cat#CCL-240). The IMSM2 cell line (NPM1c) was a kind gift from Dr. Daniel Tenen, Harvard Medical School,and originally sourced and described by Chi et al (Leukemia Research, V34, issue 2, pp261-262, 2010) and HEK293T cells (ATCC #CRL-3216).
Authentication	Identification of all cell lines was independently confirmed by cytogenetics profiling.
Mycoplasma contamination	Routine mycoplasma testing was negative.
Commonly misidentified lines (See ICLAC register)	No commonly misidentified cell lines were used in this study.

Animals and other organisms

Policy information about studies involving animals; ARRIVE guidelines recommended for reporting animal research

Laboratory animals	NOG-F mice (NOD.Cg-Prkdcscid Il2rgtm1Sug/JicTac) (Taconic BioSciences, USA). All transplanted mice were female, aged between 8-10 weeks on delivery to the facility, and injected 1-2 weeks thereafter. Laboratory mice are housed in solid-bottom, polysulfone 75 sq. in. microisolator cages. The cages are used in conjunction with the Optimice® rack systems with integrated automatic watering. Temperature and humidity in the rodent facilities are controlled at 72 +/- 2°F and a target range of 35-55% relative humidity. A standard photoperiod of 12 hours light/12 hours dark is controlled by an automated system.
Wild animals	No wild animals were used in the study.
Field-collected samples	No field-collected samples were used in the study.
Ethics oversight	All animal experiments were performed with the approval of Dana-Farber Cancer Institute's Institutional Animal Care and Use Committee (IACUC).

Note that full information on the approval of the study protocol must also be provided in the manuscript.

ChIP-seq

Data deposition

☒ Confirm that both raw and final processed data have been deposited in a public database such as GEO.

☒ Confirm that you have deposited or provided access to graph files (e.g. BED files) for the called peaks.

| Data access links
May remain private before publication. | To review GEO accession GSE168463:
Go to https://secure-web.cisco.com/1b6PdCb2qUPUvUjBiiFgyjFbB0onmPWy8Yu5NvxR2qOIL8JGmOAh5FGFoQ1hAkcrcLBjfSgVdsSXk1mbnKBRR- |

djXbgDtQQM_Bz6VH774Skro1IGY6YD6VzyMwsNCREeafXvh2wx5Aoy63GXKWQI2HAkiGn7scgNuXiUFFweq_YYd6t3C0p-N1_ADR88EhVfrHeIMXswCj-UKxbhV4SQ3FM4irXdKXLnhzO1rfJCJygTyiIJQdcuWmOv9d-I1CVt33G54TlvmI41z6ExFtUJXkg/https%3A%2F%2Fwww.ncbi.nlm.nih.gov%2Fgeo%2Fquery%2Facc.cgi%3Facc%3DGSE168463

Files in database submission	GSM5140845, GSM5140846, GSM5140847, GSM5140848, GSM5140849, GSM5140850, GSM5140851, GSM5140852, GSM5140853, GSM5140854, GSM5140855, GSM5140856, GSM5140857, GSM5140858, GSM5140859, GSM5140860, GSM5140861, GSM5140862, GSM5140863, GSM5140864, GSM5140865, GSM5140866, GSM5140867, GSM5140868
Genome browser session (e.g. UCSC)	Fully analyzed datasets for ChIPseq data have been deposited as TDF files in GEO under the above accession numbers. The TDF files can be visualized in the Integrated Genomics Viewer (IGV) (Broad Institute).

Methodology

Replicates	Chip-Seq experiments were performed as two completely independent experiments for each factor: IKAROS/IKZF1, MEIS1, MLL1, and MENIN.
Sequencing depth	All experiments measured 37mer paired-end reads. Two independent experiments for each cell line and transcription factor were performed and then combined into a single analysis. Total, combined read counts for each experiment are as follows with total reads and uniquely mapped reads indicated, respectively: MOLM13 IKZF1/IKAROS: 74387056 and 61880286, MOLM13 input: 188,881,670 and 169,466708, MOLM13 MEIS1: 115766646 and 107145186, MOLM13 MENIN: 60226646 and 51771260, MOLM13 MLL1: 94302938 and 78874532, MV411 IKZF1: 59288840 and 49928702, MV411 input: 143741076 and 128887078, MV411 MEIS1: 102687700 and 92738226, MV411 MENIN: 64865086 and 56881566, MV411 MLL1 85115432 and 70585364.
Antibodies	1) anti-IKAROS rabbit monoclonal antibody, Cell Signaling (Cat#14859S; D6N9Y), 2) anti-KMT2A/MLL1 rabbit antibody, Bethyl (Cat#A300-086A), 3) anti-MENIN rabbit antibody, Cell Signaling (Cat#A300-105A), and 4) anti-MEIS1 rabbit antibody, Abcam (ChIP-grade, Cat#ab19867)
Peak calling parameters	Read mapping and peak calling was performed using STAR (v2.7.5a) and MACS2 (v2.1.4), respectively. All peak calling was determined to a paired input control sample with FDR set to 1% and peak calling at 5-fold enrichment (IKAROS, MLL1, MENIN) or 15-fold enrichment (MEIS1) over background. A representative command line is shown below: MOLM13_ChIP_IKZF1: -t MOLM13_ChIP_IKZF1_steadystate_REP1_200713-200818_hg19_sorted_readgps_rmdup.bam -c MOLM13_ChIP_input_200717-200818_hg19_sorted_readgps_rmdup.bam -n MOLM13_ChIP_IKZF1 -g hs -f BAMPE -q 0.01 --slocal 1500 --outdir Parameters defined as follows: -t: the BAM file to call peaks on -c: the matched input control BAM file for the current sample -n: specific name prefix for the output files for the current sample -g: genome/species for current analysis ("hs" for all samples) -F: paired-end indicator ("BAMPE" for all samples) -q: qValue (minimum FDR) cutoff ("0.01" for all samples) -slocal: "small local region" parameter ("1500" for all samples) --outdir: output dir for results --tmpdir: temporary dir for intermediate files; same for all samples
Data quality	All peak calling was determined to a paired input control sample with FDR set to 1% and peak calling at 5-fold enrichment (IKAROS, MLL1, MENIN) or 15-fold enrichment (MEIS1) over background.
Software	1) bcl2fastq conversion software (v2.20.0.422; Illumina Inc.), 2) STAR (v2.7.5a; Dobin et al., 2013), 3) IGVtools (2.3.75; Li et al, 2009), 4) Picard Tools (v2.9.4; Broad Institute), 5) MACS2 v2.1.4

Flow Cytometry

Plots

Confirm that:

☒ The axis labels state the marker and fluorochrome used (e.g. CD4-FITC).

☒ The axis scales are clearly visible. Include numbers along axes only for bottom left plot of group (a 'group' is an analysis of identical markers).

☒ All plots are contour plots with outliers or pseudocolor plots.

☒ A numerical value for number of cells or percentage (with statistics) is provided.

Methodology

Sample preparation	1) For cell counting during cell line-based experiments, viable cell counts were measured using a BD Bioscience LSRFortessa Cell Analyser on indicated time points, with DAPI used as viability stain, by counting the total number of viable cells within a predetermined sample volume analysed. 2) For flow cytometry-based apoptosis assays, cell viability and surface annexin V was measured using the Annexin V Apoptosis Detection Kit (eBioScience Cat#88-8007074) according to the manufacturer's instructions. 3) For cell cycle analysis, cells were collected after indicated drug treatments, washed in PBS and fixed using the Cytofix/Cytoperm kit (BD Bioscience Cat#554714) prior to DAPI staining and direct analysis by flow cytometry. 4) For assessment of differentiation, after indicated drug treatment or CRISPR/Cas9 modification, cells were washed in PBS and

then stained with BV421-conjugated anti-CD11b (BioLegend Cat#301324) and APC-conjugated anti-CD14 (BioLegend Cat#367118) for 30-60min followed by a minimum of three washes in PBS with 1% FBS. Samples were then analysed on an LSR Fortessa flow cytometer (Becton Dickinson). 5) Blood samples were processed with red cell lysis using Pharm Lyse (BD Cat#555899) prior to staining with phycoerythrin (PE)-conjugated anti-human CD45 antibody (BioLegend), BV421-conjugated anti-CD11b (Biolegend) and APC-conjugated anti-CD14 (BioLegend), as indicated. Samples were then analysed on an LSR Fortessa flow cytometer (Becton Dickinson).

Instrument   LSR Fortessa (Becton Dickinson)

Software   FlowJo v10.6.2 (Becton Dickinson)

Cell population abundance   Minimum 10,000 events collected for analysis.

Gating strategy   For analysis of in vivo experiments, mononuclear cells were first distinguished using a standard FSC/SSC gating strategy. Human cells were then distinguished from mouse cells by staining with human-specific anti-CD45 PE-conjugated antibody. Cells were gated on human CD45-positive cells only and then evaluated for staining of anti-CD11b BV421-conjugated antibody and anti-CD14 APC-conjugated antibody.

☒ Tick this box to confirm that a figure exemplifying the gating strategy is provided in the Supplementary Information.